Lipid and protein interactions at air-water interface: correlating structural organization with rheological properties

By

Saba Ghazvini

Submitted to the graduate degree program in Bioengineering and the Graduate Faculty of the University of Kansas in partial fulfillment of the requirements for the degree of Doctor of Philosophy.

_____

Chairperson: Professor Prajnaparamita Dhar

_____

Professor David B. Volkin

_____

Professor Stevin H. Gehrke

_____

Professor Cory J. Berkland

_____

Professor Kevin C. Leonard

Date Defended: June 26, 2017

The Dissertation Committee for Saba Ghazvini certifies that this is the approved version of the following dissertation:

Lipid and protein interactions at air-water interface: correlating structural organization with rheological properties

_____

Chairperson: Professor Prajnaparamita Dhar

Date approved: June 26, 2017

Abstract

Biological compounds such as lipids and proteins are building blocks of all living species and therefore, understanding how interactions between these molecules contribute to proper biological functioning is of great importance. Among the various perspectives of understanding lipid and protein interactions, this thesis is focused on the interaction of these molecules at the air-water interface. Lipid and proteins at the liquid interfaces are both abundant and influential. A few of the biological and physiologically relevant interfaces include cell membrane, tear film, and lung surfactant. While biological interactions of lipids and proteins regulate cell process, enable the lung function and keep us alive, some of these interactions could also be unfavorable in industrial applications. For example, interaction of proteins at the interfaces has been a source of concern in pharmaceutical industry due to the protein aggregation and particle formation initiated or increased in presence of the interfaces. This thesis has been focused in both biologically and industrially relevant studies of lipids and proteins at the air-water interface to learn how to better measure and predict these interactions. An active microrheology, imaging techniques, and surface energy measurements have been used to visualize and characterize the chemical-mechanical behavior of the lipids and proteins at the interface. The results showed interesting points on the influence of lipid chemistry, including headgroup charge, size, and saturation of the tail, on its interfacial rheological properties. The effect of subphase properties such as pH had a great influence on lipid packing. Additionally the interaction of lipids at the interfaces is greatly influenced by presence of even small ratios of protein or nanoparticles; the lipid-protein mixtures were significantly more viscose than lipid mixtures. Moreover our studies using a model IgG1 mAb had shown the role of air-water interface and its renewal due to mechanical stress on protein particle formation. The interfacial properties of the protein films were influenced greatly by the liquid buffer properties such as pH. Future studies on correlating the chemical-mechanical properties of lipids and proteins and their macroscale behavior at interface could shed light on important physiologically and industrially relevant questions.

Dedicated to:

Maman, Baba, Sahar, Saman, Dayi Mansour, and Mamanjoon Tabrizi

Acknowledgment

I would first like to express my sincere appreciation to my advisor, Professor Prajnaparamita Dhar. I am very grateful for having had the opportunity to work with such an enthusiastic scientist as her enthusiasm and passion to her work is contagious. I am thankful for all the mentorship and many long days she spend training, teaching, and discussing science with us at school. It definitely takes a lot of effort to transform students with a BS degree to independent scientists who are able to discover and build. I am very appreciative for her guidance, direction, patience, and support through these years.

I am very thankful to be mentored and advised by such a great committee: Professor Stevin Gehrke, Professor Cory Berkland, Professor Kevin Leonard, and Professor David Volkin. Beside my adviser, I have been a teaching assistant of Professors Gehrke and Berkland during my studies at KU that not only gave me an opportunity to observe and learn their teaching style, but gave me a chance to explore my passion for teaching and mentoring. I am also thankful to both of them for giving me an opportunity to collaborate with their groups. I am very thankful to Professor Leonard for his support and knowledge, especially what he thought us in his classes and the great influence of that in my research.

My special thanks to Professor David Volkin for all I have learned from his interesting classes, and working with him and his student Dr Cavan Kalonia. As Professor Volkin says, to be a professional independent scientist we need to learn how to collaborate and communicate, and I could not have asked for a better experience. Our collaboration would have not been possible without the support and help of Dr Cavan Kalonia and all of Volkin group that I am truly grateful for.

I am very thankful for many other great mentors and advisers at KU, especially Professor András Czirók at Anatomy and Cell Biology department of KU, his team, and Dr Zsuzsa Ákos for giving me an opportunity to collaborate with them. I am very thankful for the mentorship, guidance,

Table of Contents

Chapter 1: Introduction

1.1. Background

Interfaces are everywhere, from every cell membrane in your body to the emulsions making your salad dressing. The boundary of two immiscible phases creates an interface also referred to as interphase [1]. The interface is the finite layer between two phases at which the chemical and physical properties change from one phase to next phase. Since there are three types of bulk phases, a variety of interfaces exist. This work is focused on the interfaces that involve liquids. Liquid interfaces play a great role in the creation of foams, emulsions, colloids, soaps [1, 2]. The science and technology in the creation and modification of emulsions and foams are heavily used in food, paint, cosmetic, and pharmaceutical industries[1]. Due to the industrial importance of foams, emulsions, and colloids, liquid interfaces have been studied and characterized for the past couple decades [1, 3, 4]. The classical characterization of interfaces was mostly focused on pure compounds. Surface energy was commonly measured in terms of surface tension or surface pressure. At air-liquid and solid-liquid interfaces it was measured using Wilhelmy plate (figure 1), capillary rise, and contact angle. However, many of the liquid interfaces are complex interfaces where either the bulk phases are not pure compounds or material that exist in one of the two phases would concentrate or adsorb to the interface.

Biological interfaces are among these complex interfaces, mostly liquid-liquid, and has been the sole focus of this thesis. The plasma membrane of a cell creates a liquid-liquid interface, where it separates two aqueous phases and controls the transport and therefore the properties of the intracellular matrix [5]. The cells are similar to the emulsions in that the membrane is the boundary that separates the two liquid phases. Another crucial liquid-liquid membrane is found where the blood capillaries meet the organ tissue where the mass transport between blood and the

tissue occurs [5]. In addition to liquid-liquid interfaces, air-liquid interfaces exist in the body at the outer surface of our eyes and inner lining of the lungs, where a liquid is in contact with air.

1.2. Lung surfactant at the air-water interface

Lung surfactant (LS) is referred to the lipid-protein mixture that exists at the air-liquid interface of the lungs. The lipids and proteins of the LS are secreted by alveoli cells in healthy lungs [6, 7]. Lipids are biological surfactants, holding both hydrophilic and hydrophobic moieties (figure 2), and therefore the lipids find it energetically favorable to adsorb to the air-water interface (figure 3). The phospholipids of lung surfactant are responsible for reducing the surface tension of the lung, which reduces the energy required to compress-expand the alveoli sacks. A unique feature of natural lung surfactant is the reversible collapse of the film after compression and re-adsorption of the surfactants [8]. The film also spreads very quickly during the expansion of the lung[9]. While the saturated lipid reduces the surface tension to almost zero, unsaturated lipids facilitate the re-adsorption of the lipids to the interface during the expansion [10-12]. Studies have shown that proteins also facilitate both the re-adsorption of the lipids and the reversibility of the collapsed film [10-13]. There are still many unanswered questions regarding the interactions between lipids and proteins and role of chemical moieties in creating an active, long-lasting lung surfactant.

Understanding the basic science behind lung surfactant function, was investigated to understand the link between lung-related diseases and lung surfactant. Unfortunately, acute lung injury (ALI) and acute respiratory distress syndrome (ARDS) could affect patients of all ages from infants to adults[7]. The consequence of lung diseases and injuries, could be impaired breathing or in many severe cases it could cause death [7]. ARDS and ALI are coupled with deficiency or dysfunctionality of lung surfactant[7, 14]. One percent of all the new born babies suffer from

deficient lung surfactant since the lungs of premature babies are not developed yet to produce adequate natural lung surfactant [14]. To address lack of natural lung surfactant, replacement lung surfactant, also referred to as exogenous lung surfactant, has been made. The commercial exogenous LS were beneficial in clinical use especially for premature infants [7].

Exogenous lung surfactant compositions vary significantly based on the source, the procedure, and the solvents [7, 9, 15]. The most successful exogenous LS to treat ARDS in premature infants have the most similar composition to natural LS, since all the natural component of LS play a significant role in the overall dynamic function[7]. While the presence of protein in success of *in vivo* models has been detected, biophysical research explored the mechanism of contribution of proteins *in vitro*. Imaging coupled with surface pressure isotherms suggested that the LS film folds at the end of compression, pushing parts of the folded layers into the liquid sub-phase, but un-folds to the air-liquid interface during the expansion by re-adsorption of the folded part to the air-liquid interface[8, 9, 13]. The proteins and lipids of LS are typically extracted from intact animal lungs [7]. Unfortunately using an animal source for the proteins can cause impurities in the mixture and inflammation issues in the patient [7]. Additionally, this type of extraction of lipids and proteins increases the cost of the final product [7]. The most desirable way of avoiding the cost and toxicity probabilities of using animal lung surfactant, is to synthesize the phospholipids and proteins instead. In theory, the synthetic lipids and proteins should ultimately guarantee similar clinical activity to the natural lung surfactant. However, since the function of lung surfactant is a very complicated chemical-mechanical behavior, producing synthetic LS with similar clinical activity is challenging in practice.

Treating dysfunctional LS has been more challenging compared to treating lack of lung surfactant. One of the issues that appears in injured lungs are the presence of plasma lipids or blood

proteins in surface of Lungs which interfere with the natural surfactant film [7, 15]. The inflammation by bacteria or viruses could degrade the surfactants and proteins, inhibiting the presence of natural composition of LS . Additionally, type II cells, the stem cells of epithelium, could be damaged in lung injuries that affects the synthesis, secretion, and recycling of natural LS [7, 15]. The replacement LS has not been successful in targeting inflammatory lung injury since a combined-modality therapy is required to treat ARDS [7, 15]. To design a replacement that has combined-modality therapy, the interfacial science behind the surface activity of combination of different LS related components should be studied.

One of the less studied aspects in lung surfactant composition is the influence of each component in overall interfacial fluidity of the film to improve both fast spreading and reversible folding of the film. Two major features of natural lung surfactant, fast spreading and reversible compression-expansion, could be characterized based on the mechanical properties of the film [16, 17]. More specifically, the viscoelastic properties of the film could describe the fluidity and the elasticity of the LS in its natural function. During the compression, the available surface area decreases and, the surfactant packing changes from a two-dimensional liquid-expanded phase, to liquid-condensed phase and ultimately a solid phase [17-21]. The change in packing which occurs during the transition from liquid-expanded to solid 2D is drastic and dependent on the chemical features of natural LS [16, 17, 22]. The presence of protein and the combination of unsaturated-saturated lipids accommodate the viscoelastic properties but there are not enough studies to quantify the viscoelasticity of the mixture. To learn more about the viscoelastic properties of LS and the role of each component in the overall behavior of the LS, rheometry should be used at the air-liquid interface.

The rheology of LS could explain the nature of its intermolecular interactions and therefore, a motivation to study the viscoelasticity of this lipid-protein film. As the attractive interaction between the components (surfactants, proteins, or particles) of the film increases, more energy is required to overcome these interactions for the fluid to flow. The dissipation energy is measured in terms of surface viscosity. If the nature of the interactions are more irreversible that would enable the film to store the applied energy and therefor the film might have elastic properties as well as viscous properties. Surfactant layers, such as lipids, mostly possess viscous properties [16, 17, 22]. However, by addition of particles or proteins to the surfactant mixtures the type of interaction could change [22]. Complexity of a lipid-protein rheological behavior is equivalent to a surfactant-protein or surfactant-particle system that have applications in industrial manufacturing [1]. In the emulsion and foam design, soluble or non-soluble surfactants in combination with nanoparticles are used. The viscoelastic properties of the mixed layer of particle and surfactant varies based on the hydrophobicity of the particle and the interactions of it with the interface [1].

1.3.   Interfacial rheology

Due to the interest in exploring the films and interfacial properties, interfacial rheological instruments have been designed. A majority of interfacial rheometrical instruments are inspired by the bulk rheometry and modified to specifically measure the viscosity and elasticity of the interface [3, 4]. Among these interfacial rheometrical instruments both dilatational and shear rheology have been used [3, 4, 23]. In both cases the response of the fluid to an applied stress is measured at the interface. the common theories to calculate viscous and elastic components are the Kelvin-Voigt and the Maxwell model based on the assumption of additive stress (parallel dashpot and spring) or additive strain (dashpot and spring in series) [3, 4, 23]. In applying a shear stress, the surface area remains constant while a probe shears the sample and changes the shape. On the other hand in

applying the dilatational stress, the shape remains constant while the surface area is forced to change. Both shear and dilatational rheology could be categorized in different types; the instrumentation and the sensitivity of these rheometers varies.

One of the common methods of applying the dilatational rheology to a film at air-water interface is change of surface area using a Langmuir trough while recording surface pressure (surface tension). The viscoelastic modulus ($\tilde{E}(t) = -\left(\frac{\partial \Pi}{\frac{\partial A}{A}}\right)_T$) could be obtained based on change of surface pressure versus area [1, 3, 4]. For insoluble monolayers at equilibrium the viscoelastic modulus equals the compressibility modulus [1]. In conditions further away from equilibrium the response of the film to change of surface area is non-linear. The solution to the non-linear response of films is more complicate to analyze since the numerical solutions do not provide accurate answers to complicated theoretical equations based on the irreversible thermodynamics [4]. Additionally, using the Langmuir trough, stress-relaxation and creep experiments could also be studied by applying sudden perturbation or compression after reaching equilibrium [1, 24]. Furthermore, several different dilatational rheometrical instruments have been used to explore complex fluid-fluid interfaces including pendant drop, bubble tensiometer, and capillary wave techniques.

Shear rheology studies the response of the fluid to a shear stress applied by a solid probe. While shear rheometry has been used for decades to measure the viscoelastic properties of the bulk, measuring the rheological properties of a film at an interface is very challenging. The main challenge in surface rheometry, is decoupling the interfacial properties from the bulk properties as introduced by Lord Rayleigh[5, 25, 27, 28]. To decouple the interface from the bulk, a ratio has been defined by Boussinesq as interfacial stresses to bulk stresses ($B_0 = \frac{\eta_S}{\eta L}$) . The surface

viscosity is presented by η_s while η presents the subphase (or bulk) viscosity, and L is the ratio of the wetted surface area to perimeter of the rheometer probe. This dimensionless number includes the effect of the size of the rheometrical probe (L). Therefore, to increase the sensitivity, either the specific geometrical length of the probe should be reduced or the perimeter to surface area ratio should be increased [25, 28]. The bigger the B_0 number, the more sensitive the measurements are. The common commercially available techniques are bi-cone surface rheometer, double-wall ring rheometer, the channel viscometer [3, 4, 25, 28]. The sensitivity of these instruments varies form 10^{-3}-10^{-6} Ns/m depending on the geometry of the probes.

One of the most successful surface rheometers, the interfacial stress rheometer (ISR), is designed by Fuller group at Stanford University[25] (figure 4). ISR consist of a magnetic needle at the air-water interface of a channel. By applying a magnetic field, the needle oscillates on its axial direction. Based on the geometry of the needle, the magnitude of the applied force, and the needle oscillation amplitude surface viscosity, storage modulus, and loss modulus could be calculated. Since the size of the needle is on the scale of millimeters, it allows measurement of surface viscosity down to 10^{-6} Ns/m [25]. This rheometer is also called a needle rheometer and has been used to explore several types of lipid-protein interactions mostly focusing on tear film lipids. The macrorheology techniques including ISR has been successful in measuring the viscoelastic properties of lipid-protein films that contain significant viscoelasticity, however, a higher sensitivity is needed to capture the interfacial properties of less viscous layers including phospholipid monolayers.

With the development of fabrication techniques and nanotechnology, micron and submicron sized probes have been designed and used to increase the sensitivity of the measurement 2-3 orders of magnitudes higher than commercially available instruments [3, 4, 23, 27-29]. Since

these smaller size probes provide a possibility of measuring the viscoelastic properties in micron scale of material, the instruments are called microrheology. For each geometry the impact of the bulk and interfacial stresses are carefully analyzed and separated. The microrheology therefore is more appealing to explore the phospholipid interfaces, since the sensitivity is more appealing [28]. It is important to note that the micrometer sized probes are used in both active and passive rheometry to explore biological interfaces [4, 23]. In active rheometry the probe is forced to move and the deformation of surrounding environment in response to the applied force, is measured. On the other hand, in passive rheometry the probe is not forced to move, rather passively moved by Brownian motion of the molecules[1]. The viscosity is then measured based on the displacement of the probe and using Einstein equation[4, 23]. Passive rheometry with small probes promises a high sensitivity of measurements. However, especially in presence of proteins that increase the elasticity of the film, the passive rheometry could be less accurate compared to active rheometry to measure the viscoelasticity of the film, since the probes only sense a limited local microenvironment [3, 4, 23]. To improve this limitation two-point microrheology has been used which records the correlated thermal motion of two particles to take into account a larger local range [3, 4, 23].

One of the successful active microrheometry instruments, used by Zasadzinski and Squires groups is a disk-shape magnet that rotates in presence of a magnetic field to align in the magnetic direction [26] (figure 4). The reorientation of the disk-shape probe, also referred to as micro-button, shears the microenvironment. The micro-button has been used to characterize lipids present in lung surfactant [16, 22, 26, 30]. The disk has a 100 µm diameter and 1 µm thickness that allows for surface viscosity measurement as low as 10^{-7} Ns/m could be measured [22]. Zasadzinski and Squires groups have coupled the fluorescence imaging with rheometrical studies to visualize the

effect of the probe on the deformation of the lipid monolayer at the air-water interface [26]. They have applied different surface pressures (surface tension) that correspond to change of surface area during the compression-expansion of the lung, and have studied the rheological properties of a saturated phospholipid monolayer[22, 26, 30]. Furthermore, they have studied the effect of additional components, such as palmitic acid and cholesterol, on lipid monolayer fluidity. While, in the liquid-condensed phase of phospholipid monolayer, a high viscosity and even elasticity has been detected, there is a lot less information available on the liquid-expanded phase. It is expected that in the absence of crystalline order in LE phase, the monolayer should have lower viscosity and the sensitivity of micro-button was not sufficient to detect any changes in that region. Additionally, more complex films with different combinations of saturated and unsaturated lipid and protein compositions have not been explored.

Dhar and Fischer groups have designed and used an even more sensitive active microrheology instrument using nanorods that are 300nm in diameter and 3-50 µm in length [31-34]. The nanorods similar to the disk-shape probe reorient toward the applied magnetic field and the viscoelastic properties of the film could be calculated based on the geometry of the rod and rate of the reorientation [31, 32, 34]. The smaller size of nanorods allows for measuring the surface viscosity down to 10^{-9} Ns/m [31, 32, 34]. This instrumentation have been used to measure the viscoelastic properties of different type of bulk and films including surfactant-particle mixture and protein films [31, 32, 34]. The success of the previous studies led us to use this technique to explore the biological films in more details.

The majority of the studied lipids are present in lung surfactant; however, they are also main components of cell membrane. The relation between their nanoscale chemical features to microscale packing and fluidity could be used to understand fundamentals of membrane fluidity.

Membrane fluidity could be a key element in drug delivery science. Furthermore the lipid-protein interactions mimicking cell membrane could shed light on discovering more about diseases such as Alzheimer's that are involved with complex cell membrane disruption.

Furthermore, the existence of biological interfaces extends beyond the physiological examples, to the biotechnological applications of large molecules. Interfaces including solid-liquid and air-liquid are factors effecting protein aggregation in pharmaceuticals. For example, monoclonal antibodies (mAb), designed as therapeutic treatments encounter several interfaces during manufacturing and consumption [35-38]. There is a significant concern that these unavoidable interfaces can induce unwanted protein aggregation, since protein particles in biological drugs can lead to loss of functionality of the protein drug or result in undesirable immune response. Due to challenges of isolating the interface from the bulk, there are lots of questions on the unfolding/aggregation pathways triggered by the interfaces. To minimize the exposure of proteins to the air-liquid interface, surfactants are commonly used in industry [39, 40]. With smaller size and amphiphilic properties, surfactant adsorb faster than proteins to the interfaces and protect the proteins from interfaces. Because of the industrial impact of the protein-protein interactions at interfaces, studying these interactions have captured a lot of attention. The basic biophysical science that explores Langmuir surfactant monolayers and surfactant-protein films could be used to study these protein films even further.

1.4. Thesis overview

The long-term goal of this project is to increase our fundamental understanding of lipid/protein interactions at interfaces with applications in biology and biotechnology. The mechanical properties at the interface are linked to the structure-function relationship of the lipid protein but

are not a well explored characteristic at the interface. By developing and using a unique active microrheology set-up which is three orders of magnitude more sensitive than commercial rheometers, surface viscosity and elasticity of these monolayers can be accurately measured for the first time. Furthermore, measurement of the interfacial energy in terms of surface tension could add to our understanding of the type and strength of interactions at interface. To investigate interfacial properties which are modulated by the biochemical composition, the following studies are completed:

In chapter 2, an active interfacial microrheology setup coupled with imaging and surface tension measurements was built to characterize the interfacial properties of phospholipid monolayers. The nanorods as rheometrical probes have been used to measure surface viscosity by applying magnetic field. The unique feature of this set-up is that the coils are imbedded in the Langmuir trough, therefore while by moving the barriers of trough the surface pressure of the layer could be controlled, the rheological properties could be measured. This set-up also enables simultaneous fluorescence and visible imaging of lipids and nanorods. As a first step, the fluidity of two saturated phospholipid monolayers has been characterized; which share the same (PE) head group but differ in their hydrocarbon chain length. These lipids are great candidates to study rheological properties as their molecular packing at the air-water interface is very well established by X-ray diffraction and other high resolution techniques. The result suggests that changes in surface viscosity were related to changes in alkyl chain length and modulated by packing density, which leads to differences in phases and phase transition. Therefore for the first time, phase transitions of phospholipid monolayers have been detected by surface viscosity measurements.

In chapter 3, the interfacial rheological properties of unsaturated phospholipid monolayers were characterized. Unsaturated phospholipids contribute greatly to the overall desired fluidity of

natural lung surfactant by virtue of their unique packing properties at the air-water interface. Regardless of head group moiety, unsaturated phospholipids exist in liquid expanded order and therefore possess a high fluidity, however the fluidity of these monolayers have not been quantified before. Since one of the goals of this research is to ultimately evaluate the mechanical properties of replacement lung surfactant, unsaturated phospholipids should be characterized individually as one of the main components. Furthermore, since unsaturated lipids are exposed to changes of bulk charge (pH and presence of ions) in biological relevant situations, this study also explored the potential change in packing density of unsaturated lipids by change of pH. Following chapter 2, the effect of head group moiety on surface viscosity of four types of the most abundant unsaturated phospholipids present at cell membranes have been studied. The surface viscosity measurements at pH 4.4 compared to pH 7.4 showed how the charge and size of head group could potentially influence the packing density of these molecules at the air-water interface. Additionally, the topographical imaging of lipid monolayers by atomic force microscopy (AFM) confirmed the increased presence of non-homogeneous features at lower pH that possibly contribute to the overall surface viscosity.

In chapter 4, the interfacial properties of phospholipid-protein mixtures, mimicking lung surfactant were characterized. The effect of saturation/unsaturation of lipid tails, size/charge of phospholipid head group and presence of protein on overall mechanical properties of monolayer has been evaluated. While the addition of unsaturated lipids decreases the overall viscosity of the lipid-protein mixture, the charge of the headgroup moiety of unsaturated lipids greatly influenced the extent of reduction of the surface viscosity. This furthermore emphasizes on the importance of the presence of both zwitterionic and anionic unsaturated lipids to modulate the interfacial rheological properties.

In chapter 5, interfacial properties of a model IgG1 monoclonal antibody (mAb) protein has been characterized at air-water interface. Protein aggregation due to mechanical agitation is a cause for concern in pharmaceutical industry due to the possibility of adverse effects with respect to patient safety. To understand the role of mechanical stresses at the air water interface and continuous renewal of interfacial area due to agitation, we have isolated the mechanical stress at the interface by using a Langmuir trough. Controlled compression-expansion cycles were applied to protein samples at different rates and durations. Surface pressure-area isotherms coupled with fluid imaging, and topographical imaging by AFM have confirmed that protein particle formation indeed initiates from the interface and only causes particle formation in bulk solution at higher rates/durations of compression-expansion cycles.

1.5. Table and figures

Panel C:

Force

Wilhelmy plate

w

d

Liquid sample

θ

$$\gamma = \frac{F}{l(cos\theta)}$$

$\gamma: surface\ tension$
$F: measuring\ force$
$l: perimiter\ of\ the\ plate$
$\theta: contact\ angel$

Panel D:

Surface tension

Intermolecular forces

Air

water
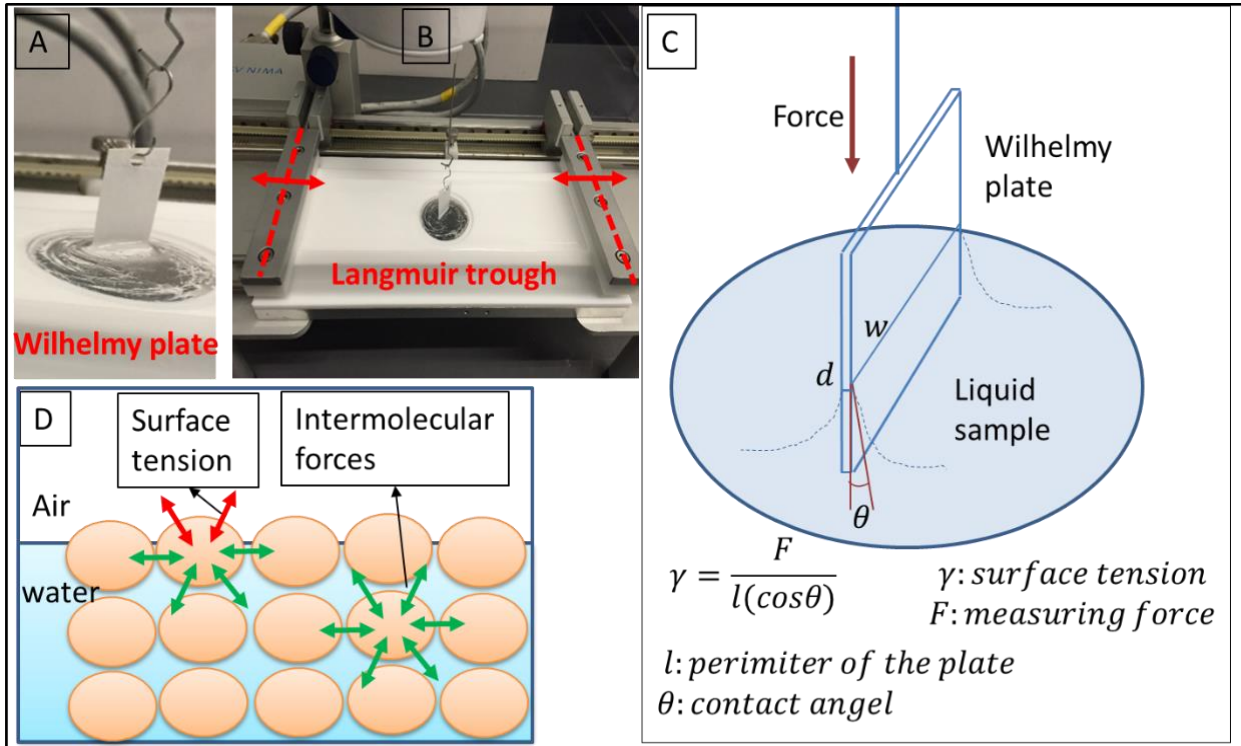
Figure1. Interfacial Characterization of surface energy: (A,B) Wilhelmy plate and Langmuir trough are commonly used to measure surface tension in a controlled surface area. (C,D) Wilhelmy plate is designed to measure the surface tension based on the interfacial forces.
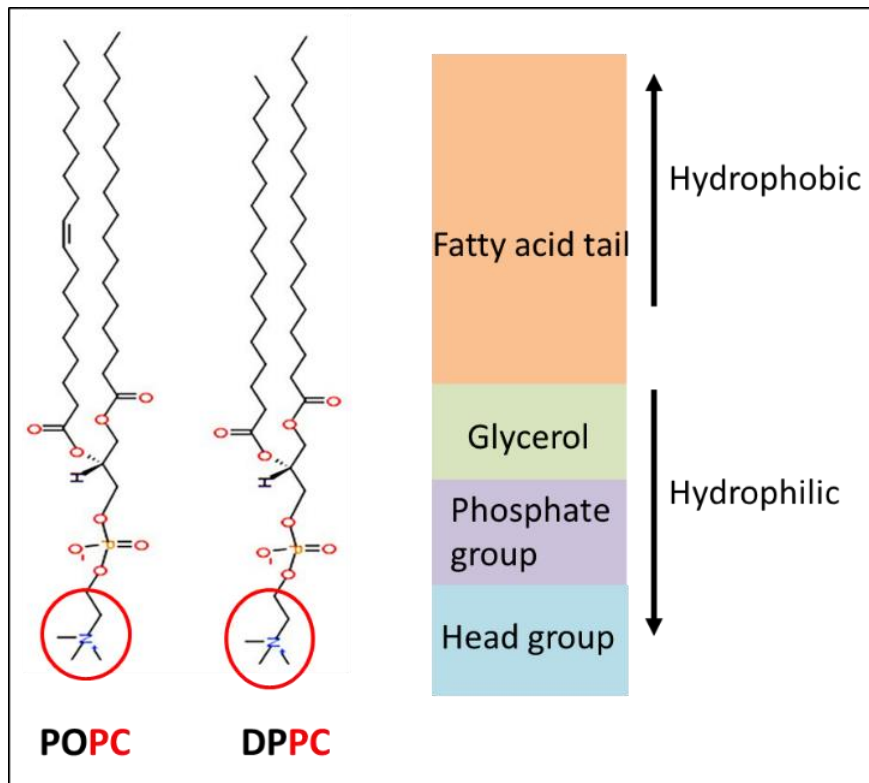
Figure 2. Phospholipid: head group moiety and alkyl tail. Head group: varies in size and charge, and the tail varies in saturated vs unsaturated.
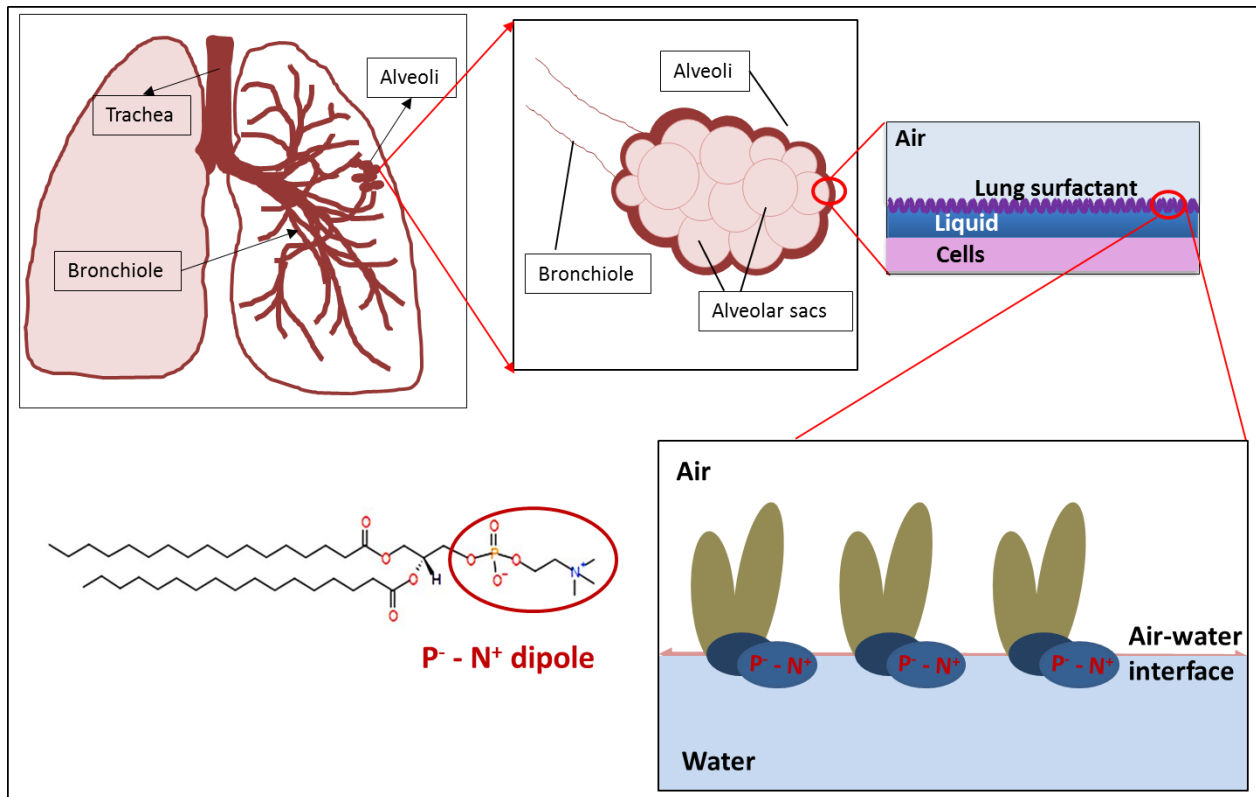
Figure 3. Natural lung surfactant is a mixture of lipid and proteins that line the alveoli cells in humans and other mammals. Lung surfactant minimizes the surface tension during continuous compression-expansion cycles and therefore minimized the work of breathing.
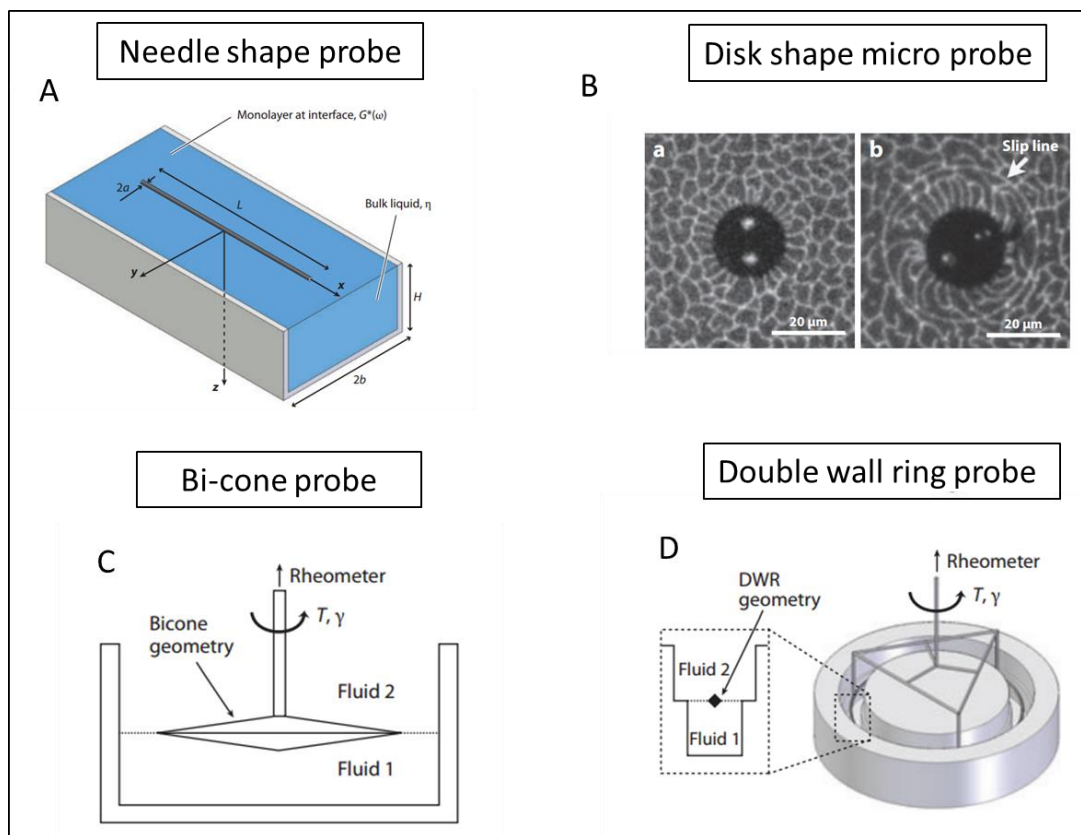
Figure 4. Interfacial shear rheometers vary in geometry and size of the probe. (A) Magnetic needle rheometer has been designed by Fuller group at university of Stanford. (B) Disk-shape magnetic probes (microbuttons) with "button holes" has been designed as microrheology probes by Squires and Zasadzinski at university of California. (C) The interfacial rheology system (IRS) that uses a bicone to shear the surface is commercially available. (D) Adopted double wall ring modified by Vermant and coworkers to increase the sensitivity [3, 17, 25, 26].

1.6. References

1. Barnes, G. and I. Gentle, *Interfacial science: an introduction*. 2011: Oxford University Press.
2. Barentin, C., et al., *Surface shear viscosity of Gibbs and Langmuir monolayers.* Journal of Fluid Mechanics, 1999. **397**: p. 331-349.
3. Fuller, G.G. and J. Vermant, *Complex fluid-fluid interfaces: rheology and structure.* Annual review of chemical and biomolecular engineering, 2012. **3**: p. 519-543.
4. Mendoza, A.J., et al., *Particle laden fluid interfaces: dynamics and interfacial rheology.* Advances in colloid and interface science, 2014. **206**: p. 303-319.
5. Saffman, P. and M. Delbrück, *Brownian motion in biological membranes.* Proceedings of the National Academy of Sciences, 1975. **72**(8): p. 3111-3113.
6. Takahashi, A., et al., *Structure-function relationships of bovine pulmonary surfactant proteins: SP-B and SP-C.* Biochimica et Biophysica Acta (BBA)-Lipids and Lipid Metabolism, 1990. **1044**(1): p. 43-49.
7. Notter, R.H., *Lung surfactants: basic science and clinical applications*. 2000: CRC Press.
8. Lee, K.Y.C., *Collapse mechanisms of Langmuir monolayers.* Annu. Rev. Phys. Chem., 2008. **59**: p. 771-791.
9. Alonso, C., A. Waring, and J.A. Zasadzinski, *Keeping lung surfactant where it belongs: protein regulation of two-dimensional viscosity.* Biophysical journal, 2005. **89**(1): p. 266-273.
10. Serrano, A.G. and J. Pérez-Gil, *Protein–lipid interactions and surface activity in the pulmonary surfactant system.* Chemistry and physics of lipids, 2006. **141**(1): p. 105-118.
11. Pérez-Gil, J., *Structure of pulmonary surfactant membranes and films: the role of proteins and lipid–protein interactions.* Biochimica et Biophysica acta (BBA)-Biomembranes, 2008. **1778**(7): p. 1676-1695.
12. Takamoto, D., et al., *Interaction of lung surfactant proteins with anionic phospholipids.* Biophysical journal, 2001. **81**(1): p. 153-169.
13. Ding, J., et al., *Effects of lung surfactant proteins, SP-B and SP-C, and palmitic acid on monolayer stability.* Biophysical Journal, 2001. **80**(5): p. 2262-2272.
14. Rodriguez, R., R. Martin, and A. Fanaroff, *Respiratory distress syndrome and its management.* Fanaroff and Martin's Neonatal-Perinatal Medicine: Diseases of the Fetus and Infant. 7th ed. St. Louis, MO: Mosby, 2002: p. 1001-1011.
15. El-Gendy, N., et al., *Delivery and performance of surfactant replacement therapies to treat pulmonary disorders.* Therapeutic delivery, 2013. **4**(8): p. 951-980.
16. Kim, K., et al., *Interfacial microrheology of DPPC monolayers at the air–water interface.* Soft Matter, 2011. **7**(17): p. 7782-7789.
17. Hermans, E. and J. Vermant, *Interfacial shear rheology of DPPC under physiologically relevant conditions.* Soft Matter, 2014. **10**(1): p. 175-186.
18. Zasadzinski, J., et al., *Atomic force microscopy of hydrated phosphatidylethanolamine bilayers.* Biophysical journal, 1991. **59**(3): p. 755-760.
19. Fainerman, V. and D. Vollhardt, *Equations of state for Langmuir monolayers with two-dimensional phase transitions.* The Journal of Physical Chemistry B, 1999. **103**(1): p. 145-150.
20. Vollhardt, D., V. Fainerman, and S. Siegel, *Thermodynamic and textural characterization of DPPG phospholipid monolayers.* The Journal of Physical Chemistry B, 2000. **104**(17): p. 4115-4121.
21. Takamoto, D.Y., et al., *Stable ordering in Langmuir-Blodgett films.* Science, 2001. **293**(5533): p. 1292-1295.
22. Sachan, A., et al., *Interfacial rheology of coexisting solid and fluid monolayers.* Soft Matter, 2017. **13**(7): p. 1481-1492.
23. Lee, M.H., et al., *Combined Passive and Active Microrheology Study of Protein-Layer Formation at an Air− Water Interface.* Langmuir, 2009. **26**(4): p. 2650-2658.

24. Krägel, J. and S.R. Derkatch, *Interfacial shear rheology.* Current Opinion in Colloid & Interface Science, 2010. **15**(4): p. 246-255.

25. Brooks, C.F., et al., *An interfacial stress rheometer to study rheological transitions in monolayers at the air− water interface.* Langmuir, 1999. **15**(7): p. 2450-2459.

26. Choi, S., et al., *Active microrheology and simultaneous visualization of sheared phospholipid monolayers.* Nature communications, 2011. **2**: p. 312.

27. Brenner, H., *Interfacial transport processes and rheology.* 2013: Elsevier.

28. Samaniuk, J.R. and J. Vermant, *Micro and macrorheology at fluid–fluid interfaces.* Soft matter, 2014. **10**(36): p. 7023-7033.

29. Espinosa, G., et al., *Shear rheology of lipid monolayers and insights on membrane fluidity.* Proceedings of the National Academy of Sciences, 2011. **108**(15): p. 6008-6013.

30. Kim, K., et al., *Effect of cholesterol nanodomains on monolayer morphology and dynamics.* Proceedings of the National Academy of Sciences, 2013. **110**(33): p. E3054-E3060.

31. Dhar, P., et al., *Autonomously moving nanorods at a viscous interface.* Nano letters, 2006. **6**(1): p. 66-72.

32. Dhar, P., et al., *Active interfacial shear microrheology of aging protein films.* Physical review letters, 2010. **104**(1): p. 016001.

33. Fischer, T.M., P. Dhar, and P. Heinig, *The viscous drag of spheres and filaments moving in membranes or monolayers.* Journal of Fluid Mechanics, 2006. **558**: p. 451-475.

34. Dhar, P., et al., *Autonomously moving local nanoprobes in heterogeneous magnetic fields.* The Journal of Physical Chemistry C, 2007. **111**(9): p. 3607-3613.

35. Kiese, S., et al., *Shaken, not stirred: mechanical stress testing of an IgG1 antibody.* Journal of pharmaceutical sciences, 2008. **97**(10): p. 4347-4366.

36. Bee, J.S., et al., *Production of particles of therapeutic proteins at the air–water interface during compression/dilation cycles.* Soft Matter, 2012. **8**(40): p. 10329-10335.

37. Shieh, I.C. and A.R. Patel, *Predicting the agitation-induced aggregation of monoclonal antibodies using surface tensiometry.* Molecular pharmaceutics, 2015. **12**(9): p. 3184-3193.

38. Rudiuk, S., et al., *Importance of the dynamics of adsorption and of a transient interfacial stress on the formation of aggregates of IgG antibodies.* Soft Matter, 2012. **8**(9): p. 2651-2661.

39. Kamerzell, T.J., et al., *Protein–excipient interactions: Mechanisms and biophysical characterization applied to protein formulation development.* Advanced drug delivery reviews, 2011. **63**(13): p. 1118-1159.

40. Khan, T.A., H.-C. Mahler, and R.S. Kishore, *Key interactions of surfactants in therapeutic protein formulations: a review.* European Journal of Pharmaceutics and Biopharmaceutics, 2015. **97**: p. 60-67.

Chapter 2: Monitoring Phases and Phase Transitions in Phosphatidylethanolamine Monolayers Using Active Interfacial Microrheology

Published:

Saba Ghazvini[1], Brandon Ricke[1], Joseph A. Zasadzinski[2] and Prajnaparamita Dhar[1]*

[1] Department of Chemical Engineering, University of Kansas, Lawrence KS 66045.

[2] Chemical Engineering and Materials Science, University of Minnesota, Minneapolis, Minnesota 55455.

2.1. Introduction

Phosphatidylethanolamines (PE) make up a substantial fraction of the lipids in the central nervous system, such as the white matter of brain, nerves, neural tissue, and in the spinal cord. In contrast to phosphatidylcholine, PE is concentrated with phosphatidylserine in the inner or cytoplasmic monolayer of the plasma membrane [1]. PE is also the dominant lipid in bacterial cell membranes; specific interactions with PE are often essential to development of new antimicrobial medications [2]. PE and other phospholipid monolayers exhibit a range of structural polymorphs [3] that can be readily accessed in a Langmuir trough by altering the area occupied by a fixed number of molecules at the air-water interface. Understanding the structure-property relationships of Langmuir films provides insight into the properties of PE in biomembranes as well as in a variety of liquid-vapor interfaces common to the chemical, petroleum, and food industries [4]. Often, the goal in these studies is to determine how the shape, size and chemical features of the molecules that make up the films influence the organization, range and perfection of molecular ordering, and how these change with surface pressure and temperature.

Modern grazing incidence synchrotron X-ray diffraction (GIXD) has become a preferred method to determine molecular packing in different phases as well as the extent of molecular order, and how these change at phase transitions [5, 6]. However, well before the development of synchrotron X-ray sources, Harkins and coworkers showed that monolayer rheology could identify phase transitions or molecular rearrangements that were not obvious from Langmuir isotherms [7]. Slight differences in the molecular lattice or molecular tilt are often accompanied by significant changes in the surface viscosity of fatty acid [8] and fatty alcohol [9, 10] films. Similar changes in surface rheology are expected at phase transitions in phospholipid monolayers [11]; in particular, second order phase transitions in phospholipid monolayers are difficult to detect from Langmuir isotherms and involve only subtle changes in X-ray diffraction patterns [5]. However, the

interfacial rheology of these biologically relevant films has not been systematically examined due to their much lower surface viscosity and elasticity.

The smaller the surface viscosity, the harder it is to decouple the response of the two-dimensional interfacial film from that of the three-dimensional subphase [12-17]. This decoupling is quantified by the Boussinesq number, B, which is the ratio of surface to bulk drag on a probe of characteristic dimension, a (here the length of the nanorod):

$$B = \frac{\eta_s}{(\eta_w + \eta_a)a} \approx \frac{\eta_s}{\eta_w a} \tag{1}$$

η_s is the surface viscosity; η_w and η_a are the bulk viscosities of water and air ($\eta_w \gg \eta_a$). Reliable measurements of surface viscosity require $B \gg 1$. Detailed analysis by Reynaert et al. show that current surface rheometers with macroscopic probes [18-20] (such as those used by Harkin and others), can be used to measure $\eta_s > 10^{-6}$ N-s/m [21]. Since phospholipid films in the liquid-expanded (LE) phase have surface viscosities of 10^{-9} N-s/m or lower [14-17, 22-24], the LE phase is inaccessible to macroscopic interfacial rheometers. As a result, the flow behavior of a significant portion of the phospholipid monolayer phase space remains unexplored. Introduction of new passive and active microrheology techniques using micron and even nanometer size probes [25] have increased the sensitivity of interfacial rheometers, the geometric ratio of our probes being 10^{-3}, [26-31] by two to three orders of magnitude [14-17], making the current work possible.

The reorientation of a nickel nanorod (diameter = 300nm, length ~ 3-50 μm) due to an externally applied magnetic field was used to measure surface viscosity and detect elasticity. The nanometer dimensions of the probe decreases a and increases B for a given value of η_s in Eqn. 1, allowing reliable measurements of surface viscosity as low as 10^{-9} Ns/m. By extending the Fischer model for analyzing the motion of an object at an interface with a finite immersion depth [32] to the motion of infinitely thin cylinders at an interface, it is possible to relate the drag on a nanorods

to the Boussinesq number, and hence, the surface viscosity[29] . Increasing the applied external torque allows measurements of η_s of 10^{-5} Ns/m or higher. Here we present the surface viscosity of two phosphatidylethanolamine monolayers, DLPE and DMPE, over a range of surface pressures that include the liquid expanded (LE) phase, liquid condensed (LC) phase and the LC-solid (S) phase transition, using a recently developed magnetic nanorod microrheometer [26]. DLPE and DMPE have identical headgroups and differ by two CH2 groups per alkyl chain, which leads to significant difference in the surface pressure at which phase transitions occur. Detailed structural characterization by grazing incidence X-ray diffraction and surface pressure-area isotherms and morphological information of both DLPE and DMPE are available [5, 33], allowing us to correlate our surface viscosity measurements with molecular structure.

We find that the surface viscosity of both DLPE and DMPE undergo several orders of magnitude change in surface shear viscosity with surface pressure in the LC and S phases. The measured surface viscosity does not change with surface pressure in the LE phase, suggesting that it is below our sensitivity limit of $\sim 10^{-9}$ N-s/m. However, the first order LE-LC phase transition is accompanied by a measurable, discontinuous jump in the surface viscosity, and the surface viscosity increases exponentially with surface pressure in the LC phase. The second order transition from LC to S phase in both DMPE and DLPE is accompanied by an abrupt appearance of elasticity in the film. The second order LC-S phase transition in PE films is easy to miss in isotherms, but synchrotron X-ray diffraction shows that the molecular tilt disappears at the LC-S transition for DMPE [5, 34] (see Supplemental Materials). However the dramatic onset of elasticity makes the transition macroscopically obvious. It is not clear if the untilting (and the transition to hexagonal from orthorhombic symmetry) is sufficient to create a jump in monolayer elasticity or

if the untilting is accompanied by a change in headgroup ordering due to enhanced hydrogen bonding between PE headgroups, which cannot be detected by X-ray diffraction.

2.2. Materials and Methods

HPLC grade chloroform solutions of 1,2-dilauroyl-sn-glycero-3-phosphoethanolamine (DLPE) and 1,2-dimyristoyl-sn-glycero-3-phosphoethanolamine (DMPE) were purchased from Avanti Polar Lipids, Alabaster, AL, and used as received. Texas Red® 1,2-dihexadecanoyl-*sn*-glycero-3-phosphoethanolamine, triethylammonium salt, (TXR-DHPE) was purchased in the dried form from Life Technologies (Invitrogen) and dissolved in HPLC grade chloroform. All organic solvents were purchased from Fisher Scientific. The subphase water (resistivity 18.2 MΩ/cm) was prepared using a Millipore Gradient System (Billerica, MA). The lipids were stored at -20 $^{\circ}$C when not in use.

Surface tension and surface compressibility modulus: A filter-paper Wilhelmy plate on a Langmuir trough (KSV-NIMA, Biolin Scientific) was used to measure the surface pressure as a function of area occupied by the phospholipid molecules. The 2-D isothermal bulk modulus, β, is the inverse of the isothermal compressibility modulus κ: $\beta = -A \left(\frac{\partial \Pi}{\partial A} \right)_T = A \left(\frac{\partial \gamma}{\partial A} \right)_T = \frac{1}{\kappa}$

For a monolayer, the surface compressibility modulus is a measure of the ability of the monolayer to store mechanical energy as stress. Both β and κ are related to the second derivative of the free energy, G, ($\gamma = (\frac{\partial G}{\partial A})_T$, $\beta = A(\frac{\partial^2 G}{\partial A^2})_T$), which means that $b \rightarrow 0$ (or $\kappa \rightarrow \infty$) at the first order LE-LC transition. At a second order LC-S phase transition, the area/molecule, A, is continuous, but β changes discontinuously. The compressibility modulus was calculated from the isotherm data by taking numerical derivatives of the surface pressure vs. molecular area isotherms using the

Differentiate tool in the Origin 8.6 graphical plotting software. The numerical derivatives were smoothed with a Fourier filter using 5 points.

Active Microrheology: The nickel nanorods used as probes were synthesized by electrochemical deposition of nickel into alumina templates [35], then magnetized, thoroughly cleaned, and dispersed in a 90% isopropyl alcohol, 10% water solution [26]. A 1 mg/ml solution of DLPE or DMPE with 1 wt% of TXR-DHPE in chloroform was used as a spreading solution. To initiate each experiment, 20-40 µl of the rod solution was deposited uniformly using a micropipette at the air/water interface in a Langmuir trough. This concentration of nanorods would allow an average of two nanorods in each 150 µm×150 µm scale that the videos are taken. The isopropyl alcohol was allowed to evaporate for 45 minutes; a population of nanorods was retained at the interface by capillary forces. Next, the DLPE or DMPE /TXR-DHPE spreading solutions were added drop-wise from a micro-syringe onto the air/water interface, and the chloroform allowed to evaporate for 20 minutes. The films were compressed to the desired surface pressure using the barriers of the Lanmguir trough. Two sets of home-built electromagnetic coils, oriented perpendicular to each other, were used to apply an external magnetic field (10 G – 120 G) to orient the nanorods. Initially only magnetic field at one axis is on next that axis is turned off and the other axis is on making the rod reorient in toward new magnetic field. Individual rods were visualized with a Nikon E3800 microscope using a 50x long working distance objective. Videos of the rod reorientations were recorded with a CCD camera connected to a personal computer and digitized for analysis [26]. At each surface pressure a minimum of two data analysis has been done to assure the accuracy of surface viscosity value.

Analysis of nanorod motion: The orientation of a magnetic nanorod (length l, magnetic moment $\mu_o m$) due to an externally applied magnetic field, **H,** can be described by the angle, $j\left(t\right)$, between

the long axis of the rod and the direction of the applied field (the applied field direction is defined to be $\jmath = 0$). In a purely viscous medium, the magnetic field provides the torque needed to align the rod, which is resisted by the viscous drag on the rod [26]:

$$\mu_0 m H \sin\varphi = -f_r \eta_w l^3 \frac{d\varphi}{dt} \qquad (2)$$

the solution to which is:

$$\tan(\varphi/2) = \exp\left(-\frac{t}{\tau}\right) \qquad (3)$$

The relaxation time, $\tau = \frac{f_r \eta_w l^3}{\mu_0 m H}$, gives the dimensionless drag coefficient of the rod, $f_r = f_w + f_s$, which is a sum of the bulk (f_w) and surface (f_s) drag. The magnetic moment of the rod can be written in terms of the magnetization, M, and the rod aspect ratio, l/r, which gives the relaxation time, τ, as:

$$\tau = \frac{f_r \eta_w l^3}{\mu_0 m H} = \frac{f_r \eta_w l^3}{\mu_0 M V H} = \frac{f_r \eta_w l^3}{\mu_0 M \pi r^2 l H} = \frac{f_r \eta_w}{\mu_0 M \pi H} \left(\frac{l}{r}\right)^2 \qquad (4)$$

The magnetization of rods was calibrated by averaging the motion of several nanorods in water and glycerol solutions [29, 36, 37] and the average value of magnetization was used for all subsequent experiments. The relaxation time τ, was obtained by fitting equation 3 to the measured values of rod orientation obtained by analyzing digitized videos of the rod motion using a particle tracking program and Origin 8.6. The subphase drag, f_w, is taken to be equal to half that of the drag on a rod of radius r and length l (for $l/r \geq 20$) rotating in a viscous fluid [29, 36, 37]:

$$f_w = \frac{\pi}{6[\ln(\frac{l}{r} - 0.8)]} \qquad (5)$$

Typically, $f_s \gg f_w$ in these experiments, suggesting that the measurements are sensitive to the interfacial stresses. The rod axial ratio, l/r, is the only relevant parameter needed to calculate f_w.

For each value of τ, f_s was calculated by subtracting f_w from f_r. The relationship between the Boussinesq number, B, for a given f_s for an incompressible interfacial film was determined in Dhar et al. [29] and used to calculate the surface viscosity using Eqn. 1.

Elasticity, E_s, in the film adds a term proportional to $E_s\varphi$ to the right hand side of Eqn. 2, such that the torque balance equation now becomes:

$$\mu_0 mHsin\varphi = -f_r\eta_w l^3 \frac{d\varphi}{dt} + E_s(\frac{\pi}{2} - \varphi) \qquad (6)$$

A finite elasticity causes the rod to "stall" ($\frac{d\varphi}{dt} \to 0$) at a non-zero angle where the elastic force is balanced by the magnetic torque (note that the magnetic torque goes to zero as $\varphi \to 0$ in Eqns. 3 and 5) [27, 38, 39]. To detect elasticity, as well as any anisotropic contribution from the monolayer microstructure, torques were applied in both the x and y direction. For purely viscous monolayers, the reorientation curves superimposed, the rod comes to rest aligned with the applied magnetic field ($\varphi \to 0$), and the measured reorientation rate is well described by Eqn. 3 (Fig. 5). However, for viscoelastic monolayers, the reorientation in different directions did not

overlap, suggesting anisotropic ordering in the monolayer. The rod never aligned with the applied field ($\varphi > 0^o$ for $t \to \infty$ in Fig. 5), and Eqn. 3 did not fit the relaxation rate data.

2.3. Results and Discussion

Figure 1a shows a representative surface pressure, $\Pi=\gamma_o-\gamma$, (γ_o =72 mN/m for water, γ is the measured surface tension) vs. molecular area isotherm of a DLPE (black curve) and DMPE (red curve) monolayers. As the area available to the monolayer is reduced, Π increases from zero, and the monolayer enters the disordered, liquid-expanded (LE) phase [40]. For the DLPE monolayer,

continued compression causes the surface pressure to increase smoothly leading to a plateau at Π_c ~ 37 mN/m. DMPE (with two more methyl groups per chain than DLPE) plateaus at Π_c~ 7 mN/m. At Π_c, decreases in the area/molecule occur at a *nearly* constant surface pressure, which defines the LE-LC coexistence [3, 41]. Compression beyond the LE-LC coexistence plateau to surface pressures greater than Π_c results in an almost linear increase in the isotherm in the LC phase. In the LE phase at surface pressures below Π_c, there is steady increase in the bulk modulus, β, with decreasing area/molecule (Fig. 1b). However, at the LE-LC coexistence, β goes to zero, consistent with a first order phase transition. β also undergoes a rapid linear increase with decreasing area/molecule and is significantly larger in the LC phase than the LE phase. GIXD of DMPE shows that these changes correlate with a decrease in the molecular tilt [4, 5]. The correlation length, which is a measure of the extent of the crystalline domains, also increases monotonically with increasing surface pressure [5]. A kink in the slope of the isotherm at Π_s, which is visible in DMPE isotherms but not DLPE, marks the second-order transition to the solid (S) phase in DMPE. Similarly, a small step in β at the same as Π_s is shown in Figure 1b. GXID [34] shows that the tilt of the alkane chains of DMPE goes to zero at a surface pressure of ~ 35 mN/m, accompanied by a significant increase in the positional order (correlation length, ζ) from around 10 to 50-70 lattice spacings in DMPE films [5].

Figure 2 shows representative fluorescence microscopy images of the DLPE and DMPE monolayers; contrast in the images is due to the partitioning of 1 wt % Texas Red-DHPE into the disordered LE phase [42]. At surface pressures below Π_c, the LE phase is homogeneously bright, consistent with a uniform distribution of the fluorescent lipid in the disordered monolayer. The lack of any GIXD reflections in this phase is consistent with a lack of positional order [5]. As the surface pressure is increased, flower shaped or snowflake-shaped dark domains of LC phase start

to nucleate, suggesting the presence of two-dimensional pseudo-hexagonal order. Contrast in these images is due to the greater solubility of the Texas Red-DHPE in the disordered LE phases compared to ordered LC phases [43-45]. With increasing compression or decreased mean molecular area in the LE-LC coexistence region, the LC domains grow in size but not in number at the expense of the LE phase; the snow-flaked shaped dark domains of DMPE grow via tip splitting until the tips start touching, at which point the domains grow in width. Compression in the LC region causes the dark LC domains to grow such that they are in contact with each other causing the appearance of uniformly dark films. No change in appearance occurs at Π_s; conventional fluorescence microscopy cannot detect this second-order phase transition between ordered phases.

Figure 3a (squares) presents the total friction factor, $f_r = f_w + f_s$, determined from the analysis of the characteristic time for rod rotation (Eqns. 3,4) as a function of surface pressure for a DLPE monolayer, along with the corresponding subphase friction factor, f_w (circles). Figure 3a shows

that for $\Pi < \Pi_c$, f_r is not significantly larger than f_w. It is not possible to determine the absolute value of surface viscosity in this regime, except to say that $\eta_s \leq 10^{-9}$ N-s/m, the limit of sensitivity of the rheometer ($Bo \sim 1$, Eqn. 1). Figure 3b shows the calculated values of surface viscosity as a function of surface pressure determined from f_s from Fig. 3a. Within the experimental error, η_s does not change with increasing surface pressure in the LE phase up to $\sim$ 35 mN/m. However, there is an exponential increase in f_r for $\Pi > \Pi_c$, making $f_r >> f_w$, and the drag on the probe is primarily due to η_s. Between 36 and 39 mN/m, η_s increased by nearly two orders of magnitude, corresponding to the first order LE-LC phase transition. At coexistence, the measured surface

viscosity varied much more than in either the LE or LC phases (large error bars in Fig. 3b). This is likely due to the location of the nanorod probes relative to the coexisting LE or LC domains (Fig. 2); the location of the probes can lead to differences in the local viscosity, as the rods are about the size of individual domains. In the LC phase, η_s increases exponentially up to $\Pi \sim 41$ mN/m at which $\eta_s \sim 10^{-6}$ Ns/m. Increasing the surface pressure further causes the rods to stop rotating entirely, consistent with an onset of surface elasticity (Eqn. 6). However, the isotherm in Fig. 1 shows no evidence of an LC-S transition in DLPE.

The LC phase is much more extensive in DMPE at room temperature, and the LC-S transition more obvious, making it more accessible to the rheometer (Fig. 4). As was the case for DPLE, Figure 4a shows that for $\Pi < \Pi_c$, $f_r \sim f_w$, while for $\Pi > \Pi_c$, $f_r >> f_w$. At $\Pi \sim \Pi_c$, there is an order of magnitude jump in f_r and η_s (Figure 4a and b between 7 and 8 mN/m), corresponding to the LE-LC phase transition. For $\Pi > \Pi_c$, GIXD reveals distinct reflections indicating a two dimensional semi-crystalline ordering in the LC phase [5, 34]. Similar discontinuous changes in η_s were previously reported in fatty acid/alcohol monolayers at first order phase transitions from less ordered to more ordered phases [8, 9]. However, this discontinuity in the surface viscosity in a phospholipid monolayer has not been quantified before, as the surface viscosity at the LE-LC phase was beyond the sensitivity limit of macroscopic rheometers [18, 46, 47].

Between Π_c and Π_s, the surface viscosity increased exponentially with surface pressure, similar to DPPC, and mixed DPPC and cholesterol monolayers [39, 46, 48, 49]. However, even with the greatly increased surface viscosity, we were unable to detect any elasticity within the LC phase. The rod orientation decays exponentially with time (Eqn. 3) as expected for a purely viscous system (Fig. 5, circles), the rod aligns with the applied field at long times, and the decay curves

overlap for perpendicular directions of applied torque (Supplemental Information). This overlap in the two decay curves also indicates that the rod motion did not damage structures in the film [39].

However, for $\Pi > \Pi_s \sim 34$ mN/m, the rod reorientation dynamics were not consistent with Eqn. 3 (Figure 5). The rod no longer reoriented parallel to the direction of the magnetic field, but stalled; $\tan(\varphi/2)$ did not decay to zero as would be expected from Eqn. 3 (circles). Further increases in surface pressure caused the rod to be completely immobile. These alterations in the rod response indicate an elastic contribution to the film in the S phase. GIXD of DMPE shows a transition from a tilted to untilted molecular orientation at Π_s [5, 34]. The translational order parameter increased gradually from ~ 10 lattice spacings at Π_c to ~50-70 lattice spacings at Π_s [5]. Helm et al. suggest that the LC-S transition may be accompanied by a dehydration and ordering of the lipid head groups, in addition to the elimination of molecular tilt [5]. The abrupt appearance of elasticity in the monolayer shows that the LC-S transition is likely not just an elimination of tilt, but requires a significant change in the intermolecular interactions such as an ordering of the lipid head groups. Kim et al. reported that dipalmitoylphosphatidylcholine (DPPC) films at surface pressures between 12-14 mN/m also showed an onset of an exponential increase in elasticity that could correspond to a possible LC-S transition [38]. The slope of the surface viscosity vs. surface pressure also showed a change in slope at surface pressures between 12-14 mN/m, consistent with a second order phase transition [38]. However, it is difficult to see any kink in DPPC isotherms, and DPPC molecules remain tilted at all surface pressures [50], which suggests that the LC-S transition likely involves the head group ordering rather than the tilt of the tail groups.

The exponential increase in surface viscosity with surface pressure in the LC phase is consistent with the free area model previously used to correlate surface viscosity in DPPC[39, 49,

51, 52] and DPPC-cholesterol [53] films. Figure 6a-b represent a correlation of the surface viscosity with the free-area model [51]. The free area model is the two-dimensional analog of the classic free volume model developed to describe liquid viscosities [54] and is given by:

$$\ln \eta_s = \ln \eta_s^0 + \frac{BA_0}{A_f}$$

(7)

The free area, A_f, is the difference between the measured area/molecule, A at a given Π, and the close-packed area/molecule, A_0: $A_f = A(\Pi)-A_0$. The parameter B in Eqn. 7 accounts for overlaps of free volume in the original theory and ranges from $1/2 \leq B \leq 1$ [54]. We find that the value of B makes little difference in the important fitting parameters of the model, so we set $B = \frac{1}{2}$ and used A_0 and $\ln \eta_s^0$ as the two fitting parameters in Fig. 6. Table 1 shows that the values of the close-packed molecular area, A_0, determined from the fits of the free area model to the surface viscosity for both DLPE and DMPE LC phases correspond nearly exactly with the area/molecule at the maximum compressibility (monolayer collapse) in Fig. 1b. This excellent agreement between the area/molecule at the maximum compressibility and A_0 is consistent with the basic assumptions used to derive the free area and free volume models [54]. The free area model also correlates the limited surface viscosity data we have obtained in the LE phase of DMPE (Fig. 6).

2.4. Conclusions

We present the detailed measured surface rheology of phosphatidylethanolamine monolayers in the LE, LC and S phases, and the discontinuities in surface viscosity at the LE-LC first order phase transitions. Over much of the disordered LE phases of DLPE and DMPE, the surface viscosity is $< 10^{-9}$ Ns/m, which is below the sensitivity of the magnetic nanorod viscometer. However, for both DLPE and DMPE, the surface viscosity undergoes a discontinuous jump at the

LE/LC phase transition, consistent with a first order phase transition and the onset of semi-crystalline order in the LC phase (Fig. 2). Within the LC phase, the surface viscosity increases exponentially with surface pressure (or decreasing area per molecule), with negligible surface elasticity. The surface viscosity in the LC phase of both DLPE and DMPE fit the free area model, with excellent agreement between the closed packed area/molecule predicted by the free area model and that given by the maximum in monolayer compressibility at monolayer collapse, even though the LC phase in DLPE only exists over a narrow range of surface pressure at room temperature.

A kink in the DMPE isotherm signifies an LC-S phase transition for $\Pi \sim 34\text{-}35$ mN/m, and is accompanied by an abrupt onset of elasticity in the monolayer. GIXD shows that the molecular tilt in DMPE is eliminated at the LC-S transition, this transition between orthorhombic and hexagonal molecular packing may be the origin of the elasticity. The elimination of molecular tilt shows that the area occupied by the PE headgroup matches the area occupied by the crystalline alkane chains at the LC-S transition. We also observed an abrupt onset of surface elasticity in DLPE at ~40-41 mN/m, although no kink was observed in the DLPE isotherm. As DLPE and DMPE are chemically identical except for a two methyl group difference in chain length, we expect that DLPE also untilts at the LC-S transition as the areas occupied by the headgroup and crystalline alkane chains should be nearly identical to DMPE. However, we are not aware of any GIXD data on DLPE with which we can validate this hypothesis.

Interfacial microrheology is a sensitive tool to detect phase transitions and critical parameters in phospholipid films that are less obvious from isotherms. The correlation of elasticity with the elimination of molecular tilt in DMPE suggests that there is a previously unknown LC-S transition in DLPE. Interfacial rheology can be extremely useful in examining phase transition and molecular

42

arrangements in monolayers that are difficult to examine by GIXD and its relative simplicity allows for a much wider and more detailed examination of phospholipid monolayer structure.

2.5. Table and figures

	A_0(free area model) Å^2/molecule	A_0 (max. compressibility) Å^2/molecule	η_{s0} (nNs/m)
DLPE	43.6(1.4)	44.6	0.005
DMPE	40 (0.5)	40.6	6.11

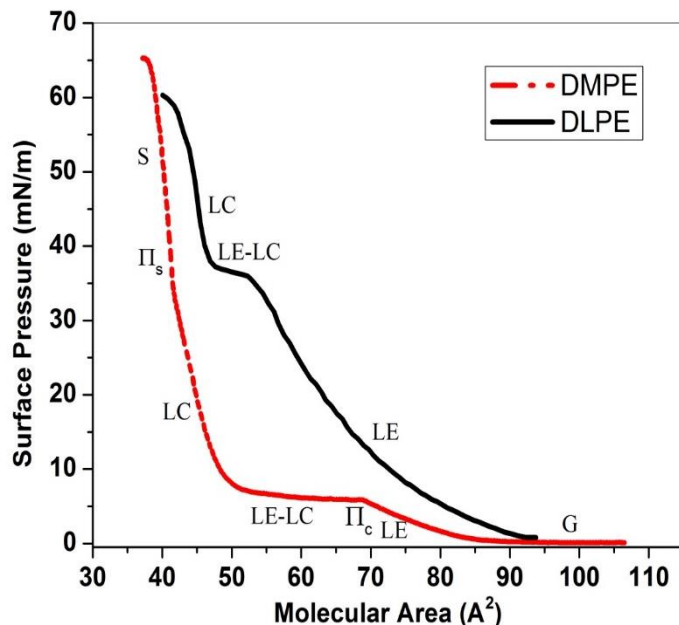**Table 1:** Fitting parameters from the free area model

Figure 1a. Surface pressure vs. molecular area isotherm of DLPE(straight black line) and DMPE (dash red line) show the progression from a "gaseous" phase (G) at high areas per molecule to a liquid-expanded (LE) phase as the film is compressed (i.e. molecular area decreased) as reflected in the lift-off of the isotherm from π=0. The LC phase is nucleated at $\pi_C \sim 37$ mN/m for DLPE and $\pi_S \sim 7$ mN/m for DMPE; further compression causes the LC phase to grow at the expense of the LE phase at roughly constant surface pressure. This coexistence plateau in the isotherm marks the first-order LE-LC transition. At the end of the plateau, compression rapidly increases the surface pressure in the LC phase and is related to a decrease in the molecular tilt and an increase in the crystalline order in the film. The second-order LC-solid (S) transition of DMPE corresponds to a kink in the isotherm and an increased slope at $\pi_S \sim 34$ mN/m.
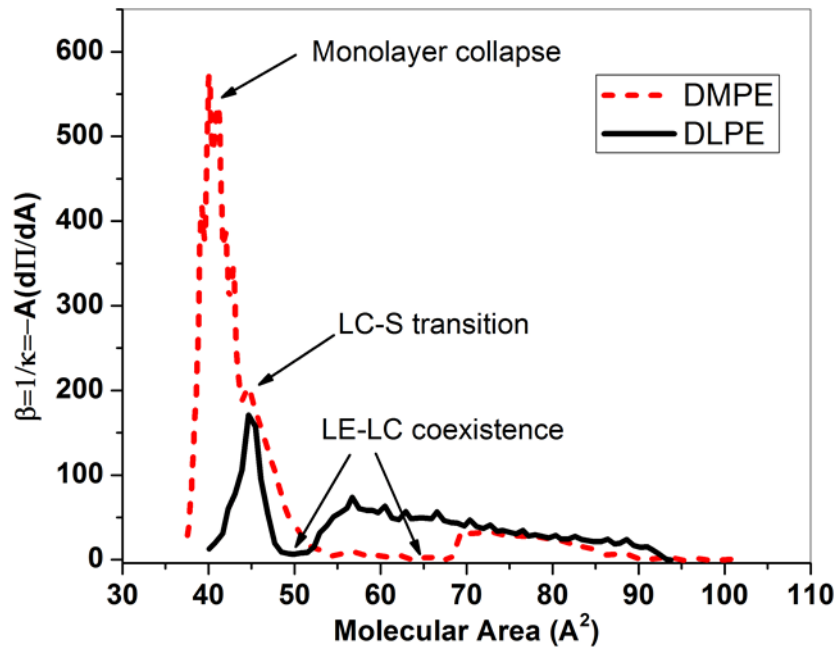
Figure 1b. Smoothened surface compressibility modulus vs. molecular area isotherm of DLPE (straight black line) and DMPE (dash red line) shows increasing compressibility modulus at the onset of the LE phase, and a sudden dip in the curve at values corresponding to the LE-LC coexistence plateau. A small discontinuity in the compressibility of DMPE corresponds to the kink in the surface pressure vs. area isotherm. The peak in the curves correspond to the onset of monolayer collapse, this is the close packed limit for the stable monolayer.
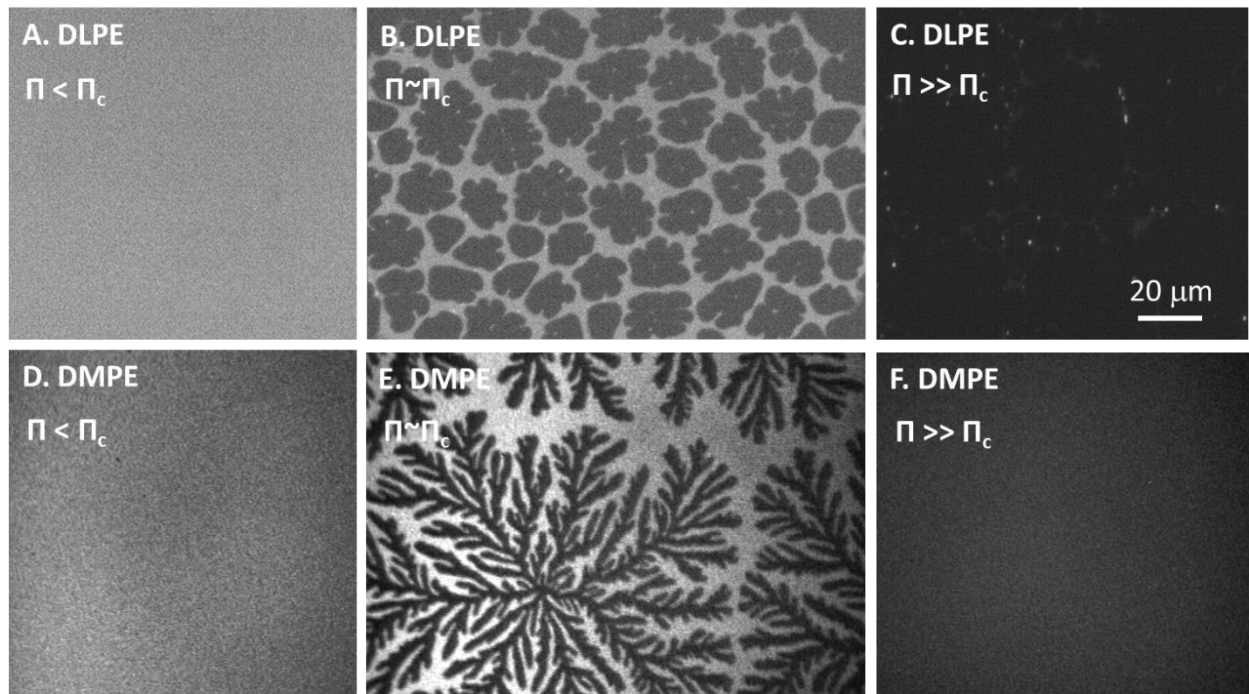
Figure2. The fluorescence micrographs of DLPE and DMPE at three different phases corresponding to the positions marked in the isotherm in Figure 1A. At $\pi < \pi_C$ (image A,D), the LE phase is uniformly fluorescent due to high solubility of the lipid dye in the disordered monolayer. At π_C (image B, E) the LC phase nucleates as dark, multiple-armed structures (the better ordered LC phase excludes the lipid dye) in a bright, unstructured, continuous LE phase in which the lipid dye is concentrated. For $\pi > \pi_s$ (image C,F), both the LC and S phases are uniformly dark without distinguishable domains (the S phase also excludes the lipid dye); no changes in the images occur at π_s.

Figure 3a. The total friction factor, f_r and the friction factor due to the subphase water, f_w on a half-immersed rod at the air/lipid interface vs. surface pressure for DLPE samples. The total friction factor has been calculated using Eqn.3 in text. Below a surface pressure of $\pi_C \sim 37$ mN/m, the monolayer is in the liquid expanded phase and has a low friction factor close to the f_w. Increasing the surface pressure above π_C, the f_r is orders of magnitude higher than the f_w. In the LE region, $f_r \sim f_w$, indicating that there is no measureable viscosity change in this phase. The first order LE- LC transition is indicated by a sudden increase of f_r, indicating a corresponding reliable increase in the surface stresses. f_r values have been used to calculate the surface viscosity plotted in the Figure 3b, by using the theory of Fischer et al. for a infinitely thin cylinder at an interface.

Figure 3b. Surface viscosity vs. surface pressure for a DLPE monolayer. Below a surface pressure of $\pi_C \sim 37$ mN/m, the monolayer is in the liquid expanded phase and has a low viscosity consistent with the disordered molecular arrangements of the phase. Increasing the surface pressure above π_C causes a sudden increase in the surface viscosity at the first order LE- LC transition. Each data point is an average of surface viscosity of multiple rods, and the error bars is the standard deviation of the data. The significant error bars at LE-LC coexistence indicate the heterogeneity of the surface in the LE-LC phase. Further increases in surface pressure cause the surface viscosity to increase exponentially. At surface pressures above 41mN/m, the monolayer acted like a solid; the rod stalled, and did not turn at all with increase in magnetic field.
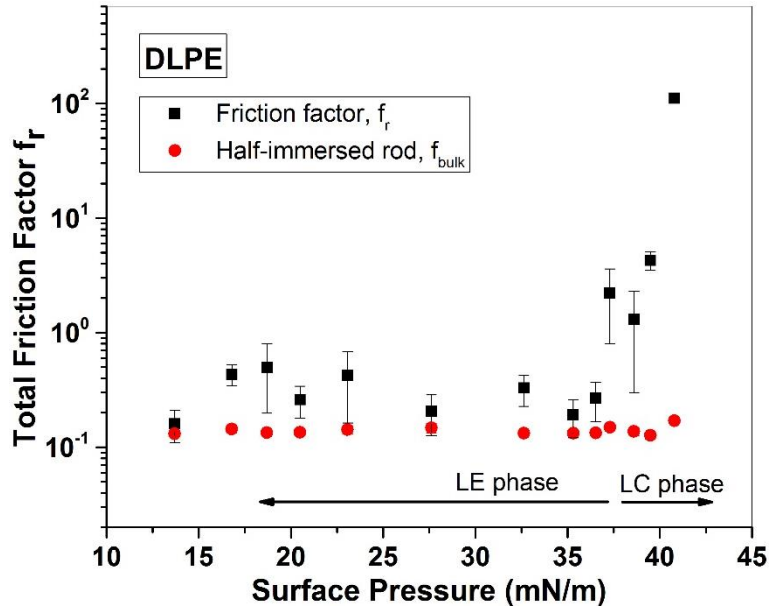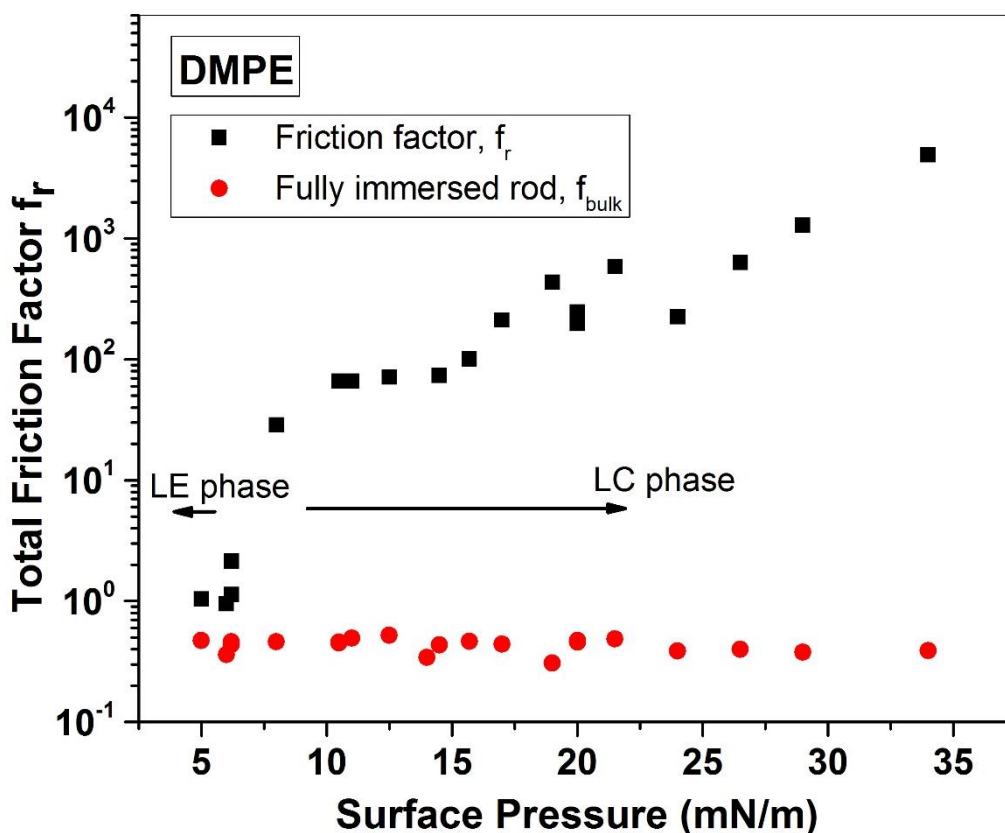
Figure 4a. The total friction factor, f_r and the friction factor due to the bulk water, f_w on a half-immersed rod at the air/lipid interface vs. surface pressure for DMPE films. The total friction factor has been calculated using Equ.3 in text. Below a surface pressure of $\pi_C \sim 7$ mN/m, the monolayer is in the liquid expanded phase and has a low friction factor close to f_w. Increasing the surface pressure above π_C, the f_r is orders of magnitude higher than the f_w. The first order LE- LC transition is indicated by a sudden increase of f_r and used to calculate the surface viscosity in Figure 4b.
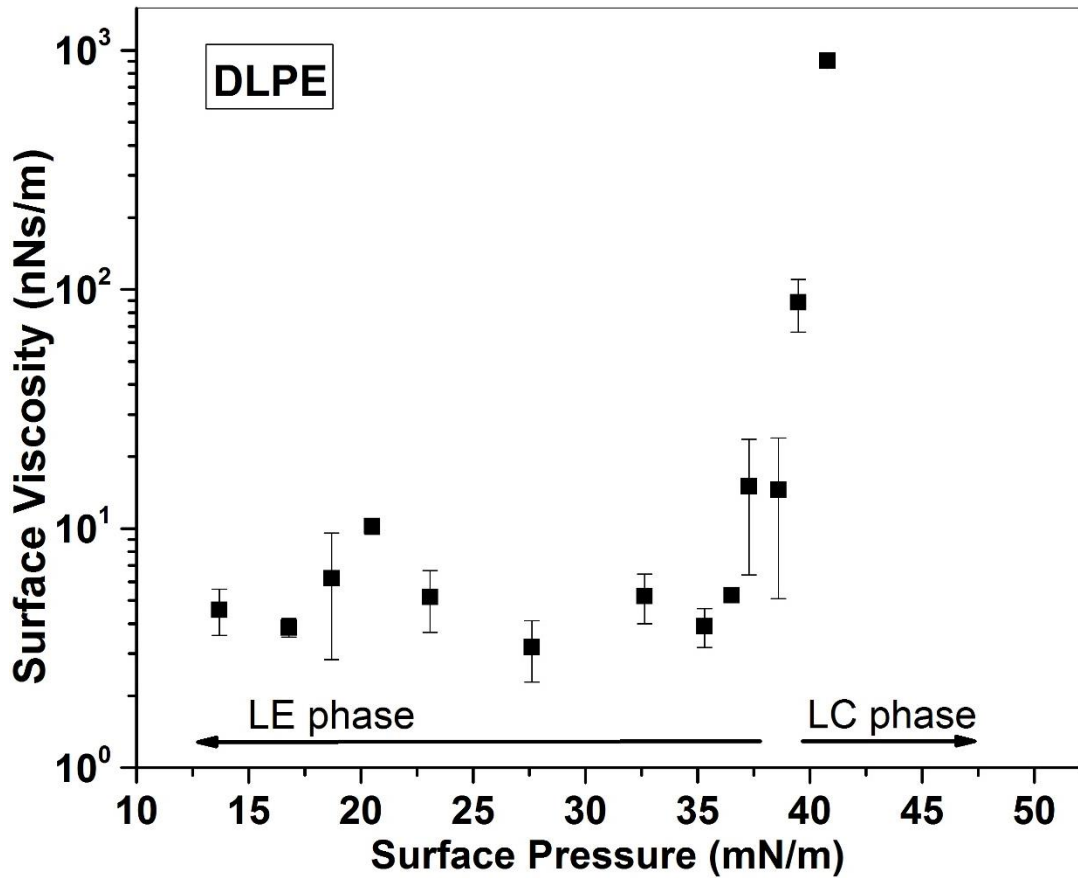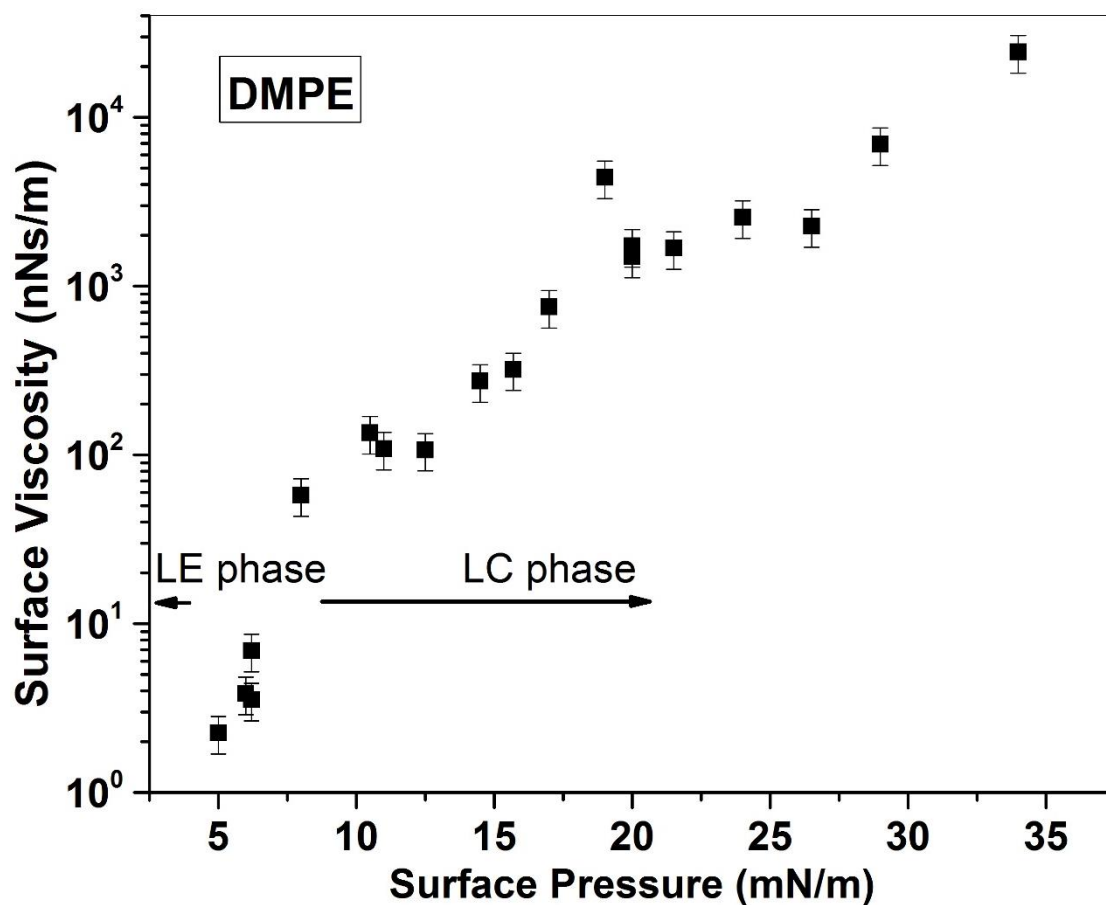
Figure 4b. Surface viscosity vs. surface pressure for a DMPE monolayer. Below a surface pressure of 6-7 mN/m, the monolayer is in the liquid expanded phase and has a low viscosity consistent with the disordered molecular arrangements of the phase. Increasing the surface pressure above 7 mN/m causes an order of magnitude increase in the surface viscosity at the first order LE- liquid condensed (LC) transition. This discontinuous change in the surface viscosity can be correlated with a sharp dip in the surface compressibility modulus of the monolayer. Further increases in surface pressure cause the surface viscosity to increase exponentially. At a surface pressure of 32-34 mN/m, the transition to solid (S) phase occurs, although the surface viscosity still increases linearly, the phase transition is marked by the appearance of elasticity in the monolayer (See Fig. 5).
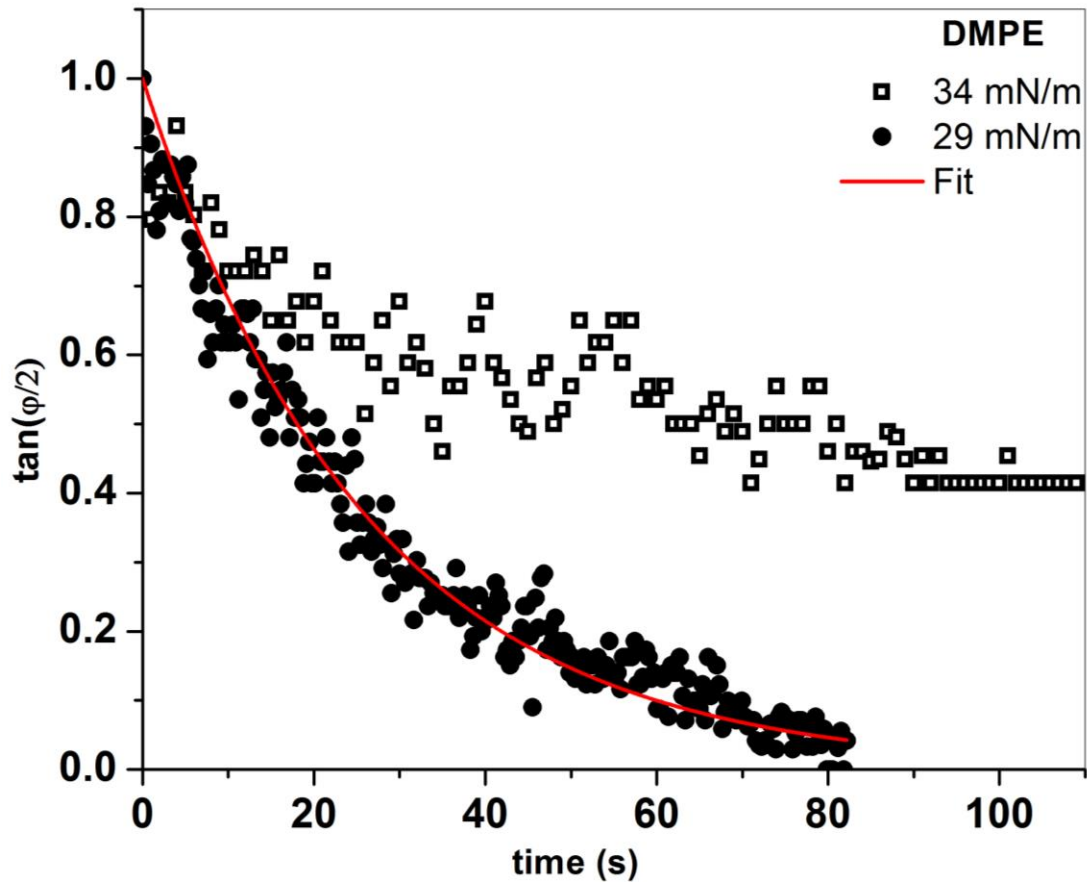
Figure 5. Rod reorientation at DMPE samples, tan ($\varphi/2$), vs. time, for surface pressures just below

(circles, 29 mN/m) and above (squares, 34 mN/m) the LC-S phase transition at 32 mN/m (kink in

isotherm, Fig. 1). At 29 mN/m, the nanorod reorients completely, ending at tan ($\varphi/2$) = 0, and the

rate is consistent with a purely viscous response described by Eqn. 3. At 34 mN/m, above the LC-

S transition surface pressure, the rod "stalls" at tan ($\varphi/2$) > 0, indicating the appearance of an

elastic component, which causes the nanorod to stop rotating at a finite angle.
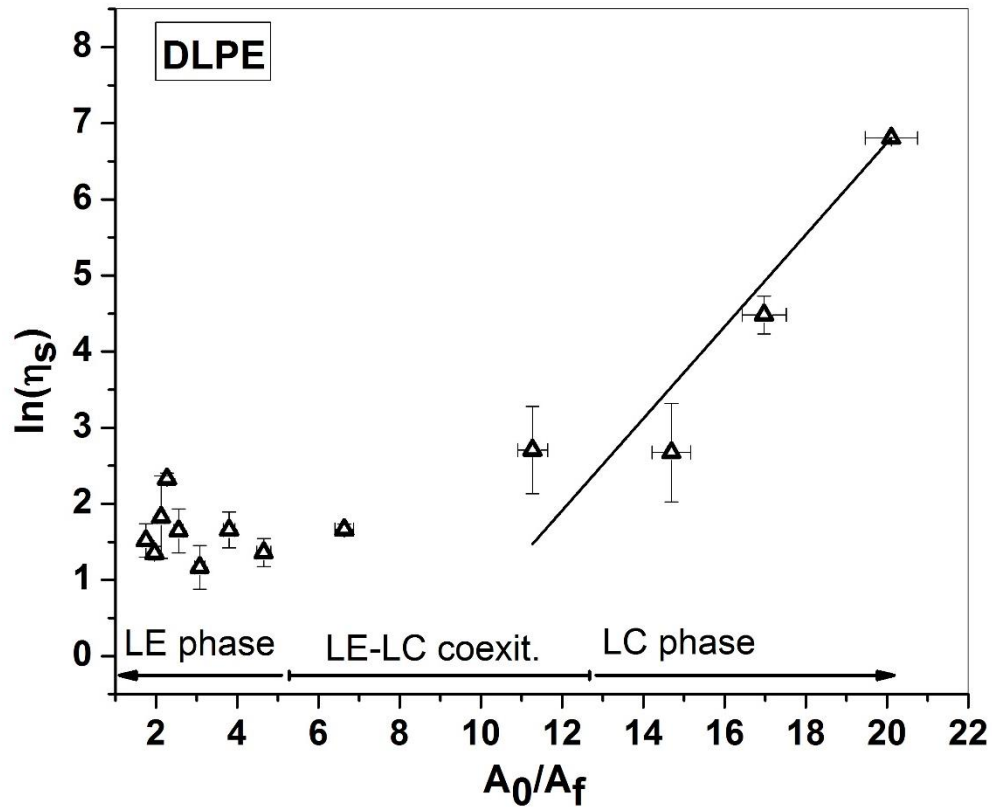
Figure 6a. Natural logarithm of surface viscosity vs. the ratio of the close-packed A_0 to free area A_f for DLPE monolayer. The correlation between surface viscosity and free-area model has been used to represent the phase transition. At $\pi < \pi_c$ the change in surface viscosity is not significant and does not satisfy the free area model. In the LC phase, the change in the surface viscosity with molecular area can be explained by the free area model ($p < 0.05$ for the fit).

Figure 6b. Natural logarithm of surface viscosity vs. the ratio of the close-packed A_0 to free area A_f for DMPE monolayer. In the LC phase, the exponential increase in surface viscosity follows the two-dimensional free-area model ($p<0.1$).

2.6.   References

1.   Jamieson, G.A. and D.M. Robinson, *Mammalian Cell Membranes*. Vol. 2. 1977, London: Butterworth.
2.   Epand, R.F., P.B. Savage, and R.M. Epand, *Bacterial lipid composition and the antimicrobial efficacy of cationic steroid compounds*. Biochemica et Biophysica Acta, 2007. **1768**: p. 2500-2509.
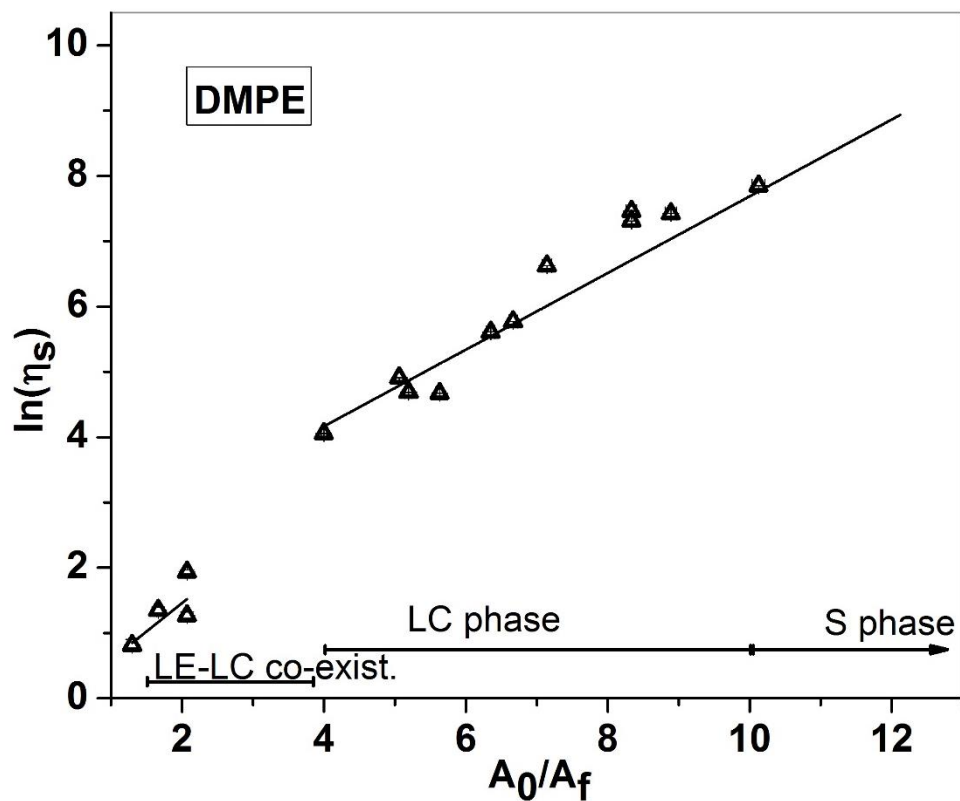3.   Albrecht, O., H. Gruler, and E. Sackmann, *Polymorphism of Phospholipid Monolayers*. Journal De Physique, 1978. **39**(3): p. 301-313.
4.   Kaganer, V.M., H. Mohwald, and P. Dutta, *Structure and phase transitions in Langmuir monolayers*. Reviews of Modern Physics, 1999. **71**(3): p. 779-819.
5.   Helm, C.A., et al., *Phases Of Phosphatidyl Ethanolamine Monolayers Studied by Synchrotron X-Ray Scattering*. Biophysical Journal, 1991. **60**(6): p. 1457-1476.
6.   Kjaer, K., et al., *ORDERING IN LIPID MONOLAYERS STUDIED BY SYNCHROTRON X-RAY-DIFFRACTION AND FLUORESCENCE MICROSCOPY*. Physical Review Letters, 1987. **58**(21): p. 2224-2227.
7.   Boyd, E. and W.D. Harkins, *Molecular interaction in monolayers: Viscosity of two-dimensional liquids and plastic solids. V. Long chain fatty acids*. Journal of the American Chemical Society, 1939. **61**: p. 1188-1195.
8.   Alonso, C. and J.A. Zasadzinski, *A brief review of the relationships between monolayer viscosity, phase behavior, surface pressure, and temperature using a simple monolayer viscometer*. Journal of Physical Chemistry B, 2006. **110**(44): p. 22185-22191.
9.   Gavranovic, G.T., et al., *Interfacial rheology and structure of straight-chain and branched hexadecanol mixtures*. Industrial & Engineering Chemistry Research, 2006. **45**(21): p. 6880-6884.
10.   Kurtz, R.E., et al., *Langmuir Monolayers of Straight-Chain and Branched Hexadecanol and Eicosanol Mixtures*. Langmuir, 2008. **24**(24): p. 14005-14014.
11.   Birdi, K.S., *Lipid and biopolymer monolayers at liquid interfaces*. 1989, New York: Plenum Press.
12.   Saffman, P.G. and M. Delbruck, *Brownian motion in biological membranes*. Proc. Nat. Acad. Sci. USA, 1975. **72**: p. 311-313.
13.   Prasad, V., S.A. Koehler, and E.R. Weeks, *Two-Particle Microrheology of Quasi-2D Viscous Systems*. Phys. Rev. Lett., 2006. **97**: p. 176001-4.
14.   Choi, S.Q., et al., *Influence of Molecular Coherence on Surface Viscosity*. Langmuir, 2014. **30**: p. 8829-8838.
15.   Choi, S.Y., et al., *Active microrheology of phospholipid monolayers: seeing stretching, flowing, yielding and healing*. Nature Communications, 2011. **2**: p. 312.
16.   Kim, K., et al., *The effect of cholesterol nanodomains on monolayer morphology and dynamics*. Proc. Nat. Acad. Sci. USA, 2013. **101**(33): p. E3054-E3061.
17.   Kim, K., et al., *Interfacial microrheology of DPPC monolayers at the air-water interface*. Soft Matter 2011. **7**: p. 7782-7789.
18.   Ding, J.Q., et al., *Magnetic needle viscometer for Langmuir monolayers*. Langmuir, 2002. **18**(7): p. 2800-2806.
19.   Brooks, C.F., et al., *An interfacial stress rheometer to study rheological transitions in monolayers at the air-water interface*. Langmuir, 1999. **15**(7): p. 2450-2459.
20.   Bantchev, G.B. and D.K. Schwartz, *Surface shear rheology of beta-casein layers at the air/solution interface: Formation of a two-dimensional physical gel*. Langmuir, 2003. **19**(7): p. 2673-2682.
21.   Reynaert, S., et al., *Analysis of the magnetic rod interfacial stress rheometer*. Journal of Rheology, 2008. **52**(1): p. 261-285.

22. Klingler, J.F. and H.M. McConnell, *BROWNIAN-MOTION AND FLUID-MECHANICS OF LIPID MONOLAYER DOMAINS.* Journal of Physical Chemistry, 1993. **97**(22): p. 6096-6100.

23. Schwartz, D.K., C.M. Knobler, and R. Bruinsma, *DIRECT OBSERVATION OF LANGMUIR MONOLAYER FLOW-THROUGH A CHANNEL.* Physical Review Letters, 1994. **73**(21): p. 2841-2844.

24. Sickert, M., F. Rondelez, and H.A. Stone, *Single-particle Brownian dynamics for characterizing the rheology of fluid Langmuir monolayers.* Epl, 2007. **79**(6).

25. Wilson, L.G. and W.C.K. Poon, *Small-world rheology: an introduction to probe-based active microrheology.* Physical Chemistry Chemical Physics, 2011. **13**(22): p. 10617-10630.

26. Dhar, P., et al., *Active Interfacial Shear Microrheology of Aging Protein Films.* Physical Review Letters, 2010. **104**(1): p. -.

27. Lee, M.H., et al., *Combined passive and active microrheology study of protein-layerformation at an air-water interface.* Langmuir, 2010. **26**(4): p. 2650-2658.

28. Prasad, V., S.A. Koehler, and E.R. Weeks, *Two-particle microrheology of quasi-2D viscous systems.* Physical Review Letters, 2006. **97**(17).

29. Dhar, P., et al., *Autonomously moving nanorods at a viscous interface.* Nano Letters, 2006. **6**: p. 66-72.

30. Shlomovitz, R., et al., *Measurement of monolayer viscosity using noncontact microrheology.* Physical Review Letters, 2013. **110**(13): p. 137802.

31. Allan, D.B., et al., *Linear and nonlinear microrheology of lysozyme layers forming at the air-water interface.* Soft Matter, 2014. **10**(36): p. 7051-7060.

32. Fischer, T.M., P. Dhar, and P. Heinig, *The viscous drag of spheres and filaments moving in membranes or monolayers.* Journal of Fluid Mechanics, 2006. **558**: p. 451-475.

33. Helm, C.A. and H. Mohwald, *Equilibrium and Nonequilibrium Features Determining Superlattices in Phospholipid Monolayers.* Journal of Physical Chemistry, 1988. **92**(5): p. 1262-1266.

34. Maltseva, E. and G. Brezesinski, *Adsorption of amyloid beta (1-40) peptide to phosphatidylethanolamine monolayers.* Chemphyschem, 2004. **5**(8): p. 1185-90.

35. Paxton, W.F., et al., *Catalytic Nanomotors: Autonomous Movement of Striped Nanorods.* J. Am. Chem. Soc., 2004. **126**: p. 13424-13431.

36. Dhar, P., et al., *Autonomously moving local nanoprobes in heterogeneous magnetic fields.* Journal of Physical Chemistry C, 2007. **111**(9): p. 3607-3613.

37. Dhar, P., et al., *Active interfacial shear microrheology of aging protein films.* Physical Review Letters, 2010. **104**(1): p. 016001.

38. Kim, K., et al., *Interfacial microrheology of DPPC monolayers at the air-water interface.* Soft Matter, 2011. **7782-7789**: p. 7782-7789.

39. Choi, S.Q., et al., *Active microrheology and simultaneous visualization of sheared phospholipid monolayers.* Nat Commun, 2011. **2**: p. 312.

40. McConnell, H.M., *Structures and Transitions in Lipid Monolayers at the Air-Water-Interface.* Annual Review of Physical Chemistry, 1991. **42**: p. 171-195.

41. Israelachvili, J., *Self-assemblyin two dimensions: surface micelles and domain formation in monolayers.* Langmuir, 1994. **10**: p. 3774-3781.

42. Losche, M., E. Sackmann, and H. Mohwald, *A fluorescence microscopic study concerning the phase diagram of phospholipids* Berichte Der Bunsen-Gesellschaft-Physical Chemistry Chemical Physics, 1983. **87**(10): p. 848-852.

43. Knobler, C.M., *Seeing phenomena in flatland: studies of monolayers by fluorescence microscopy.* Science, 1990. **249**(4971): p. 870-4.

44. Losche, M. and H. Mohwald, *FLUORESCENCE MICROSCOPE TO OBSERVE DYNAMICAL PROCESSES IN MONOMOLECULAR LAYERS AT THE AIR WATER INTERFACE.* Review of Scientific Instruments, 1984. **55**(12): p. 1968-1972.

45.   Losche, M., E. Sackmann, and H. Mohwald, *A FLUORESCENCE MICROSCOPIC STUDY CONCERNING THE PHASE-DIAGRAM OF PHOSPHOLIPIDS.* Berichte Der Bunsen-Gesellschaft-Physical Chemistry Chemical Physics, 1983. **87**(10): p. 848-852.
46.   Hermans, E. and J. Vermant, *Interfacial shear rheology of DPPC under physiologically relevant conditions.* Soft Matter, 2014. **10**(1): p. 175-86.
47.   Kragel, J., et al., *Surface rheology of monolayers.* Thin Solid Films, 1996. **284**: p. 361-364.
48.   Choi, S.Q., et al., *Influence of molecular coherence on surface viscosity.* Langmuir, 2014. **30**(29): p. 8829-38.
49.   Kim, K., et al., *Interfacial microrheology of DPPC monolayers at the air-water interface.* Soft Matter, 2011. **In press**.
50.   Lee, K.Y.C., et al., *Influence of palmitic acid and hexadecanol on the phase transition temperature and molecular packing of dipalmitoylphosphatidylcholine monolayers at the air-water interface.* Journal of Chemical Physics, 2002. **116**(2): p. 774-783.
51.   Alonso, C. and J.A. Zasadzinski, *Linear dependence of surface drag on surface viscosity.* Phys. Rev. E, 2004. **69**: p. 0216021-6.
52.   Galla, H.J., et al., *On two-dimensional passive random walk in lipid bilayers and fluid pathways in biomembranes.* J Membr Biol, 1979. **48**(3): p. 215-36.
53.   Kim, K., et al., *Effect of cholesterol nanodomains on monolayer morphology and dynamics.* Proc Natl Acad Sci U S A, 2013. **110**(33): p. E3054-60.
54.   Cohen, M.H. and D. Turnbull, *Molecular Transport in Liquids and Glasses.* Journal of Chemical Physics, 1959. **31**(5): p. 1164-1169.

Chapter 3: pH induced changes in the surface viscosity of unsaturated phospholipids depends on the lipid head-group charge

3.1. Introduction

Lipid membranes form an integral part of all living things. In addition to serving as a barrier between the extracellular and intercellular environment, as well as between the intracellular organelles, cell membranes control many essential processes such as cellular signaling and transportation [1, 2]. Since phospholipids are the fundamental building blocks of these lipid membranes, their interactions with molecules in the surrounding environment have a significant impact on overall cellular functions, by altering the structure, lateral organization, and dynamics of membranes [1-3]. These molecular interactions are also expected to be influenced by changes in the intracellular and extracellular environmental pH [1, 2, 4]. While the interior pH in the extracellular environment is maintained at 7.4, the intracellular vesicles in the endocyclic pathway can undergo vast pH changes [1, 2, 5]. For example, the pH of vesicles in early endosomes is 7.0 and it reduces to pH 4.5-5.0 in late endosomes and lysosomes [1, 2, 5-7].

One particular effect of changes in the intracellular pH on phospholipid membranes that remains unexplored is the effect of changes in intracellular pH on membrane fluidity. Membrane fluidity plays a crucial part in several cellular processes[8, 9], and is modulated by changes in membrane packing and orientation. Extensive studies using deuterium NMR on phosphatidylcholine (PC) head-groups have established the ability of lipid head-groups to reorient themselves in response to the presence of charges in their vicinity, thus serving as a powerful sensor of electrostatic interactions between lipid molecules (often referred to as the "electrometer effect") [10-13]. However, how reorientation of the phospholipid head-group effects the fluidity of phospholipid membranes is currently not available. The presence of chemically different phospholipid head-group moieties in different cellular compartments introduces complexities when exploring the effect of head-group reorientation on membrane fluidity.   While   the

59

outer leaflet of eukaryotic cell membranes contain only zwitterionic lipid head groups, such as phosphatidylcholine (PC) and phosphoethanolamine (PE), the location of anionic phospholipids such as phosphotidylserine (PS) in the inner leaflet of the plasma membrane ensures passive transport through the cell membrane by maintaining an electrostatic gradient [1, 2]. Further, late endosomes and lysosomes have a higher composition of negatively charged phospholipids such as Bis Monoacylglycero Phosphate (BMP), which is a structural isomer of phosphotidylglycerol (PG)[1, 2, 6]. Therefore, in order to obtain a complete understanding of the effect of pH changes in the cellular environment on lipid head-group re-orientations, the role of lipid head-group chemistry also needs to be considered, making this a major focus of this paper.

Measuring the fluidity or surface viscosity of phospholipid membranes is non-trivial. This is especially true for unsaturated phospholipids that are the most abundant type of phospholipids in the cell membranes [2]. This difficulty stems from the inability to realize a completely isolated two-dimensional surface that is decoupled from the bulk sub-phase, as first identified by Saffmann and Dulbruck for lipid membranes[14]. Detailed analysis of probe motion in lipid-laden interfaces suggest that this decoupling, quantified by the Boussinesq number B, should be much greater than one (B>>1)[15] [14]. Such analysis suggests that most current rheometers are capable of accurately measuring surface viscosities as low as 10^{-6} Ns/m [16]. However, surface viscosity of unsaturated phospholipids, which mostly remain in the liquid expanded phase, remain inaccessible to macroscopic rheometers, making measurements of their surface viscosity especially challenging. Recent development of passive and active microrheology techniques, incorporating micron and sub-micron sized probes increase the sensitivity of the measurements to viscosities as low as 10- (N-s/m), making the studies described here possible.

In this work, a previously described active microrheology technique[17], that analyzes the induced motion of nickel nanorods placed in a lipid monolayer, is used to monitor surface viscosity of four different unsaturated phospholipids at pH of 7.4 and 4.4 , representing the limits in the pH encountered by phospholipid membranes in all cells, from the plasma membranes to late endosomes. Our choice of lipid head-groups is representative of the varying composition of the cellular membranes. Phosphatidylcholine (PC) head-group represents the most abundant zwitterionic phospholipid in the cell membrane. Phosphoethanolamine (PE), also a zwitterionic lipid typically present in the inner leaflet of plasma membrane, is used here to compare the effect of the size of the head-group in the head-group reorientation process. PS and PG are used a representative anionic lipids, and PG is also used to model the composition of late endosomes (see table 1). To limit our attention only on lipid head-group reorganization, and rule out any influence from lipid chain length, the same mixed lipid alkyl chains (1-palmitoyl-2-oleoyl) are chosen in all four samples.

3.2.   Materials and Methods

1-hexadecanoyl-2-(9Z-octadecenoyl)-sn-glycero-3 phosphocholine (sodium salt) (POPC), 1-hexadecanoyl-2-(9Z-octadecenoyl)-sn-glycero-3-phosphoethanolamine(POPE), 1-palmitoyl-2-oleoyl-sn-glycero-3-phospho-L-serine (sodium salt) (POPS), and 1-palmitoyl-2-oleoyl-sn-glycero-3-phospho-(1'-rac-glycerol) (sodium salt) (POPG) were purchased from Avanti Polar Lipids, Alabaster, AL, as organic mixtures in chloroform. Texas Red® 1,2-dihexadecanoyl-*sn*-glycero-3-phosphoethanolamine, triethylammonium salt, (TXR-DHPE) was purchased in the dried form from Life Technologies (Invitrogen) and dissolved in HPLC grade chloroform. The lipids were stored at -20 °C when not in use. Salts sodium hydrogen phosphate (Na_2HPO_4), sodium dihydrogen phosphate (NaH_2PO_4), sodium chloride (NaCl), and potassium chloride (KCl) and   calcium chloride dihydrate (CaCl2. $2H_2O$) were purchased from Fisher Scientific. All organic solvents used in this work were also purchased from Fisher Scientific. Phosphate

Buffered Saline (PBS) at pH 4.4 and 7.4 with ionic strength of 185.56 mM was used for all experiments was prepared using stoichiometric amounts of sodium hydrogen phosphate (Na_2HPO_4), sodium dihydrogen phosphate (NaH_2PO_4), sodium chloride (NaCl), and potassium chloride (KCl) in water (resistivity 18.2 MΩ/cm) using a Millipore Gradient System (Billerica, MA).

A custom designed Langmuir trough, containing specially designed holders for electromagnetic coils, the purpose of which is explained below, was mounted on a standard Langmuir trough frame available from KSV-NIMA, Biolin Scientific[17]. Two delrin barriers were used to alter the total surface area, by using a stepper-motor that is part of the frame. This whole set-up was mounted on a custom-modified fluorescence microscope from Nikon (Eclipse LV100) . Surface pressure vs. area isotherms of phospholipids were recorded during the compression expansion isotherm by using a filter-paper Wilhelmy plate coupled to the Langmuir trough (KSV-NIMA, Biolin Scientific). The rate of compression used for the compression-expansion studies, was 125mm/min To initiate the surface pressure vs. area isotherm measurements in different sub-phase pHs, a 1 mg/ml organic solution of phospholipids (POPC, POPE, POPS, and POPG) in chloroform with 1 wt% of added TXR-DHPE dye molecules was first added drop-wise at several locations on the buffer-air interface and the chloroform was allowed to evaporate for 20 minutes before compression was started. The change in the surface pressure with change in the mean molecular area was recorded using KSV-NIMA's interface unit and accompanying software and saved for later analysis.

Surface viscosity of the monolayer films was obtained by a previously described active microrheology technique [17]. Briefly, four home-built electromagnetic coils, oriented perpendicular to each other and placed in the magnet holder of the modified Langmuir trough, were used to apply an external magnetic field (3 G – 100 G), which was used to orient nickel rods of size diameter 300 nm and length 10-30 µm, placed on the lipid laden interface. The nickel nanorods were synthesized by electrochemical deposition of nickel into alumina templates [8-10], washed thoroughly by several centrifuging steps, re-suspended in a isopropanol:water mixtures and added dropwise to the phospholipid covered interface. The

capillary forces at the interface retain the nanorods at the interface, allowing the monitoring of the reorientation of individual nanorods. After addition of the nanorods to the monolayer surface, the monolayer was compressed to surface pressures 20 mN/m, 25 mN/m, and 30 mN/m using the barriers of the Langmuir trough, and images of the nanorod reorientation was recorded and saved for further analysis. To visualize the motion of individual nanorods, an extra-long working distance and a motorized stage was used to reduce the disturbances to the interface. The circular chamber between the electromagnets helped with controlling the drift of the interface, while the channels allowed free flow of the lipids in and out of the contained area, as shown in the supplementary data (Figure S1A). The drift was further controlled by using a custom designed microscope cover with a built in window to monitor the position of the objective with respect to the air-water interface.

3.3. Theoretical analysis

Analysis of nanorod motion:

The equations describing the reorientation of magnetic nanorods (length *l*, magnetic moment $\mu_o m$) under an externally applied magnetic field have been described in detail in previous publications [17-20]. Briefly, the motion of these magnetic rheological probes in a purely viscous monolayer may be described by Eqn. 4,

$$\mu_0 mH sin\varphi = -f_r \eta_w l^3 \frac{d\varphi}{dt} \quad (4)$$

where H is typically the externally applied magnetic field and φ the angle between the length of rod and the applied magnetic field direction. The assumption of a purely viscous system is valid for the unsaturated phospholipid films studied here, since unsaturation in the alkyl chains prevent these phospholipid molecules from assembling into well-organized liquid condensed or solid phases. We have recently shown that a transition from a LE or LC condensed to a solid phase in a

saturated phospholipid film is often accompanied by a significant increase in surface elasticity[17].

However, this is not accepted to be the case for the monounsaturated films being studied here, and

indeed the magnetic rods were found to align completely with the applied magnetic field, H (

$j \rightarrow 0$). Thus in a purely viscous system the movement of the nanorod is only resisted by the

viscous drag in the system. The reorientation of the nanorod was measured by the ImageJ tracking

software, and the rod motion plotted as a function of time. The rod reorientation is described by

the following equation:

$$\tan(\varphi/2) = \exp\left(-\frac{t}{\tau}\right) \quad (5)$$

where the relaxation time, $\tau = \frac{f_r \eta_w l^3}{\mu_0 mH}$, is obtained by fitting the $\tan(\varphi/2)$ values of rod reorientation

data to equation 4 using the origin 8.6 software. The magnetic moment of the rod can be written

in terms of the magnetization, M, and the rod aspect ratio, l/r. Therefore, the relaxation time, τ as:

$$\tau = \frac{f_r \eta_w l^3}{\mu_0 mH} = \frac{f_r \eta_w l^3}{\mu_0 MVH} = \frac{f_r \eta_w l^3}{\mu_0 M\pi r^2 lH} = \frac{f_r \eta_w}{\mu_0 M\pi H}\left(\frac{l}{r}\right)^2 \quad (6)$$

By substituting the average magnetization of the rod (11.9 C/s.m) obtained as a result of

calibrations in water and glycerol [21], the dimensionless drag coefficient of the rod, $f_r = f_w + f_s$

was obtained and f_s was calculated by subtracting f_w from f_r.

The subphase drag, f_w, was taken to be equal to half that of the drag on a rod of radius r and length

l (for $l/r \geq 20$) rotating in a viscous fluid: $f_w = \frac{\pi}{6[\ln(\frac{l}{r}-0.8)]}$ [21-23]. For each value of τ the

relationship between the Boussinesq number, B, and f_s for an incompressible interfacial film was

determined by using the analytical relationship described by Dhar et. al.,. [21]. These values of f_s were then used to calculate the surface viscosity.

Calculation of the association parameters of the phospholipid films at the different pHs:

The thermodynamics behind these surface pressure-area isotherms could give more information about the intermolecular interactions of the molecules at the air-water interface. The Butler's equation provided the classic relationship between chemical potentials of the components within surface layer which depends on the composition of the layer and its surface tension [24]. Thermodynamic definition for multicomponent Langmuir monolayers based on Butler's equation and Gibbs equation of adsorption has been used by Volmer [25-27].

$$\Pi = -\frac{kT}{\omega_0}(\ln x_0 + \ln f_0) \quad (7)$$

Where k is Boltzmann constant and ω_0 is the molecular area per solvent molecule. Assuming the enthalpy contribution, $\ln f_0^H$ is independent of A and corresponds to a liquid-expanded monolayer, cohesion pressure, Π_{coh}, describes the interaction between the components.

$$\Pi_{coh} = \frac{kT}{\omega_0}\ln f_0^H \quad (8)$$

The increase in cohesion pressure could indicate an increased density of packing at the interface and an increased robustness of the monolayer [26, 28].

Vollhardt and Fainerman have derived a thermodynamic definition for multicomponent Langmuir monolayers based on Volmer's work and using Gibbs equation of adsorption called generalized Volmer's equation [25, 26].

$$\Pi = \frac{kT(\frac{\omega}{A})}{\omega_0(1-(\frac{\omega}{A}))} - \Pi_{coh} \quad (9)$$

Where Π is the surface pressure, ω_0 is the molecular area per solvent molecule, ω is the average molecular area of insoluble species, k is the Boltzmann constant and T is the temperature [27, 29]. By fitting equation 9 to the experimentally obtained isotherms the association degree, defined as $n = \frac{\omega}{\omega_o}$, and the cohesion pressure between phospholipid molecules, Π_{coh}, were obtained. The Volmer's generalized equation has been used to quantify the packing density and compare the interaction between molecules in response to change of pH[29].

3.4. Results and Discussion

POPC

First we measured the interfacial properties of POPC, the most abundant unsaturated phospholipid in the cell. Figure 1A presents the average value of the total drag force for POPC at surface pressure 20, 25, and 30 mN/m at both pH 7.4 and pH 4.4. The interfacial drag can be measured by our setup and differentiated from bulk properties, since the total drag force was higher than the measured values of lipid-free control sample (indicated as a line at 0.14 on the graph). We observed an increase in the total drag force at pH 4.4 for POPC by increasing the surface pressure. Figure 1B illustrates the changes in surface viscosity of POPC translated from the total drag force based on affirmation theoretical section. Based upon total drag force measurements, the surface viscosity increased at pH 4.4 as compared to pH 7.4. Figure 1B shows a significant increase in average surface viscosity at pH 4.4 from ~15 nNs/m to ~28 nNs/m with corresponding surface pressures of 25 and 30 mN/m. However, increase in surface pressure did not have a significant effect on surface viscosity at pH 7.4 across all POPC samples.

To explore the lipid interactions of the molecules at the air-water interface by change of pH, surface energy, in terms of surface tension (surface pressure), have been measured. Figure 2A shows a representative surface pressure, Π, (γ=72 mN/m for water, γ is the measured surface tension) against molecular area isotherm of POPC at pH 7.4 and pH 4.4. As the area available to the POPC monolayer is reduced, Π increased from zero to a maximum surface pressure of ~45 mN/m. It is well known that unsaturated phospholipids remain in the liquid expanded phase with no specified crystalline order [1]. It is expected that the surface viscosity of POPC samples would be low, and the films be purely viscous; this was indeed the case for all POPC monolayers. To detect any possible change in the Langmuir monolayer fluorescence imaging of the samples were acquired at both pH 4.4 and pH 7.4 (Supplementary figure S2 A,B) which confirmed a lack of crystalline order.

Next, we fitted the isotherm of the POPC monolayer to the Volmer's generalized equation at both neutral and acidic pH values tested (Figure 2B). The average molecular area of insoluble species (ω) decreased at pH 4.4 compared to pH 7.4 suggesting a higher packing density. The ratio of molecular area occupied by lipids to water, n, at pH 4.4 was greater than the value at pH 7.4. The cohesion pressure, Π_{coh}, also increased at pH 4.4 compared to 7.4, since the ω_0 (the molecular area per solvent molecule) has been reduced. The thermodynamic properties presented in panel B of figure 2 indicate a greater interaction between the insoluble molecules at the Langmuir monolayer with a decrease in pH. Gurtovenko, *et. al.,* have previously shown that by inducing the electric field at the lipid (PC/PE) bilayer, the lateral pressure and the density of packing have changed relative to the location of the electric field [30]. Herein, we have also observed similar changes in the cohesion pressure through pH-induced charges.

Studies have shown that the presence of foreign charges at the air-water interface influences the intralipid interactions of an electrically neutral phospholipid via head-group reorientation [31-33]. Previous NMR data confirmed the parallel alignment of the $P^-\_N^+$ dipoles to the interface with angle of 0-3° for an electrically neutral phospholipid head-group (PC)[13, 31-34]. Interestingly in the presence of foreign charges in the local micro-environment, the angle of $P^-\_N^+$ dipoles changes due to attraction/repulsion between exterior dipoles and partial charges [13, 31-34]. The angle and degree of reorientation of the head-group depend on the magnitude and type of the foreign charge (positive or negative)[13, 31-34]. A change in the angle of the head-moiety could impact the packing density of the molecules at the interface. Wang, *et. al.,* have also demonstrated a similar concept through exposing charged nanoparticles to the phospholipid bilayer[35]. In this study the local construction changes making the bilayer more gel-like or fluid-like depending on the charge of the particle, also using an isothermal titration calorimetry, a loss of entropy was observed while the gelation occurred[35]. Overall, these findings indicate that the head-group reorients to satisfy the strongest dipole-dipole or dipole-ion interactions (measured as loss of entropy)[34, 35]. We expect that what Wang *et. al.,* observed as a gel-like properties would result in less fluidity and a higher surface viscosity. In our study, at lower pH the larger concentration of available OH^- ions could have stronger interaction with positive charge of head-group; therefore, the $P^-\_N^+$ dipole could tilt toward the acidic solution.

We hypothesize that there should be a considerable change in intramolecular interactions between POPC molecules by reducing the pH to follow the significant increase of surface viscosity. As the schematic figure represents, in acidic conditions the intralipid interactions would increase to promote a higher packing density, providing the head-group contains an overall neutral dipole. The increase in packing density was detected through a decrease in average molecular area

of lipids (ω) based on Volmer's equation. This surface coverage could also be translated to the greater surface viscosity which we observed for POPC monolayer at pH 4.4. Furthermore, AFM imaging showed more distinct clusters were formed in these lower as compared to the transferred monolayer at pH 7.4 pH 4.4 at the air-water interface (Supplementary figure S3). These features confirm the increased intralipid interactions at acidic pH. These interactions could be stimulated by the presence of an ionic excess at acidic pH which could build a stronger network of interactions in vicinity of each lipid molecules and bridge the lipid-lipid binding.

POPE

To validate our hypothesis on the effect of acidic pH on zwitterionic head-groups, we continued our study on unsaturated phospholipids with POPE monolayer. Figure 4A represents the total drag force measured by reorientation of nanorods at pH 4.4 and 7.4. Translating the total drag force to surface viscosity, figure 4B represents changes in surface viscosity based upon both pH and surface pressure. Remarkably, in the absence of any crystalline order (Supplementary figure S2 E,F) a significant increase of surface viscosity was observed from ~17nNs/m at surface pressure 25 mN/m to ~65nNs/m at surface pressure 30mN/m at pH 4.4. However, similar to POPC, at pH 7.4 the surface viscosity remained almost constant with increasing surface pressure. Even with the substantial boost in surface viscosity for POPE at a surface pressure of 30 mN/m in acidic pH, we were unable to detect any elasticity. Nanorod rotations mirrored the exponential decay curve expected for a purely viscous fluid. The result of higher surface viscosity for the zwitterionic POPE samples at pH 4.4 confirmed what we observed with POPC samples and thus validates our hypothesis on increased interfacial packing for these moieties.

Figure 5A shows a representative surface pressure-area isotherm of POPE monolayer in both pH environments tested. The POPE monolayer collapse occurred at surface pressure ~47 mN/m. The isotherm of POPE at both pH 7.4 and pH 4.4 were fitted to the Volmer's generalized equation (Figure 5B). Similar to POPC, the average molecular area of insoluble species (ω) decreased at pH 4.4 compared to pH 7.4 suggesting higher packing density of the molecule. The ratio of molecular area occupied by lipid to water, n, increased at pH 4.4 compared to pH 7.4. Furthermore, Π_{coh} increased at acidic conditions, since the ω_0 (the molecular area per solvent molecule) decreased. Larger n and Π_{coh} values suggest higher interaction between POPE molecules at pH 4.4. This increase was greater for POPE as compared to POPC which was similar to what we observed for surface viscosity.

The similarity of POPE and POPC results further validates our hypothesis that there are significantly more interaction of the neutral dipole at acidic pH. At the highest surface pressure tested, with the minimum surface area available at the air-water interface, the packing density of lipid molecules were strongly influenced by the pH as shown through Volmer's parameters. This increased interaction at pH 4.4 could be due to stronger and plentiful hydrogen bonds between head-group dipoles and ions in the solution. Since the charge of PC and PE head-groups are similar, the size and chemistry of the head-group are the remaining parameters which could affect lipid-lipid interaction and packing densities. Both rheological data and thermodynamic parameters suggest stronger interactions between head-groups of POPE molecules compared to POPC at acidic pH. Gurtovenko, *et. al.,* also reported that following electric field application the PE head-group travels in the bilayer less than that observed for the PC suggesting a stronger bonding between PE lipids [30]. Similarly, in our study, the increase of cohesion pressure in POPE was larger than POPC.

70

POPG

We studied POPG monolayer to detect the influence of charge of head-group on surface fluidity, since the PG moiety hold a total negative charge of -1.0 through the pH range of 7.4-4.4 with. Interestingly our data showed that the total drag of POPG monolayer remained unchanged during an increase in surface pressure at both pH 7.4 and 4.4 (Figure 6A). Therefore the POPG monolayer did not have any measurable surface viscosity in all surface pressures at both tested pH values (Figure 6B). This result indicates that the presence of negative charge of the head-group impacts the fluidity of phospholipid monolayer compared to zwitterionic ones. Interestingly, AFM images showed less distinct clusters at pH 4.4 for a transferred monolayer of POPG compared to what was observed for POPC monolayer before (Supplementary Figure S3).

Subsequently the surface pressure-area isotherm of POPG monolayer were measured at both neutral and acidic pH (Figure 7A). The maximum surface pressure occurred at ~45 mN/m. Isotherms of POPG were found to be shifted by less than 5 A^{02}/molecule to a higher mean molecular area for pH 4.4 compared to the pH 7.4 suggesting that the packing is less condensed at pH 4.4. Interestingly by fitting the POPG isotherms to generalized Volmer's equation (Figure 7B) the n, and Π_{coh} were decreased at pH 4.4 compared to pH 7.4. The Π_{coh} of POPG in both pH 4.4 and 7.4 is lower than the values obtained for the zwitterionic lipids which could indicate lesser interaction between POPG molecules compared to previous samples. Similarly the decrease of n predicts less significant interaction between POPG molecules at pH 4.4. We hypothesize the strong negative charge could cause a repulsion between head-groups at air-water interface limiting the packing density of POPG molecules since PG head-group is protonated through the pH range of 7.4 to 4.4.

POPS

We continued our investigation on the effect of the head-group charge on interfacial packing of unsaturated phospholipids with POPS monolayer that has partly zwitterionic properties. While POPS is anionic with a total negative charge of -1.0 at pH 7.4, at pH 4.4 the carboxyl moiety of POPS is protonated only less than 10% which gives a total charge of -0.125 to the head-group. Therefore at pH 7.4 POPS is almost zwitterionic similar to the PC and PE head-groups (see table 1 for the pKa of POPS). Figure 8A and 8B present the total friction coefficient and the surface viscosity of POPS at pH 7.4 and 4.4. Surface viscosity of POPS monolayer stayed very low at pH 7.4 at all tested surface pressures similar to what was observed for POPC and POPE monolayers. Interestingly at pH 4.4 there was an increase in surface viscosity by increase in surface pressure. The surface viscosity of POPS monolayer increases from ~7nNs/m at 25 mN/m to ~17nNs/m at 30 mN/m at pH 4.4. Even though the surface viscosity at 30mN/m was significantly higher for pH 4.4 compared to pH 7.4, it increased less than what was measured for POPC and POPE. We hypothesize that the existence of partial negative charge on POPS causes a minor repulsion between head-group moieties in very close proximity of molecules; therefore, the density of interfacial packing of POPS would not increase as much as zwitterionic lipids.

Figure 9A shows a representative surface pressure-area isotherm of POPS monolayer, at pH 7.4 and pH 4.4. As the area available to POPS monolayer was reduced, Π increased from zero, until a maximum surface pressure of ~49 mN/m was reached. The isotherm at pH 4.4 was shifted slightly to lower mean molecular area compared to pH 7.4, similar to POPC isotherms. Figure 9B presents the Volmer's generalized parameters. The average molecular area of POPS molecules decreased at the pH 4.4 compared to pH 7.4. Additionally similar to POPC and POPE the ratio of association and cohesion pressure increased at pH 4.4 compared to pH 7.4. These thermodynamic

parameters confirmed the increased association between the POPS molecules at the air-water interface at acidic pH.

Comparing these four types of unsaturated phospholipids, the head-group charge and size significantly alters the surface viscosity. The difference in surface viscosity of these unsaturated phospholipids especially becomes significant at surface pressure 30mN/m at pH 4.4 (Figure 10). Increase in surface viscosity, 4 times the minimum measured value for POPC (PO_4^- $\_CH_2\_CH_2\_N(CH_3)_3^+$) and 12 times for POPE ($PO_4^-\_CH_2\_CH_2\_NH_3^+$), could speak of the similar phenomena among these zwitterionic phospholipids. These data suggests that the difference between POPC and POPE fluidity at acidic pH is influenced by the size of the head moiety since the bulky head-group of POPC requires more space compared to POPE.

Additionally, The $P^-\_N^+$ dipole of POPS head-group acted similar to what was explained for POPC, and POPE in response to acidic pH, only with smaller increase in packing due to the minor repulsion as a result of the small negative charge. Furthermore, there was a difference in packing of POPS ($PO_4^-\_CH_2\_CH\_$ $NH_3^+\_COO^-$ head-group) compared to POPG (PO_4^- $\_CH_2\_CH\_OH\_CH\_OH$ head-group) at acidic buffers. This difference highlighted the effect of charge of the head-group moiety since PS head-group contains only a total negative charge of -0.125 compared to PG head-group with a total negative charge of -1.0.

3.5. Conclusions

We measured the surface viscosity of four unsaturated phospholipid monolayers, at both neutral and acidic pH and three surface pressures, to quantify the fluidity of a one component monolayer. Both zwitterionic (POPC, and POPE) and anionic (POPS, and POPG) lipids which contain no crystalline order at the air-water interface at ambient temperature. Overall the surface

viscosity were very low compared to previously measured values for saturated lipid monolayers at similar surface pressures and available area [17]. Relative to the minimum surface viscosity values measured, there was a significant increase of surface viscosity at pH 4.4 for POPC, POPE, and POPS by increasing the surface pressure but none for POPG samples. Furthermore the extracted thermodynamic parameters using Volmer's generalized equation confirmed the increased association between molecules for corresponding samples. The density of packing of phospholipid molecules increased for POPC, POPE, and POPS in available interfacial area. On the other hand the packing density of POPG monolayer did not increase by increase of surface pressure possibly due to the repulsion of negatively charged PG head-groups. NMR studies have reported the reorientation of the $P^-\_N^+$ dipole of phospholipid head-group in response to surrounding foreign charges [13, 31-34]. Since the unsaturated phospholipid monolayers do not have a significant crystallinity even at higher surface pressures, no X-ray data is available of their orientation [1, 36]. However, the significant increase of surface viscosity of zwitterionic head-groups at acidic pH, indicates a possible two dimensional semi-crystalline ordering at higher surface pressures. This increase of surface viscosity could indicate head-group reorientation which could result in increased packing density as we measured. The increased surface viscosity and packing density at acidic pH for zwitterionic unsaturated lipids has not been reported before due to the limitations of macroscopic rheometers.

3.6. Table and figures

Name	Synonyms	Classification	pKa	Structure
POPC	1-hexadecanoyl-2-(9Z-octadecenoyl)-sn-glycero-3 phosphocholine	Zwitterionic Phospholipid	pKa ~ 1.0	
POPE	1-hexadecanoyl-2-(9Z-octadecenoyl)-sn-glycero-3-phosphoethanolamine	Zwitterionic Phospholipid	pKa ~ 1.7 pKa ~ 11.25	
POPS	1-palmitoyl-2-oleoyl-sn-glycero-3-phospho-L-serine (sodium salt)	Anionic Phospholipid	pKa ~ 2.6 pKa ~ 5.5 pKa ~ 11.55	
POPG	1-hexadecanoyl-2-(9Z-octadecenoyl)-sn-glycero-3-phospho-(1'-rac-glycerol)	Anionic Phospholipid	pKa ~ 3.5	

Table 1. Name, synonyms, classification, pKa, and structure of the POPC, POPE, POPS and POPG monolayers which are characterized in this study.
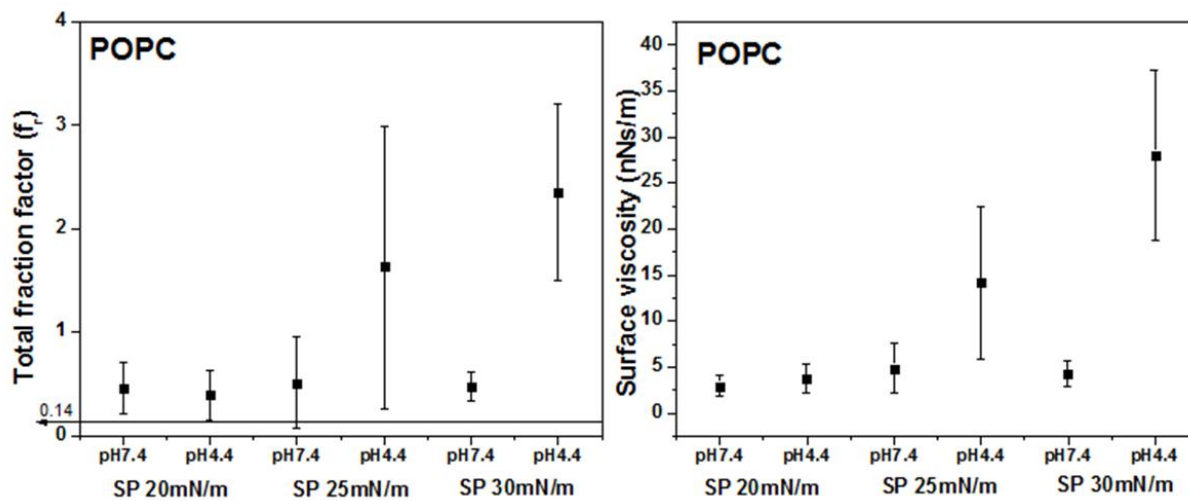
Figure 1 represent Changes in total friction drag and surface viscosity as a function of pH (4.4 and 7.4) and surface pressure (20, 25, and 30 mN/m) of **POPC**. Results are presented as mean and ±1.5SE (n >= 3). The "0.14 line" represents the value of total friction of half immersed rod (0.14) in water as control. At SP 30mN/m POPC has a significant increase in surface viscosity compared to pH 7.4 (p<0.01, one-way ANOVA).
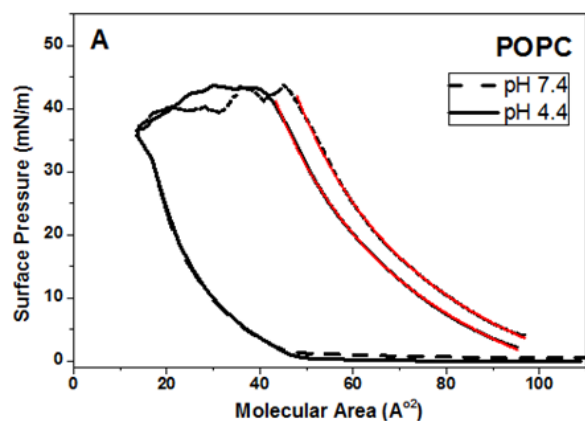
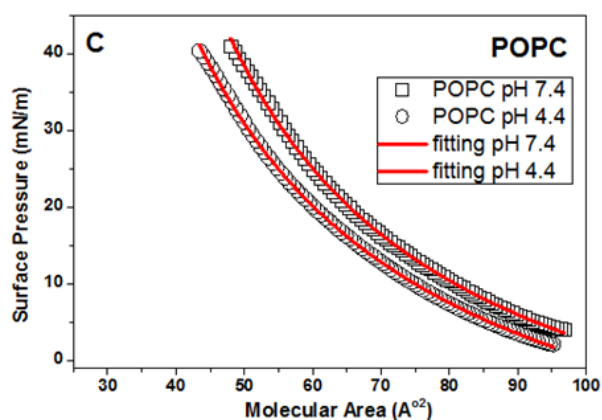| Parameters	POPC pH7.4	POPC pH4.4
$\omega\ (A^{o2})$	15.21	7.15
$\omega_0\ (A^{o2})$	2.91	1.19
$\Pi_{coh}\ (\dfrac{mN}{m})$	22.35	25.8
$n = \dfrac{\omega}{\omega_0}$	5.24	6.01

Figure 2A. Surface pressure vs area isotherm of **POPC** monolayer at pH 7.4 (solid curve) and pH 4.4 (dashed curve) lines (presented as average, N=3). **The red line** represents the fitting curve based on generalized Volmer's equation for insoluble monolayers to POPC isotherms at both pH 4.4 and 7.4. **Panel 2B** w = Average molecular area of amphiphilic species at the interface. w/ w_0 = n (accounts for associations between the amphiphilic molecules). π_{coh} = Cohesion pressure between molecules.
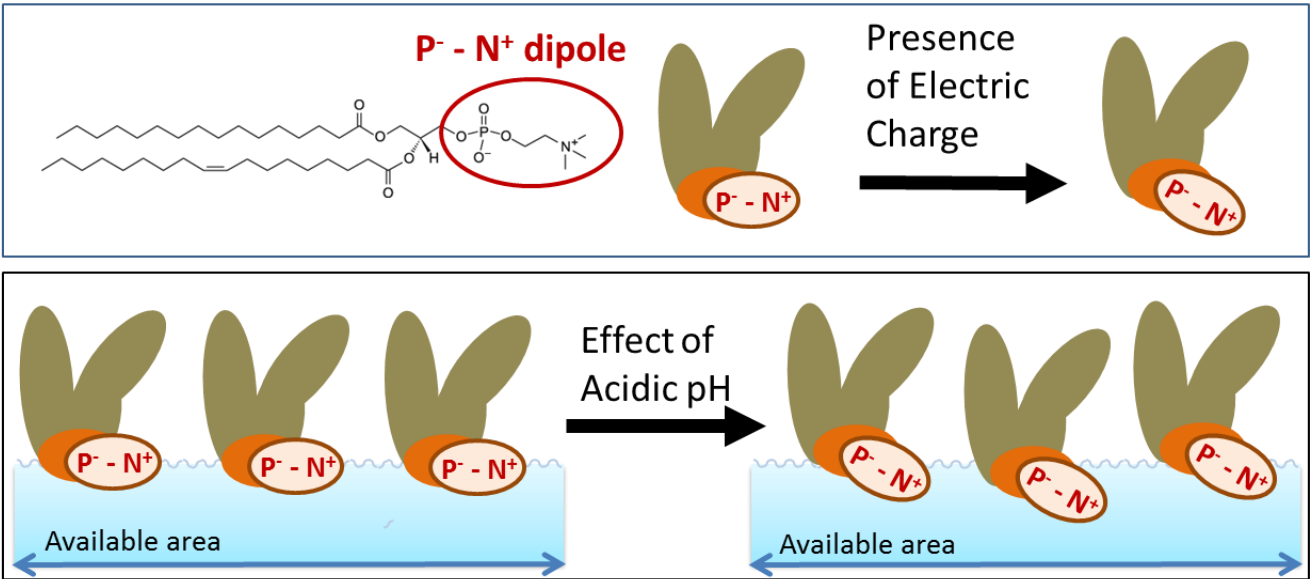
Figure 3. Schematic figure of head-group reorientation of unsaturated phospholipids affected by pH of solution. Decrease in pH causes a reorientation of the head-group at the interface, which could lead to increased packing density at interfacial area. The increased packing density is detected by measuring the interfacial viscosity of the phospholipid monolayer.

Figure 4 represent Changes in total friction drag and surface viscosity as a function of pH (4.4 and 7.4) and surface pressure (20, 25, and 30 mN/m) of **POPE**. Results are presented as mean and ± 1.5SE (n >= 3). The "0.14 line" represents the value of total friction of half immersed rod (0.14) in water as control. At SP 30mN/m and pH 4.4, POPE has a significant increase in surface viscosity compared to pH 7.4 (p<0.005, one-way ANOVA).

Panel A
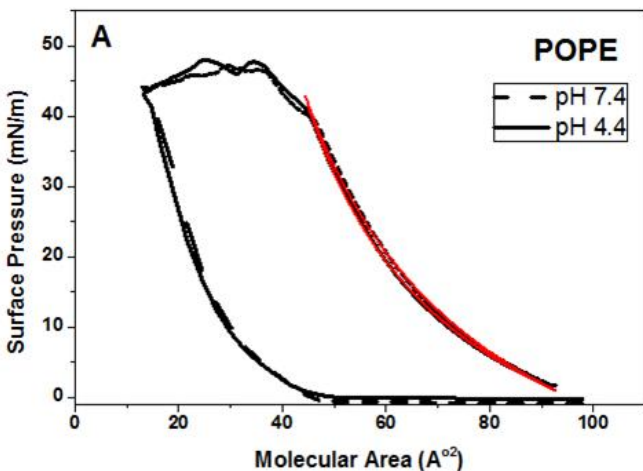
Parameters	POPE pH7.4	POPE pH4.4
$\omega\ (A^{o2})$	16.6	12.38
$\omega_0\ (A^{o2})$	3.49	2.22
$\Pi_{coh}\ (\dfrac{mN}{m})$	24.18	28.05
$n = \dfrac{\omega}{\omega_0}$	4.75	5.6
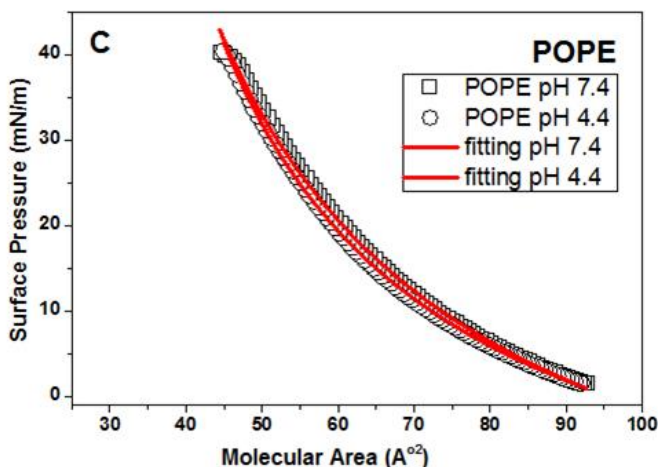
Figure 5A. Surface pressure vs area isotherm of **POPE** monolayer at pH 7.4 (solid curve) and pH 4.4 (dashed curve) lines (presented as average, N=3). **The red line** represents the fitting curve based on generalized Volmer's equation for insoluble monolayers to POPE isotherms at both pH 4.4 and 7.4. **Panel 5B** w = Average molecular area of amphiphilic species at the interface. w/ w_0 = n (accounts for associations between the amphiphilic molecules). π_{coh} = Cohesion pressure between molecules.
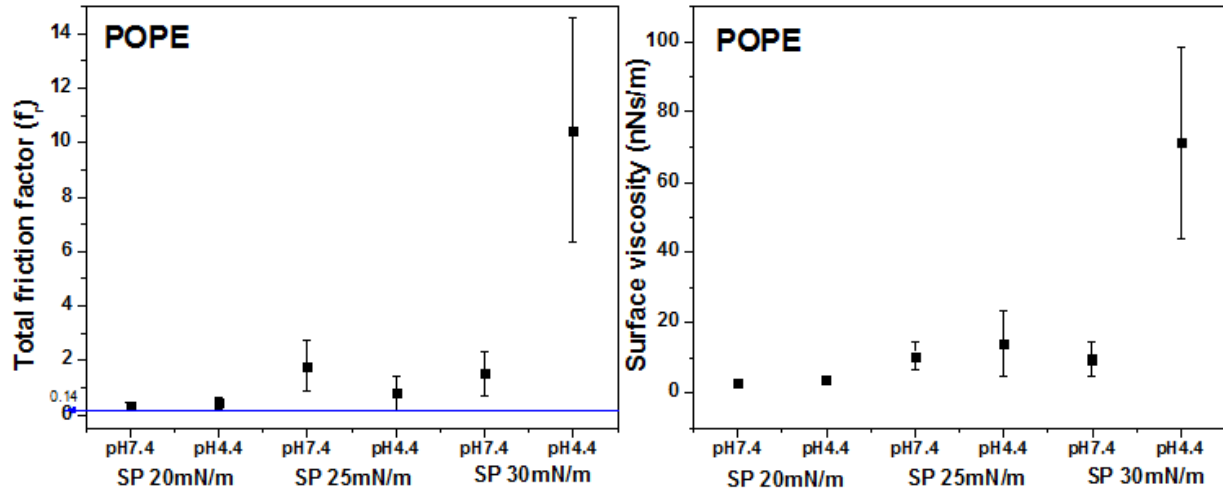
Figure 6 represent Changes in total friction drag and surface viscosity as a function of pH (4.4 and 7.4) and surface pressure (20, 25, and 30 mN/m) of **POPG**. Results are presented as mean and ±1.5SE (n >= 3). The "0.14 line" represents the value of total friction of half immersed rod (0.14) in water as control. POPG do not have a significant viscosity change between pH4.4 and pH7.4 or with increase of surface pressure.
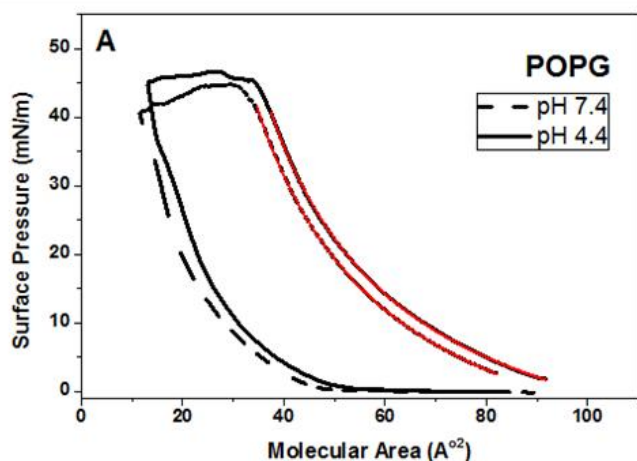
| Parameters	POPG pH7.4	POPG pH4.4
$\omega\ (A^{o2})$	2.16	6.66
$\omega_0\ (A^{o2})$	0.42	1.46
$\Pi_{coh}\ (\dfrac{mN}{m})$	23.91	20.35
$n = \dfrac{\omega}{\omega_0}$	5.1	4.6
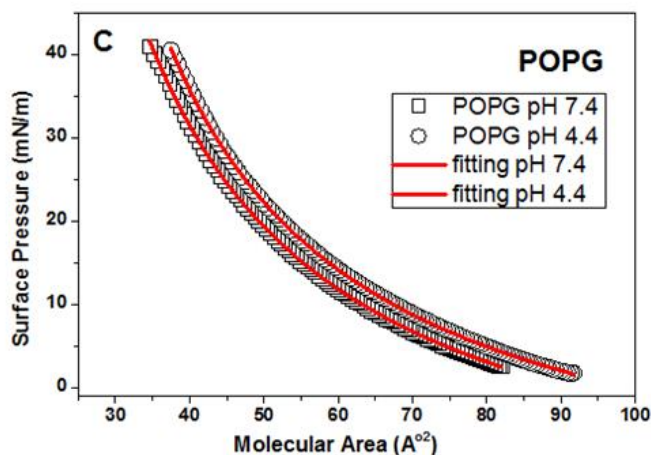
Figure 7A. Surface pressure vs area isotherm of **POPG** monolayer at pH 7.4 (solid curve) and pH 4.4 (dashed curve) lines (presented as average, N=3). **The red line** represents the fitting curve based on generalized Volmer's equation for insoluble monolayers to POPG isotherms at both pH 4.4 and 7.4. **Panel 7B** w = Average molecular area of amphiphilic species at the interface. w/ w_0 = n (accounts for associations between the amphiphilic molecules). π_{coh} = Cohesion pressure between molecules.
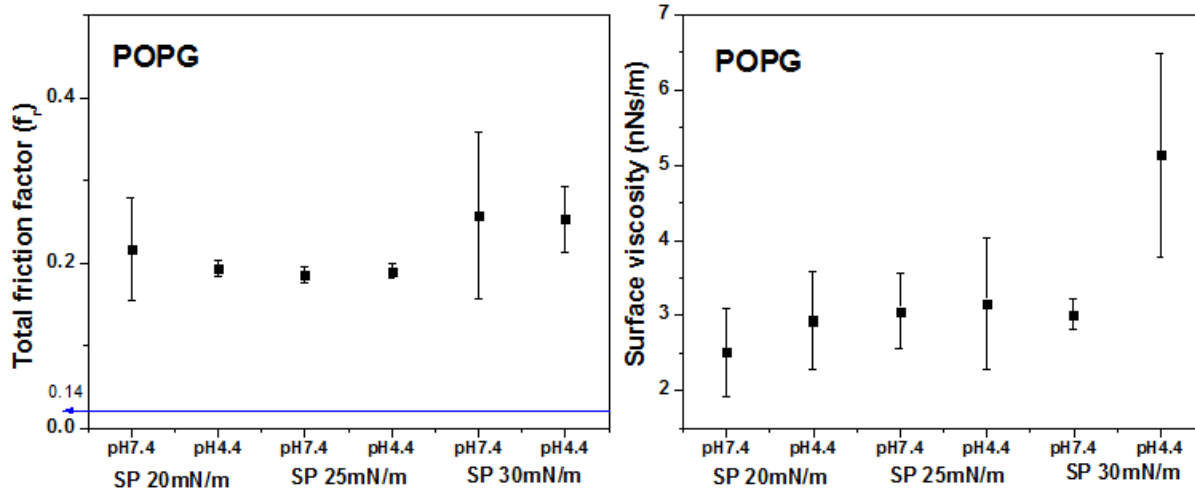
Figure 8 represent Changes in total friction drag and surface viscosity as a function of pH (4.4 and 7.4) and surface pressure (20, 25, and 30 mN/m) of **POPS**. Results are presented as mean and ±1.5SE (n >= 3). The "0.14 line" represents the value of total friction of half immersed rod (0.14) in water as control. At SP 30 mN/m the surface viscosity of POPS at pH 4.4 is three times more than pH 7.4 (p<0.005, one-way ANOVA).
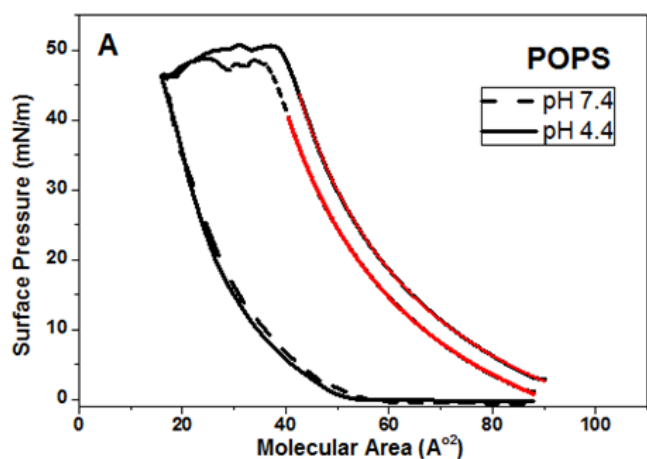
B

| Parameters	POPS pH7.4	POPS pH4.4
$\omega \ (A^{o2})$	9.78	9.21
$\omega_0 \ (A^{o2})$	1.98	1.64
$\Pi_{coh} \ \left(\dfrac{mN}{m}\right)$	24.82	26.13
$n = \dfrac{\omega}{\omega_0}$	4.9	5.6
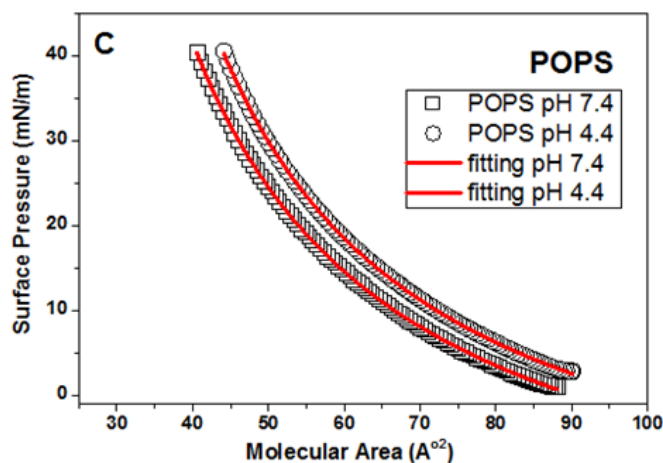
Figure 9A. Surface pressure vs area isotherm of **POPS** monolayer at pH 7.4 (solid curve) and pH 4.4 (dashed curve) lines (presented as average, N=3). <u>**The red line**</u> represents the fitting curve based on generalized Volmer's equation for insoluble monolayers to POPS isotherms at both pH 4.4 and 7.4. **Panel 9B** w = Average molecular area of amphiphilic species at the interface. w/ w_0 = n (accounts for associations between the amphiphilic molecules). π_{coh} = Cohesion pressure between molecules.
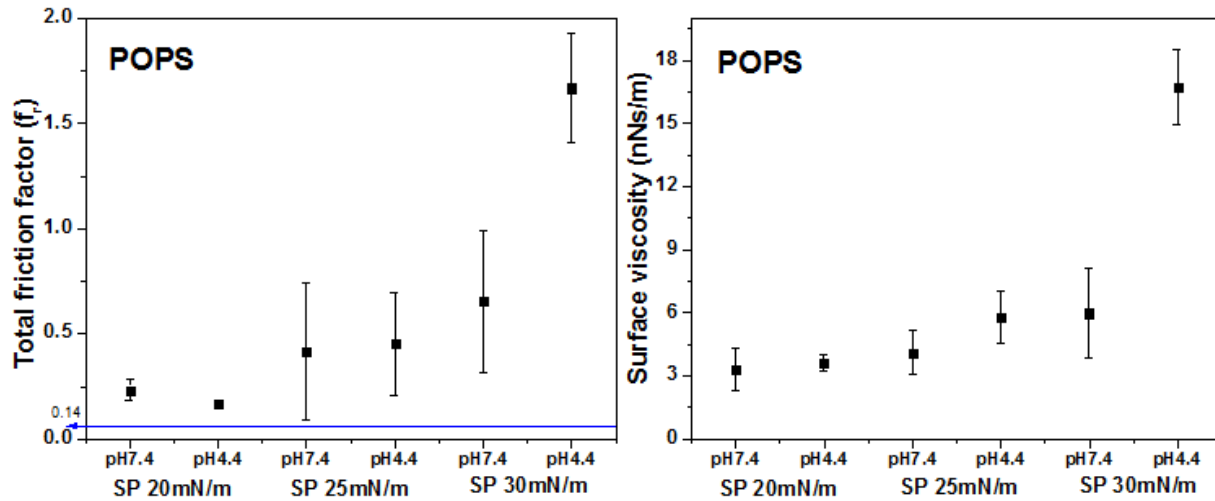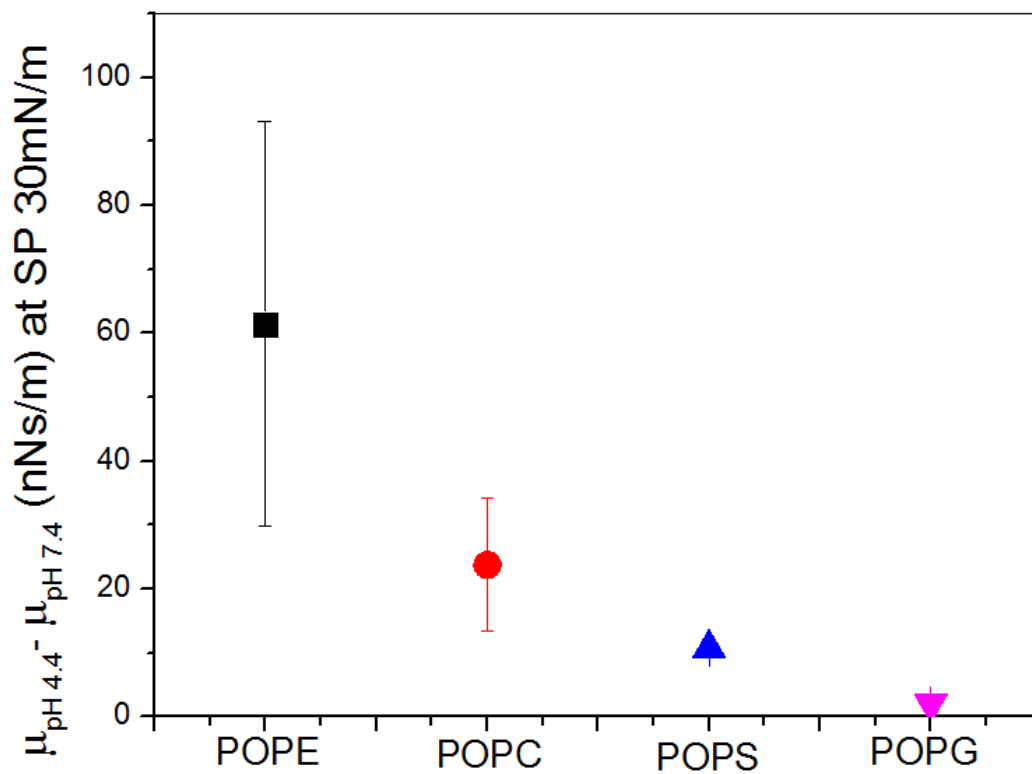
Figure 10 represents changes in surface viscosity of POPE, POPC, POPS, and POPG monolayers between pH 4.4 and 7.4 at surface pressure 30 mN/m. Results are presented as difference between means and STDEV of two groups of data.
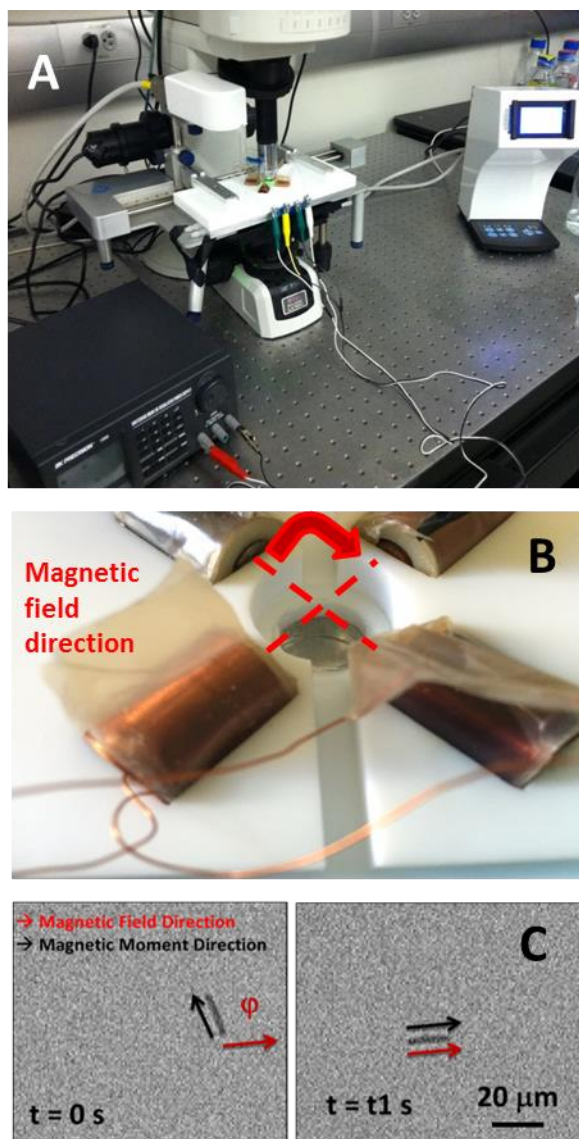
Figure S1A. The Langmuir trough has been coupled with set of magnetic coils, a fluorescence microscope, and a pressure sensor to simultaneously visualize alterations in phospholipid packing and record reorientation of rods to measure interfacial rheological properties while surface pressure changed. **Figure S1B** shows the 90 degree position of the magnetic coils. **Figure S1C** shows the representative images of a nanorod reorientation at air-water interface. By applying the magnetic torque, nanorod reorients toward magnetic field at the air-water interface.
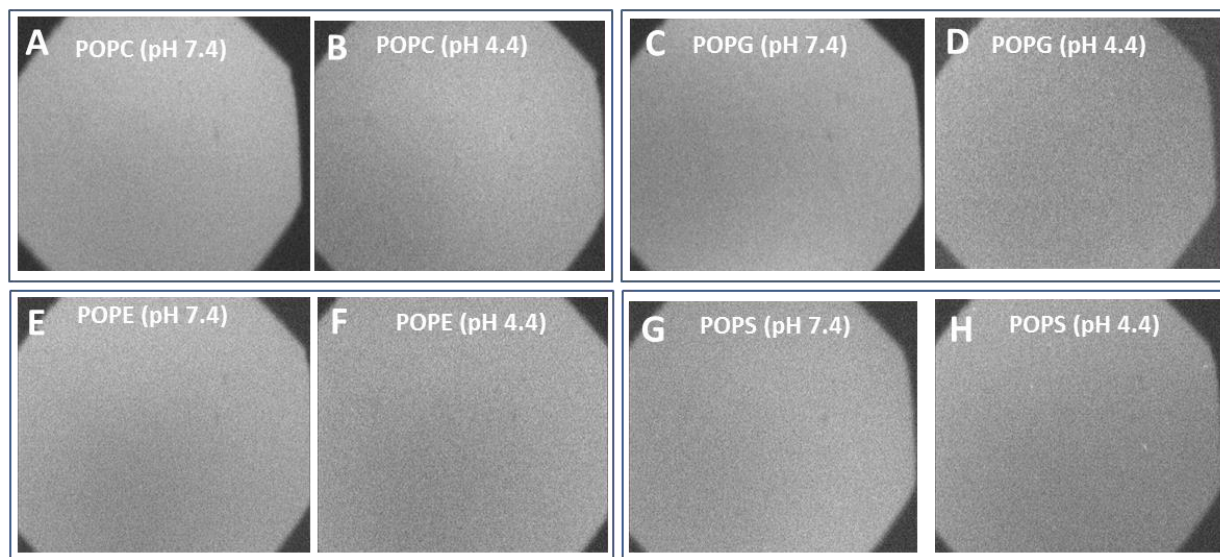
Figure S2. Fluorescence image of **POPC** monolayers at surface pressure 30 mN/m of both pH 4.4 and pH 7.4 at air-water interface using a Langmuir trough. These images indicate that there is no domain formation at air-water interface at studied surface pressures.
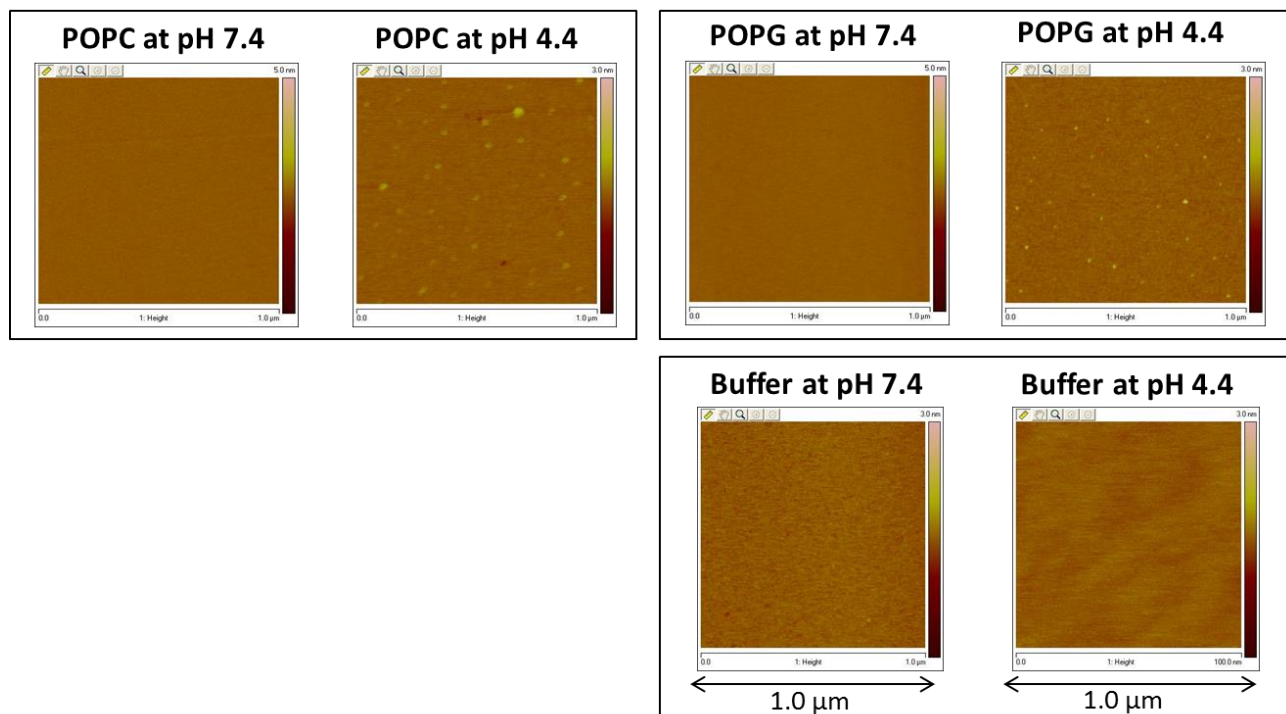
Figure S3. AFM Images of POPC, POPE, and POPG monolayers at pH 7.4 and pH 4.4. The monolayers have been transferred on a freshly cleaved mica sheet at surface pressure 30mN/m. the color bars indicate the heights of the features in morphological imaging of monolayers to study the effect of pH on monolayer packing.

3.7. References

1. Alberts, B., et al., *Molecular biology of the cell, 1994.* Garland, New York: p. 139-194.
2. Van Meer, G., D.R. Voelker, and G.W. Feigenson, *Membrane lipids: where they are and how they behave.* Nature reviews molecular cell biology, 2008. **9**(2): p. 112-124.
3. Vanni, S., et al., *A sub-nanometre view of how membrane curvature and composition modulate lipid packing and protein recruitment.* Nature communications, 2014. **5**.
4. Dautry-Varsat, A., A. Ciechanover, and H.F. Lodish, *pH and the recycling of transferrin during receptor-mediated endocytosis.* Proceedings of the National Academy of Sciences, 1983. **80**(8): p. 2258-2262.
5. Mosesson, Y., G.B. Mills, and Y. Yarden, *Derailed endocytosis: an emerging feature of cancer.* Nature Reviews Cancer, 2008. **8**(11): p. 835-850.
6. Sorkin, A. and M. von Zastrow, *Signal transduction and endocytosis: close encounters of many kinds.* Nature reviews Molecular cell biology, 2002. **3**(8): p. 600-614.
7. Suresh, S. and J.M. Edwardson, *Phase separation in lipid bilayers triggered by low pH.* Biochemical and biophysical research communications, 2010. **399**(4): p. 571-574.
8. Aloia, R.C. and J.M. Boggs, *Membrane Fluidity in Biology: Disease Processes*. 2013: Academic Press.
9. Arora, A., et al., *Modulation of liposomal membrane fluidity by flavonoids and isoflavonoids.* Archives of Biochemistry and Biophysics, 2000. **373**(1): p. 102-109.
10. Su, Y., W.F. DeGrado, and M. Hong, *Orientation, dynamics, and lipid interaction of an antimicrobial arylamide investigated by 19F and 31P solid-state NMR spectroscopy.* Journal of the American Chemical Society, 2010. **132**(26): p. 9197-9205.
11. Wang, M., et al., *Incorporating headgroup structure into the Poisson-Boltzmann model of charged lipid membranes.* The Journal of chemical physics, 2013. **139**(2): p. 024703.
12. Brown, M.F. and J. Seelig, *Ion-induced changes in head group conformation of lecithin bilayers.* Nature, 1977. **269**(5630): p. 721-723.
13. Doux, J.P., B.A. Hall, and J.A. Killian, *How Lipid Headgroups Sense the Membrane Environment: An Application of 14 N NMR.* Biophysical journal, 2012. **103**(6): p. 1245-1253.
14. Saffman, P.G. and M. Delbruck, *Brownian motion in biological membranes.* Proc. Nat. Acad. Sci. USA, 1975. **72**: p. 311-313.
15. Choi, S.Y., et al., *Active microrheology of phospholipid monolayers: seeing stretching, flowing, yielding and healing.* Nature Communications, 2011. **2**: p. 312.
16. Reynaert, S., et al., *Analysis of the magnetic rod interfacial stress rheometer.* Journal of Rheology, 2008. **52**(1): p. 261-285.
17. Ghazvini, S., et al., *Monitoring phases and phase transitions in phosphatidylethanolamine monolayers using active interfacial microrheology.* Soft matter, 2015. **11**(17): p. 3313-3321.
18. Dhar, P., et al., *Active Interfacial Shear Microrheology of Aging Protein Films.* Physical Review Letters, 2010. **104**(1): p. -.
19. Dhar, P., et al., *Autonomously moving local nanoprobes in heterogeneous magnetic fields.* Journal of Physical Chemistry C, 2007. **111**(9): p. 3607-3613.
20. Dhar, P., et al., *Autonomously moving nanorods at a viscous interface.* Nano Letters, 2006. **6**: p. 66-72.
21. Dhar, P., et al., *Autonomously moving nanorods at a viscous interface.* Nano letters, 2006. **6**(1): p. 66-72.
22. Dhar, P., et al., *Active interfacial shear microrheology of aging protein films.* Physical review letters, 2010. **104**(1): p. 016001.
23. Dhar, P., et al., *Autonomously moving local nanoprobes in heterogeneous magnetic fields.* The Journal of Physical Chemistry C, 2007. **111**(9): p. 3607-3613.

24.   Butler, J., *The thermodynamics of the surfaces of solutions.* Proceedings of the Royal Society of London. Series A, Containing Papers of a Mathematical and Physical Character, 1932. **135**(827): p. 348-375.
25.   Fainerman, V. and D. Vollhardt, *Equations of state for Langmuir monolayers with two-dimensional phase transitions.* The Journal of Physical Chemistry B, 1999. **103**(1): p. 145-150.
26.   Fainerman, B. and D. Vollhardt, *Equation of state for monolayers under consideration of the two-dimensional compressibility in the condensed state.* The Journal of Physical Chemistry B, 2003. **107**(14): p. 3098-3100.
27.   Fainerman, V. and D. Vollhardt, *Surface pressure isotherm for the fluid state of langmuir monolayers.* The Journal of Physical Chemistry B, 2006. **110**(21): p. 10436-10440.
28.   Vollhardt, D., V. Fainerman, and S. Siegel, *Thermodynamic and textural characterization of DPPG phospholipid monolayers.* The Journal of Physical Chemistry B, 2000. **104**(17): p. 4115-4121.
29.   Kuo, C.-C., et al., *Particle size effects on collapse in monolayers.* Langmuir, 2012. **28**(39): p. 13976-13983.
30.   Gurtovenko, A.A. and A.S. Lyulina, *Electroporation of asymmetric phospholipid membranes.* The Journal of Physical Chemistry B, 2014. **118**(33): p. 9909-9918.
31.   Scherer, P.G. and J. Seelig, *Electric charge effects on phospholipid headgroups. Phosphatidylcholine in mixtures with cationic and anionic amphiphiles.* Biochemistry, 1989. **28**(19): p. 7720-7728.
32.   Bechinger, B. and J. Seelig, *Interaction of electric dipoles with phospholipid head groups. A deuterium and phosphorus-31 NMR study of phloretin and phloretin analogs in phosphatidylcholine membranes.* Biochemistry, 1991. **30**(16): p. 3923-3929.
33.   Akutsu, H. and J. Seelig, *Interaction of metal ions with phosphatidylcholine bilayer membranes.* Biochemistry, 1981. **20**(26): p. 7366-7373.
34.   Marassi, F.M. and P.M. Macdonald, *Response of the phosphatidylcholine headgroup to membrane surface charge in ternary mixtures of neutral, cationic, and anionic lipids: a deuterium NMR study.* Biochemistry, 1992. **31**(41): p. 10031-10036.
35.   Wang, B., et al., *Nanoparticle-induced surface reconstruction of phospholipid membranes.* Proceedings of the National Academy of Sciences, 2008. **105**(47): p. 18171-18175.
36.   Als-Nielsen, J., et al., *Principles and applications of grazing incidence x-ray and neutron scattering from ordered molecular monolayers at the air-water interface.* Physics Reports, 1994. **246**(5): p. 251-313.

Chapter 4: Interfacial rheology of lung surfactant lipids and SP-B protein

4.1. Introduction

In order for the mammalian lungs to compress and expand during the breathing cycle, the surface tension is reduced by presence of a lipid-protein mixture, called lung surfactant, at the interface [1]. Lung surfactant is regularly synthesized, secreted, and recycled by alveoli cells [1, 2]. Unfortunately, in patients with respiratory distress syndrome (lung injury or inflammation) or in un-developed lungs of premature infants, lung surfactant can be respectively dysfunctional or deficient [1-3]. The consequences of dysfunctional or deficient lung surfactant could be as severe as patient death [1, 2, 4]. To treat patients with respiratory distress syndrome, replacement lung surfactant has been developed commercially [1, 4, 5]. While clinical studies have confirmed the beneficial effect of replacement lung surfactant for premature infants that suffer from lack of LS, these therapies were less successful to treat dysfunctional lung surfactant [1, 5]. It is expected that to effectively treat patients with respiratory diseases that suffer from injury or inflammation if the lung, a replacement lung surfactant should be designed that not only has an optimal surface activity but agents to resist the inflammation and therefore work as a multi-targeted drug [1, 2, 5]. To achieve this aim, careful biophysical analysis of replacement LS candidates and their composition is required.

Recent interfacial characterization of lipid-protein mixtures mimicking LS, have shed light on important dynamic properties of LS including fluidity and reversible collapse of the film [6-9]. The properties of LS film are dynamic, since it continuously goes through a two dimensional (2D) compression-expansion cycle[10]. The lateral force that causes 2D compression-expansion of the film, has been studied using Langmuir monolayers [7, 8, 10-13]. One of the main features of the monolayers is its collapse at the end of each compression cycle when the available surface area is minimum [10]. The film is irreversibly collapsed if some portion of the film is lost to the subphase

or if it is rigid enough that the film fractures [8]. However, if the film does not get "squeezed out" to the subphase and if it is not too rigid, reversible collapse enables repetitive compression-expansion cycles [8]. Several studies using fluorescence microscopy, digital imaging analysis, atomic force microscopy, and surface pressure-area isotherms have studied the relationship between nanoscopic properties of lipid-protein mixtures and their macroscopic properties, showing reversible collapse is a tunable property based on film composition [6, 8-10, 14, 15]. The collapse mechanism is also linked to the fluidity of the film, and has been characterized based on presence of unsaturated phospholipids, proteins, palmitic acid, etc. [6-9, 14, 15].

Natural LS is a mixture of approximately 90% lipids and 10% surfactant proteins (SP) A, B, C, and D [1, 2]. Almost one third of the lipid portion consists of 1,2-dipalmitoyl-sn-glycero-3-phosphocholine (DPPC) ,a zwitterionic saturated phospholipid [1, 2]. The remaining lipids are mostly unsaturated with PC (zwitterionic) and PG (anionic) headgroups [1, 2]. DPPC monolayers can pack tightly to lower the surface tension down to almost zero, reducing the energy required for the lungs to expand [1, 2, 10]. However, without the presence of proteins and unsaturated phospholipids, the DPPC monolayer is rigid without the ability to reversibly collapse [1, 2, 10]. It has been shown that the presence of SP-B and SP-C proteins decrease the loss of material to the subphase, facilitating reversible collapse [1, 8, 9, 15-17]. It has been suggested that the interaction between the positively charged SP-B protein and negatively charged PG headgroup of unsaturated lipids strengthens the uniformity of the LS film to promote folding of the film during compression-expansion rather than the squeezing out of the portion of the film [8, 9, 11, 12, 15, 17]. Interestingly, *in vivo* studies have confirmed the importance of SP-B and SP-C proteins in the success of replacement lung surfactants [1, 9, 15]. Elaborating on the essential dynamic chemical-mechanical properties of lipid-protein mixtures, as described by Lee *et. al.*, parameters should be

found to characterize and quantify the fluidity of the layer in a way that could predict the reversibility of the collapse [8].

The fluidity or rigidity of a layer can be measured in terms of its rheological properties. Measuring the surface rheological properties of lipid mixtures at the air-liquid interface is not trivial. The difficulty stems from the inability to isolate the two-dimensional surface that is decoupled from the bulk sub-phase, as first identified by Saffmann and Dulbruck for lipid membranes [18]. Detailed analysis of probe movement in lipid-laden interfaces suggests that this decoupling, quantified by the Boussinesq number B, should be much greater than one (B>>1) [19-21]. To satisfy the B>>1, smaller probe geometries have been designed and incorporated, increasing the sensitivity of surface viscosity measurements down to 10^{-7} Ns/m [19-24]. Several groups with different rheometrical instruments and sensitivities have attempted to quantify the mechanical properties of pure lipid monolayers at the air-water interface [19, 21, 25]. These studies have shown that the surface viscosity of lipid monolayers increases by orders of magnitude with an increase of surface pressure due to increase of packing density [26, 27]. The change in surface pressure in pure lipid monolayer corresponds to 2D phases and phase transitions from a liquid-expanded phase to a liquid-condensed phase [28]. Additionally, the viscoelastic properties of binary mixtures are significantly different from pure monolayers [17]. Sachan *et. al.* have shown that the presence of cholesterol and palmitic acid decreases the surface viscosity of the DPPC monolayer up to three orders of magnitude with an increase in surface pressure [29].

Furthermore, presence of other LS components in a monolayer mixture could affect the surface rheology of the film. Since unsaturated phospholipids have a lower packing density than saturated phospholipids, they create non-homogeneous patches of poorly packed phospholipids in binary mixtures with saturated lipids [1, 8, 9]. Furthermore, the collapse pressure of unsaturated

lipids, that provides information on maximum packing and minimum surface tension, are lower than saturated lipids at room temperature and more similar to collapse pressure of saturated lipids at higher temperatures [8]. Therefore, the presence of unsaturated lipids, such as POPG in a phospholipid mixture is expected to reduce the surface viscosity compared to a pure saturated lipid monolayer [17]. While the viscoelastic properties of DPPC monolayer have been studied, the contribution of both unsaturated lipids and proteins on dynamic mechanical properties has not been quantified. Moreover, since the presence of unsaturated lipids could significantly increase the fluidity of the monolayer, higher sensitivity is required to measure the interfacial rheological properties of the lipid mixture in the liquid-expanded to liquid-condensed range. To achieve this higher sensitivity measurement, a unique rheological set-up has been used in this study. The rheological probes are micron sized and able to measure to viscosities as low as 10^{-9} Ns/m; thus, the use of these probes has made our studies possible.

Our goal was to quantify the effect of the following variables on overall the mechanical properties of a mixed monolayer: 1) introduction of unsaturated lipid tails in mixed DPPC-unsaturated lipid monolayers, 2) effect of phospholipid head-group charge, and 3) presence of protein. We studied the most abundant phospholipids of the natural lung surfactant: DPPC (1,2-dipalmitoyl-sn-glycero-3-phosphocholine), POPC (1-palmitoyl-2-oleoyl-sn-glycero-3-phosphocholine), and POPG (1-palmitoyl-2-oleoyl-sn-glycero-3-phospho-(1'-rac-glycerol)) (Table 1). We have used a synthetic form of SP-B, miniB, which has been designed to mimic the 3D structure of the N- and C-terminals of SP-B. Since miniB shares the same active site as SP-B, they have similar interfacial functionality [30, 31]. Monolayers containing mixtures of zwitterionic-anionic (DPPC-POPG) headgroups were compared with zwitterionic-zwitterionic ones (DPPC-POPC) in the absence and presence of miniB to explore the effect of head-group

interactions on the overall fluidity of the monolayer. The interaction of each mentioned head-group with miniB shows how the headgroup charge can influence the surface viscosity and elasticity and therefore, increase the possibility of reversible compression-expansion. These results could be used in developing more efficient replacement lung surfactants to treat various forms of respiratory distress.

4.2. Materials and methods

HPLC grade chloroform solutions of 1,2-dipalmitoyl-*sn*-glycero-3-phosphocholine(DPPC), 1-palmitoyl-2-oleoyl-*sn*-glycero-3-phosphocholine(POPC), and 1-palmitoyl-2-oleoyl-*sn*-glycero-3-phospho-(1'-*rac*-glycerol) (POPG) were purchased from Avanti Polar Lipids, Alabaster, AL, and used as received. Texas Red® 1,2-dihexadecanoyl-sn-glycero-3-phosphoethanolamine, triethylammonium salt, (TXR-DHPE) was purchased in the dried form from Life Technologies (Invitrogen) and dissolved in HPLC grade chloroform. All organic solvents were purchased from Fisher Scientific. The subphase water (resistivity 18.2 MΩ/cm) was prepared using a Millipore Gradient System (Billerica, MA). The lipids were stored at -20 ᵒC when not in use.

Stock solution of DPPC-POPC and DPPC-POPG samples were made by mixing in a 70:30 molar ratio of DPPC: POPC and DPPC: POPG. The 70:30 molar ratio between DPPC and POPC (or POPG) have been chosen since many synthetic lung surfactants contain this ratio between PC and PG headgroup. The stock solution of miniB was prepared in a 3:1 mixture of chloroform and methanol prior to mixing with lipids. The DPPC-POPC-miniB and DPPC-POPG-miniB samples were prepared using 5wt. % miniB with DPPC-POPC and DPPC-POPG (70:30 molar ratio) ; similarly DPPC-POPG-miniB sample has been made. The nickel nanorods used as probes were

synthesized by electrochemical deposition of nickel into alumina templates 35, then magnetized, thoroughly cleaned (multiple washes with isopropyl alcohol, water, and chloroform), and dispersed in isopropyl alcohol.

A 1 mg/ml solution of all samples with 1 wt% of TXR-DHPE in chloroform was used as a spreading solution. The samples were spread drop-wise from a micro-syringe onto the air/water interface of the rheology trough, and the chloroform allowed to evaporate for 20 minutes. Then a 15µl of the rod solution was deposited uniformly using a micro-syringe at the air/water interface in the trough. The isopropyl alcohol was allowed to evaporate for at least 45 minutes before recording any date. Similar to chapter two and three, the films were gradually compressed by the barriers of the Langmuir trough and during the compression the reorientation of the nanorods were recorded at known surface pressures. Similar to previous studies, a filter-paper Wilhelmy plate on a Langmuir trough (KSV-NIMA, Biolin Scientific) was used to measure the surface pressure as a function of area occupied by the phospholipid molecules. The methods used to reorient the rod and analyze their movement was explained in details in chapter two and three.

4.3. Results and Discussion

The surface pressure-molecular area $(\pi - A)$ isotherms represents phase behavior of surfactant molecules at the air-water interface. Several distinct phases are noted, as the surfactant film is compressed, starting from a gaseous phase at very high area per molecules (large surface area) to liquid expanded (LE) phase, liquid condensed (LC) phase and finally the solid phase. The $\pi - A$ isotherms of the DPPC-POPC, DPPC-POPC-miniB (5 wt.%), DPPC-POPG, and DPPC-POPG-miniB (5 wt.%) are presented in Fig. 1. Our results show that for both lipid mixtures studied here (DPPC-POPG and DPPC-POPC), the addition of miniB shifted the mean molecular area to

higher values for the same surface pressure; this shift indicates the insertion of protein to the lipid mixture monolayer at the air-liquid interface.

The slope of the isotherm has changed in both DPPC-POPC and DPPC-POPG by addition of the protein. The sudden change of slope corresponds to the phase transition of the lipid monolayers that had changed by addition of the protein. The plateau at 15mN/m, corresponding to a 1st order phase transition in DPPC-POPC, occurred at 10mN/m in the presence of miniB. For the DPPC-POPG monolayer the plateau corresponding to a 1st order phase transition occurred at 10mN/m, while in the presence of miniB occurred at 8mN/m. As it is expected for lipid mixture monolayers, there was a sudden change in slope of isotherm in DPPC-POPG-miniB and DPPC-POPC-miniB at surface pressure 42 and 43 mN/m respectively that indicates the loss of unsaturated lipids where they are "squeezed out" to the subphase.

The surface viscosities of lipid mixtures and lipid-protein mixtures are presented in Figure 2. As the surface pressure increased, the surface viscosity increased for all groups except for the DPPC-POPC mixture. Pure DPPC monolayer reached great surface viscosity values in lower surface pressures. For example, at a surface pressure of 22 mN/m, a surface viscosity of $7*10^{-5}$ Ns/m has been measured for pure DPPC. Surface viscosity of DPPC-POPG and DPPC-POPC were decreased compared to pure DPPC monolayer. Based on our previous studies, unsaturated phospholipids such as POPC and POPG have a very low surface viscosity, equal to or below the sensitivity of our measurements (10^{-9} Ns/m) up to the collapse surface pressure at room temperature. Therefore, it is not surprising that combining the unsaturated lipids with DPPC decreased the surface viscosity of the mixture compared to pure DPPC.

The proportion of saturated to unsaturated lipids is 7 to 3 in both DPPC-POPG and DPPC-POPC mixtures; however, the surface fluidity of the DPPC-POPC was higher, resulting in lower surface viscosity. The significant difference in the surface viscosity of DPPC-POPC compared to DPPC-POPG, suggest that the presence of negatively charged headgroups contribute differently to headgroup interactions and the overall packing. In addition to the difference between headgroup charges, the PG headgroup has a smaller size compared to the PC headgroup that could enhance the packing. The surface viscosity of DPPC-POPG was only decreased about ten-fold compared to values of pure DPPC at a surface pressure of 21-23 mN/m, while the surface viscosity of DPPC-POPC was decreased about 10000-fold.

Our data of DPPC-POPG surface viscosity using nano-rod probes matched the data of Alonso *et. al.* for the surface viscosity of DPPC-POPG at a surface pressure of 30 mN/m [17]. Alonso *et. al.* used a magnetic needle with a sensitivity of 10^{-6} Ns/m for their measurements [17]. However, because of the sensitivity limitations of commercial instruments, the jump of surface viscosity between the liquid-expanded phase and the liquid-condensed phase has not been measured for the lipid mixtures, including DPPC-POPG. Since the liquid expanded phase has a surface viscosity of 10^{-9} Ns/m or lower, Alonso *et. al.* were not able to detect the jump in surface viscosity as a result of the increase of surface pressure that we have shown here for DPPC-POPG [17].

The addition of protein significantly increased the surface viscosity of lipid mixtures. In the case of DPPC-POPG, 5 wt.% of miniB increased the surface viscosity 3- to 10-fold in respectively in the liquid-expanded and liquid-liquid condensed phases. For the DPPC-POPC mixture, addition of protein increased the surface viscosity even more significantly. At a surface pressure of 40 mN/m, the surface viscosity of DPPC-POPC-miniB (5 wt.%) is 1000-fold higher

than that of DPPC-POPC. At surface pressures below 20 mN/m, corresponding to liquid expanded phase, the surface viscosity of DPPC-POPC-miniB increased slightly compared to the DPPC-POPC monolayer in this range of surface pressure.

The miniB, synthetic form of native SP-B, has charged amphipathic α-helices, which accommodate the interaction of the protein with lipid mixtures [30-32]. Since miniB is designed to match the amino acid sequence and the secondary α-helical structure of the SP-B, [30-32] our result is comparable to previous findings of increased viscosity of DPPC:POPG:Palmitic-acid: 5wt. %SP-B compared to DPPC:POPG:Palmitic-acid [17]. The influence of the charge of the unsaturated head group is very relevant since the unsaturated lipids tend to stay outside of the packed domains, and therefore their interaction with protein, which also stays outside of packed domains, could be key to understanding overall monolayer fluidity [8, 9, 12]. Previous studies using NMR have also shown a reorientation of head-group moiety of phospholipids in response to partial charges, and this reorientation could result in higher packing density [33, 34]. Wang *et. al.* has specifically shown a gelation in the DPPC lipid bilayer as a result of charges in close vicinity to the lipid [35]. Additionally, our previous studies have shown the sensitivity of POPC monolayers to the pH of the microenvironment.

The lipid domains emerge at the interface during the coexistence of liquid condensed-liquid expanded phase, as the surface area is reduced and the surface pressure is increased, the proportion of domain (solid phase) to liquid phase increases [1, 36, 37]. A two-dimensional analog of the three-dimensional free area model for viscosity of solid suspensions in liquid could be fitted to the surface viscosity of the monolayer based on the interfacial area occupied by domains (solid) and the area occupied by the liquid [28, 29]. Figure 3 represents the surface viscosity data fitted to the free area model (Equation 1) across surface pressures at which the liquid condensed phase

emerges. η_s, A_0 and A_π are the surface viscosity, the minimum area the lipids could occupy before collapse of the monolayer, and the area at each surface pressure respectively. Except for DPPC-POPC, which did not show any significant increase in surface viscosity, the increase in surface viscosity of all three lipid-protein mixtures matched the exponential increase predicted by the 2-D free-area model.

$$ln\,\eta_s = \ln\eta_{s0} + B\left(\frac{A_0}{A_\pi - A_0}\right) \qquad (1)$$

4.4. Conclusions

In summary, we have investigated the surface pressure (surface tension) dependence of interfacial rheological properties of DPPC-POPC, DPPC-POPG, DPPC-POPC-miniB, and DPPC-POPG-miniB monolayers at the air-water interface. We presented the surface viscosity of lipid-protein mixtures that mimic lung surfactant at physiologically relevant surface pressures of 5-40 mN/m. It has been shown that the presence of proteins SP-B and SP-C facilitates the reversible folding of replacement lung surfactant and is therefore an essential component of *in vivo* trials [8, 9, 11, 15, 17]. Additionally, previous studies indicated that the synergistic interactions between SP-B and anionic unsaturated lipids with PG headgroups, have an effect on the collapse pressure and reversibility of the film [11, 12]. Our result showed that synthetic form of the active site of SP-B had the ability to regulate the surface viscosity up to 1000-fold at the low value of only 5 wt. %. The increased surface viscosity can be a key factor in accommodating the reversible collapse at high surface pressures. This finding could also enhance our understanding of how the proteins of cell membranes adjust the necessary fluidity of the membrane bilayer for transportation, signaling, and recognition[38, 39].

Furthermore, unsaturated lipids are known to have a higher re-adsorption rate to the LS monolayer during the expansion and reduced lost amount in the sub-phase compared to saturated DPPC [12]. Additionally, the unsaturated lipids were known to increase the fluidity of the monolayer to increase the spreading rate of lung surfactant [12]. Our study suggests that the charge of the head group moiety of the unsaturated lipids affects their role in fluidity of the monolayer. POPC reduced the surface viscosity of DPPC more than 1000-fold while POPG only reduced the surface viscosity of DPPC 10-fold. Thus large changes in surface viscosity could be achieved by small changes in composition of lipid-protein mixture.

Our rheological data motivates us to explore the interfacial mechanical properties of replacement lung surfactants made of lipids, proteins, and other components to adjust the composition and ratios in a systematic way to mimic the natural lung surfactant. In order to effectively relate these data to the efficacy of lung surfactant *in vivo,* we need to measure the surface viscosity of the natural lung surfactant across the relevant surface pressures. Previous studies with the magnetic needle surface viscometer showed that the two most common commercial replacement lung surfactants, Curosorf and Survanta, have significantly different surface viscosities, in particular between surface pressures of 30 mN/m and 40 mN/m [17]. The surface viscosities below 30mN/m were lower or equal to the sensitivity of the magnetic needle surface viscometer; therefore, the surface viscosity jump between liquid expanded to liquid condensed phase was not detected [17]. Future experiments in our group will include measurements of surface viscosity of commercial and natural lung surfactants to better evaluate the role of composition and ratio of the main components.

4.5. Table and figures
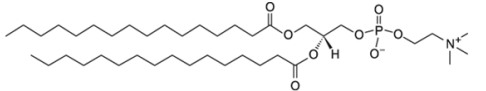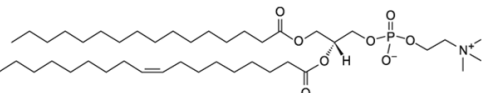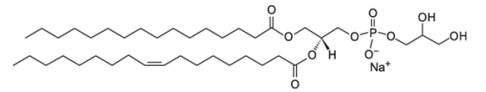
Acronym	Head group	Name	Classification	pKa	Structure
DPPC	PC	1,2-dipalmitoyl-*sn*-glycero-3-phosphocholine	Zwitterionic Saturated Phospholipid	pKa ~ 1.0	
POPC	PC	1-palmitoyl-2-oleoyl-*sn*-glycero-3-phosphocholine	Zwitterionic Unsaturated Phospholipid	pKa ~ 1.0	
POPG	PG	1-palmitoyl-2-oleoyl-*sn*-glycero-3-phospho-(1'-*rac*-glycerol)	Anionic Unsaturated Phospholipid	pKa ~ 3.5	

Table 1. Chemical structure of the lipids used in this study: DPPC, POPC, and POPG.
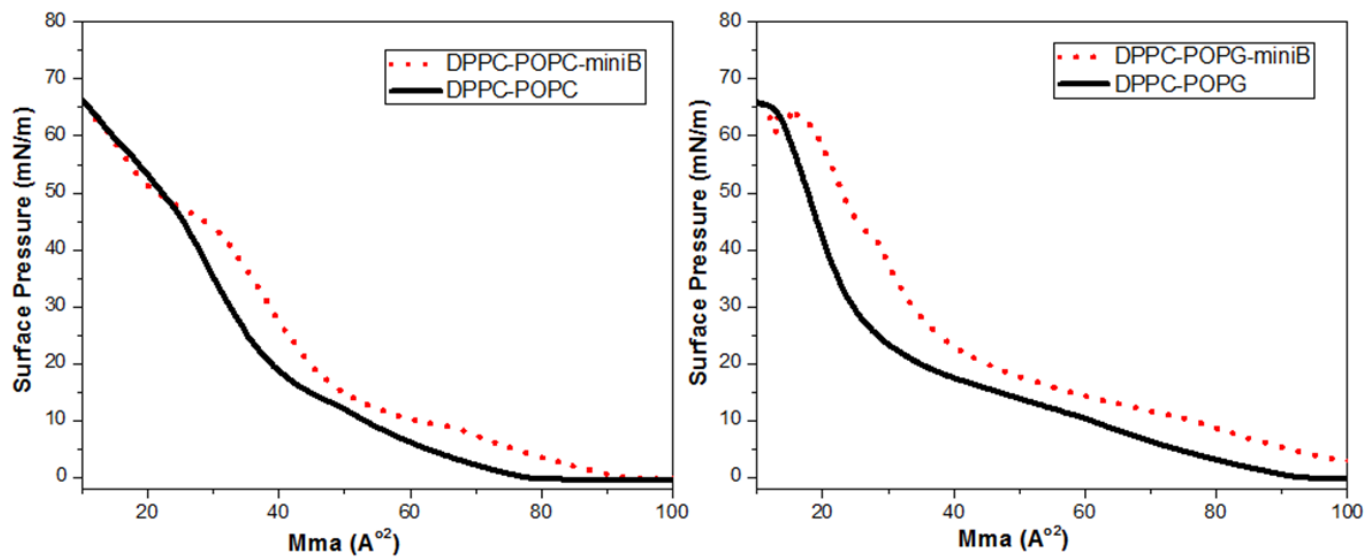
Figure 1. Surface pressure-area isotherms of DPPC-POPG, DPPC-POPC, DPPC-POPG-

miniB (5 wt.%) , and DPPC-POPC-miniB (5 wt.%) .
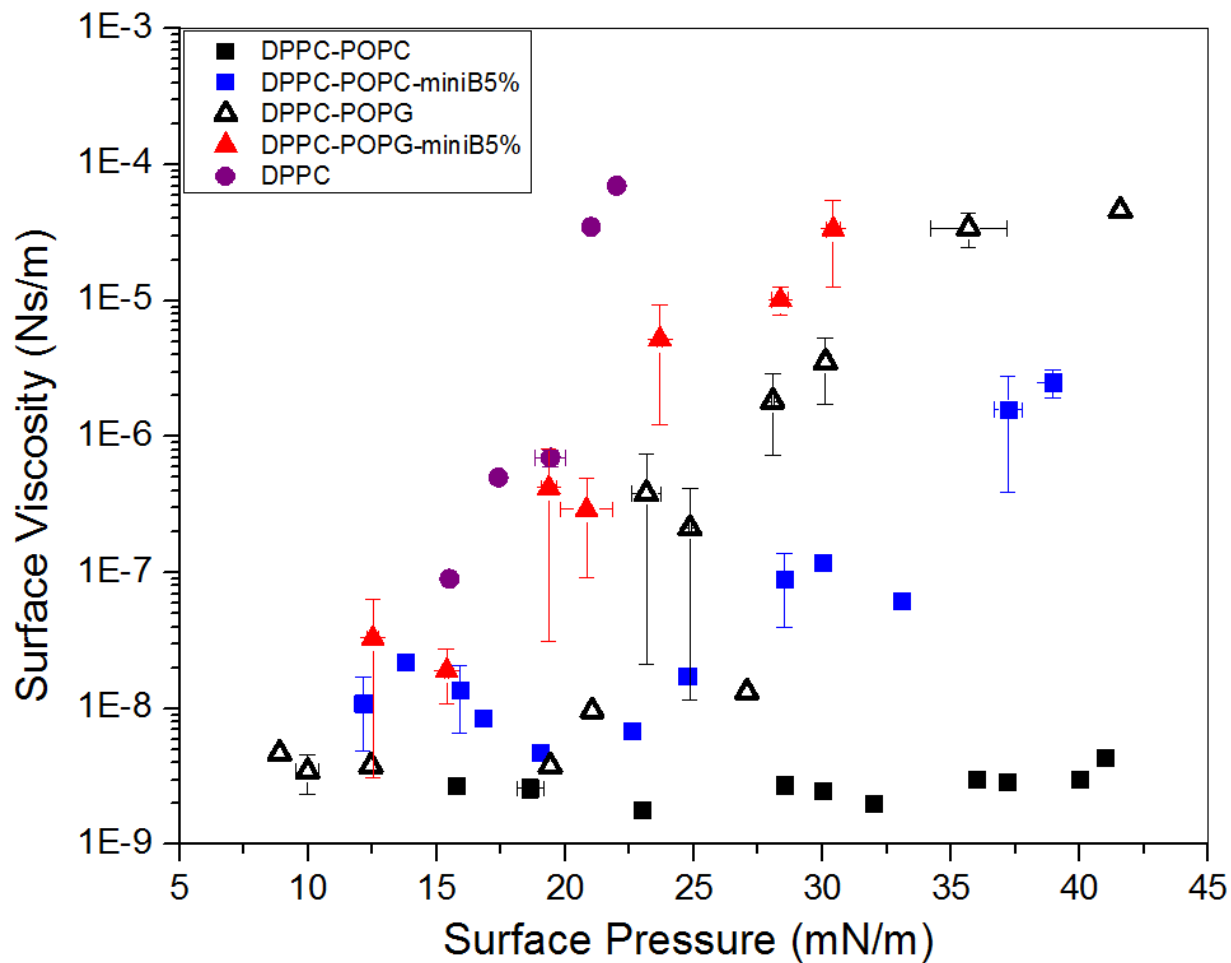
Figure 2. Surface viscosity of DPPC-POPC, DPPC-POPC-miniB (5 wt.%) , DPPC-POPG and DPPC-POPG-miniB (5 wt.%) measured with nanorods using active micro-rheology.

The ratio between DPPC and POPC is similar to DPPC and POPG that is 7:3.
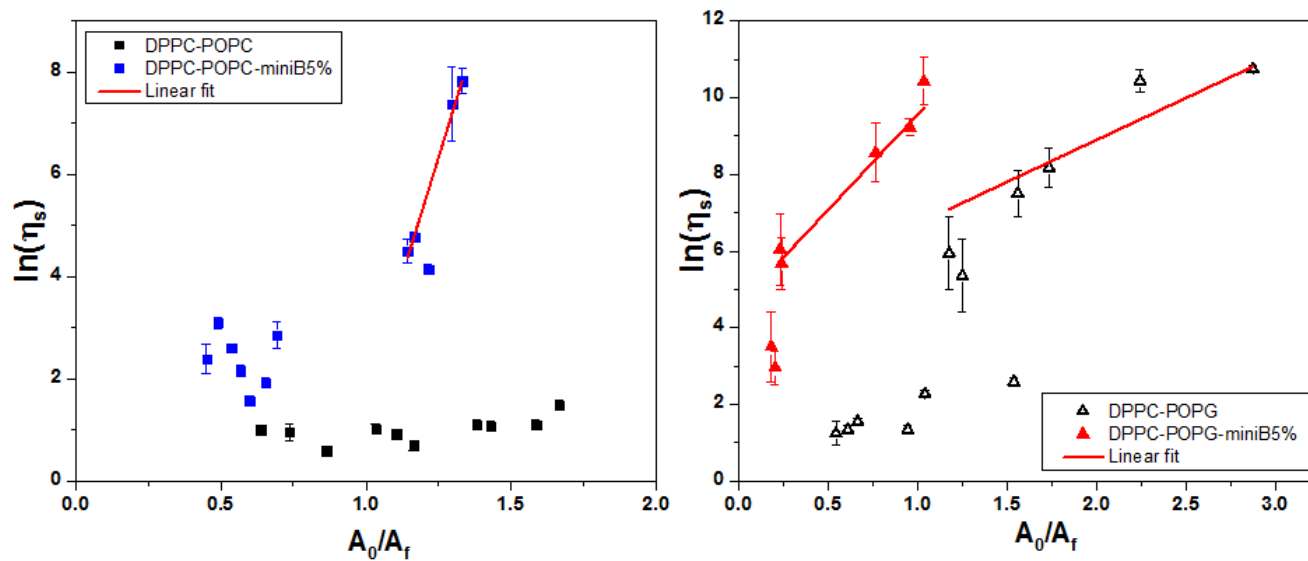
Figure 3. Natural logarithm of surface viscosity vs. the ratio of the close-packed A_0 to free area A_f for DPPC-POPC, DPPC-POPC-miniB, DPPC-POPG, and DPPC-POPG-miniB monolayers.

4.5. References

1. Notter, R.H., *Lung surfactants: basic science and clinical applications*. 2000: CRC Press.
2. El-Gendy, N., et al., *Delivery and performance of surfactant replacement therapies to treat pulmonary disorders*. Therapeutic delivery, 2013. **4**(8): p. 951-980.
3. Rodriguez, R., R. Martin, and A. Fanaroff, *Respiratory distress syndrome and its management*. Fanaroff and Martin's Neonatal-Perinatal Medicine: Diseases of the Fetus and Infant. 7th ed. St. Louis, MO: Mosby, 2002: p. 1001-1011.
4. Takahashi, A., et al., *Structure-function relationships of bovine pulmonary surfactant proteins: SP-B and SP-C*. Biochimica et Biophysica Acta (BBA)-Lipids and Lipid Metabolism, 1990. **1044**(1): p. 43-49.
5. Bernhard, W., et al., *Commercial versus native surfactants: surface activity, molecular components, and the effect of calcium*. American Journal of Respiratory and Critical Care Medicine, 2000. **162**(4): p. 1524-1533.
6. Lhert, F., et al., *Effects of hydrophobic surfactant proteins on collapse of pulmonary surfactant monolayers*. Biophysical journal, 2007. **93**(12): p. 4237-4243.
7. Baoukina, S., et al., *The molecular mechanism of lipid monolayer collapse*. Proceedings of the National Academy of Sciences, 2008. **105**(31): p. 10803-10808.
8. Lee, K.Y.C., *Collapse mechanisms of Langmuir monolayers*. Annu. Rev. Phys. Chem., 2008. **59**: p. 771-791.
9. Pérez-Gil, J., *Structure of pulmonary surfactant membranes and films: the role of proteins and lipid–protein interactions*. Biochimica et Biophysica acta (BBA)-Biomembranes, 2008. **1778**(7): p. 1676-1695.
10. Zasadzinski, J., et al., *The physics and physiology of lung surfactants*. Current Opinion in Colloid & Interface Science, 2001. **6**(5): p. 506-513.
11. Ding, J., et al., *Effects of lung surfactant proteins, SP-B and SP-C, and palmitic acid on monolayer stability*. Biophysical Journal, 2001. **80**(5): p. 2262-2272.
12. Takamoto, D., et al., *Interaction of lung surfactant proteins with anionic phospholipids*. Biophysical journal, 2001. **81**(1): p. 153-169.
13. Bringezu, F., et al., *Influence of pulmonary surfactant protein B on model lung surfactant monolayers*. Langmuir, 2002. **18**(6): p. 2319-2325.
14. Yan, W., B. Piknova, and S.B. Hall, *The collapse of monolayers containing pulmonary surfactant phospholipids is kinetically determined*. Biophysical journal, 2005. **89**(1): p. 306-314.
15. Serrano, A.G. and J. Pérez-Gil, *Protein–lipid interactions and surface activity in the pulmonary surfactant system*. Chemistry and physics of lipids, 2006. **141**(1): p. 105-118.
16. Walther, F.J., et al., *Surfactant protein B and C analogues*. Molecular Genetics and Metabolism, 2000. **71**(1): p. 342-351.
17. Alonso, C., A. Waring, and J.A. Zasadzinski, *Keeping lung surfactant where it belongs: protein regulation of two-dimensional viscosity*. Biophysical journal, 2005. **89**(1): p. 266-273.
18. Saffman, P. and M. Delbrück, *Brownian motion in biological membranes*. Proceedings of the National Academy of Sciences, 1975. **72**(8): p. 3111-3113.
19. Brooks, C.F., et al., *An interfacial stress rheometer to study rheological transitions in monolayers at the air− water interface*. Langmuir, 1999. **15**(7): p. 2450-2459.
20. Dhar, P., et al., *Autonomously moving nanorods at a viscous interface*. Nano letters, 2006. **6**(1): p. 66-72.
21. Choi, S., et al., *Active microrheology and simultaneous visualization of sheared phospholipid monolayers*. Nature communications, 2011. **2**: p. 312.
22. Lee, M.H., et al., *Combined Passive and Active Microrheology Study of Protein-Layer Formation at an Air− Water Interface*. Langmuir, 2009. **26**(4): p. 2650-2658.
23. Fuller, G.G. and J. Vermant, *Complex fluid-fluid interfaces: rheology and structure*. Annual review of chemical and biomolecular engineering, 2012. **3**: p. 519-543.

24. Mendoza, A.J., et al., *Particle laden fluid interfaces: dynamics and interfacial rheology.* Advances in colloid and interface science, 2014. **206**: p. 303-319.

25. Samaniuk, J.R. and J. Vermant, *Micro and macrorheology at fluid–fluid interfaces.* Soft matter, 2014. **10**(36): p. 7023-7033.

26. Kim, K., et al., *Interfacial microrheology of DPPC monolayers at the air–water interface.* Soft Matter, 2011. **7**(17): p. 7782-7789.

27. Hermans, E. and J. Vermant, *Interfacial shear rheology of DPPC under physiologically relevant conditions.* Soft Matter, 2014. **10**(1): p. 175-186.

28. Ghazvini, S., et al., *Monitoring phases and phase transitions in phosphatidylethanolamine monolayers using active interfacial microrheology.* Soft matter, 2015. **11**(17): p. 3313-3321.

29. Sachan, A., et al., *Interfacial rheology of coexisting solid and fluid monolayers.* Soft Matter, 2017. **13**(7): p. 1481-1492.

30. Walther, F.J., et al., *Hydrophobic surfactant proteins and their analogues.* Neonatology, 2007. **91**(4): p. 303-310.

31. Walther, F.J., et al., *Critical structural and functional roles for the N-terminal insertion sequence in surfactant protein B analogs.* PLoS One, 2010. **5**(1): p. e8672.

32. Waring, A., et al., *The role of charged amphipathic helices in the structure and function of surfactant protein B.* The Journal of peptide research, 2005. **66**(6): p. 364-374.

33. Bechinger, B. and J. Seelig, *Interaction of electric dipoles with phospholipid head groups. A deuterium and phosphorus-31 NMR study of phloretin and phloretin analogs in phosphatidylcholine membranes.* Biochemistry, 1991. **30**(16): p. 3923-3929.

34. Doux, J.P., B.A. Hall, and J.A. Killian, *How Lipid Headgroups Sense the Membrane Environment: An Application of 14 N NMR.* Biophysical journal, 2012. **103**(6): p. 1245-1253.

35. Wang, B., et al., *Nanoparticle-induced surface reconstruction of phospholipid membranes.* Proceedings of the National Academy of Sciences, 2008. **105**(47): p. 18171-18175.

36. Helm, C., et al., *Phases of phosphatidyl ethanolamine monolayers studied by synchrotron x-ray scattering.* Biophysical journal, 1991. **60**(6): p. 1457.

37. Zasadzinski, J., et al., *Langmuir-blodgett films.* Science-AAAS-Weekly Paper Edition-including Guide to Scientific Information, 1994. **263**(5154): p. 1726-1738.

38. Simons, K. and D. Toomre, *Lipid rafts and signal transduction.* Nature reviews Molecular cell biology, 2000. **1**(1): p. 31-39.

39. Edidin, M., *The state of lipid rafts: from model membranes to cells.* Annual review of biophysics and biomolecular structure, 2003. **32**(1): p. 257-283.

Chapter 5: Evaluating the Role of the Air-Solution Interface on the Mechanism of Subvisible Particle Formation Caused by Mechanical Agitation for an IgG1 mAb

Published:

Saba Ghazvini [†1], Cavan Kalonia [†2], David B. Volkin [2], Prajnaparamita Dhar [3]

1. Bioengineering Graduate Program, University of Kansas, Lawrence, KS 66046
2. Department of Pharmaceutical Chemistry, Macromolecule and Vaccine Stabilization Center, University of Kansas, Lawrence, KS 66047
3. Department of Chemical and Petroleum Engineering, University of Kansas, Lawrence, KS 66046.

† These authors contributed equally to the paper as first authors.

Saba Ghazvini mainly contributed to the interfacial characterization studies.

Cavan Kalonia mainly contributed to the bulk characterization studies.

5.1. Introduction

Protein aggregation and particle formation is a commonly observed degradation pathway of therapeutic mAb drug products, and is a significant cause for concern due to potential adverse effects on product safety and efficacy, either through decreasing potency or by enhancing product immunogenicity [1, 2]. Larger protein aggregates, in the size range of >0.1 µm and <100 µm, often called submicron and subvisible protein particles, are widely considered to be important to monitor and control, since particle sizes within this range potentially possess the ability to enhance the efficiency of uptake by antigen presenting cells [3-8]. Characterization of such particles formed by exposure of protein solutions to different stresses (e.g., mechanical, chemical, and thermal) has shown that particles can vary in size, number and shape, as well as the degree of structural perturbation/chemical degradation of protein within the particles, leading to highly heterogeneous samples [9, 10] [11]. Preliminary studies attempting to purify fractions of particles based upon size suggest that protein particle immunogenicity potential may be size and concentration dependent as determined by *in vitro* cell-based models [5, 12]. As a result, the risk vs. benefit that these protein degradation products pose to patients has emerged as a major consideration during mAb drug formulation design and development [4, 13-15].

Successful development of protein formulations requires a thorough understanding of protein physical degradation pathways during exposure to different environmental stresses. Numerous studies have resulted in an improved mechanistic understanding of protein aggregation and particle formation in bulk protein solution from a pharmaceutical perspective [16-18]. Models describing protein aggregation and subsequent particle formation in bulk solution typically include nucleation, growth and condensation phases[19-21] and involve unfolding and/or association steps. As a result, protein candidates are often formulated to optimize conformational and colloidal

stability to reduce the rate of aggregation in bulk solution during manufacturing, transport and administration [22-24]. However, formulation conditions that stabilize some mAbs against aggregation and protein particle formation during thermal stress have been observed to be destabilizing during mechanical agitation[25]. Therefore, in addition to evaluating protein interaction mechanisms occurring in the bulk solution, it is also important to consider the air-solution interface as a source of instability for therapeutic protein products[26].

Several recent studies have provided evidence that disruption of a high concentration protein layer at air-solution interface can be responsible for producing protein particles in the bulk solution [27] [28] [29]. One of the most common ways to minimize interface induced aggregation of protein molecules has been the addition of nonionic surfactants such as polysorbate 20 or 80 or related surface active compounds[30, 31]. Competitive adsorption between the smaller surfactant molecules and the larger protein molecules has been shown to minimize adsorption of the proteins to the air-water interface, thereby reducing protein particle formation at the interface[32]. However, polysorbate-based excipients are themselves prone to physicochemical degradation and in some cases may even accelerate the aggregation of certain proteins [33]. Other formulation variables such as pH, ionic strength, and poly valent ions have been shown to have a large effect on protein instability during agitation and can impact protein-protein interactions at the air-water interface [34] [35]. Therefore, developing a better understanding of how mAb formulation conditions affect air-solution interface mediated particle formation is critical to ultimately reduce the reliance on nonionic surfactant alone to provide stability against agitation induced protein particle formation.

In this work, we seek to further elucidate the mechanism of particle formation initiated at the air-solution interface during mechanical agitation, and to better understand the effect of

solution pH and buffer ion type on this aggregation pathway, for a model IgG1 mAb. A Langmuir trough is used to model pharmaceutical instability resulting from mechanical agitation of different formulations of the IgG1 mAb, where controlled compression/dilation cycles ensure that mechanical stresses are applied only to a protein film formed at the air-water interface. Analysis of protein particles formed in the bulk solution after compression/dilation cycles are correlated with high resolution atomic microscopy images of protein films at the interface, to better understand how protein aggregates at the air-solution interface effect the amount of particles present in the bulk solution. In addition, we evaluate the role of formulation conditions on extent of particle formation for this IgG1 mAb at the air-solution interface, with and without mechanical stress, and correlate our results with surface pressure measurements.

5.2.   Experimental procedures
5.2.1. Materials and Sample Preparation

The IgG1 mAb (pI range around ~ 9) used in this study was provided by Janssen Research & Development, LLC (Horsham, Pennsylvania) at a concentration of ~40 mg/ml. Stock buffers of 50 mM citrate and 50 mM histidine were prepared at pH 4.5 and 6.5. The L-histidine was purchased from Sigma-Aldrich (St. Louis, Missouri) and the sodium citrate dihydrate and citric acid anhydrous were purchased from Fisher Scientific (Hampton, New Hampshire). Additionally, 1x phosphate buffered saline (PBS) buffer (Fisher Scientific, Hampton, New Hampshire) was prepared at pH 7.4 according to the manufacturer's recipe, and a second preparation of 1x PBS buffer was titrated using hydrochloric acid to a pH of ~4.5. All stock buffers were prepared using Milli-Q water (EMD Millipore, Billerica, Massachusetts) and sterile filtered using a 0.2 μm filter.

Mechanical Agitation Studies

The mAb solution was diluted 1:40x into each of the stock buffers to generate working mAb solutions of 1.0 mg/ml. The working mAb solutions were gently inverted and allowed to sit for half an hour to ensure proper mixing. Three ml aliquots of each working solution were pipetted into 37.7×16.75 mm glass vials (Schott, Lebanon, Pennsylvania) and capped with uncoated rubber stoppers (West Pharmaceutical Services, Exton, Pennsylvania). The mAb solutions were agitated using a HS 260 shaker (IKA Works, Inc., Wilmington, North Carolina) at 300 cycles/minute as described previously [11]. The aliquots for each formulation condition were agitated for 0, 1 or 3 days (N=3 for each time point).

Interfacial Compression-Expansion Studies

Working IgG1 mAb solutions at 0.37mg/ml were prepared by adding 370 µl of mAb stock solution to 40 ml of buffer (PBS, histidine, or citrate). Working solutions were loaded into a Langmuir trough that was controlled at 23 ± 2°C (Biolin Scientific Inc., Stockholm, Sweden). A Wilhelmy plate was used to measure surface pressure during adsorption and compression-expansion experiments. The compression-expansion cycles began after a 2hr period for adsorption to become saturated. The available interfacial area changed from 87 to 12 cm^2 during each compression-expansion cycle by moving the barriers of the Langmuir trough. The compression ratio, defined as the ratio of the maximum possible area and the minimum area of the trough (CR=A_{max}/A_{min}), was held constant at 7.25 for this study. For mAb samples prepared in 1x PBS, the "slow" compression-expansion rate was 50 cycles/6 hours and the "fast" compression-expansion rate was 750 cycles/6 hours. For the mAb samples prepared in histidine or citrate buffers, the "slow" compression-expansion rate was 50 cycles/6 hours and the "fast" compression-expansion rate was 1000 cycles/6 hours.

5.2.2. Methods

Size-Exclusion HPLC

A Prominence UFLC HPLC (Shimadzu, Kyoto, Japan) with a diode array detector was used with a TSKgel G3000SWx1 stainless steel column (Tosoh Biosciences, San Francisco, California) and TSKgel SWxI guard column for size exclusion chromatography. The column was operated at 30°C and separation was achieved at a flow rate of 0.7 ml/min. The areas of the stressed sample chromatograms were normalized to the total area of the unstressed sample chromatograms to detect a loss of total area. A pH 6.8, 0.2 M phosphate buffer was selected as the mobile phase because the buffer has been shown to minimize protein adsorption to the column [36].

Flow Microscopy

A FlowCam VS Series (Fluid Imaging Technologies, Scarborough, Maine) benchtop flow microscope was used to count and characterize particles ≥ 1 μm but ≤ 100 μm in area based diameter (ABD). A 10x objective was used with a 100 μm x 2 mm flow cell. The sample volume analyzed was 0.5 ml, the flow rate was 0.15 ml/min, and the capture speed was set at 21 frames per second. Prior to measurement, the instrument was focused using NIST traceable 25 μm Duke Standards (Thermo Fisher Scientific, Waltham, Massachusetts).

Atomic force microscopy (AFM)

Freshly cleaved mica (Ted pella Inc., Redding, CA) was used as a support to obtain high resolution images of IgG1 mAb particles isolated from the air-solution interface and the bulk solution. Transferring the IgG1 mAb particles from interface was done by briefly contacting the mica to the air-solution interface. Mica sheets containing mAb particles from the bulk solution

were prepared by placing the freshly cleaved mica sheet at the bottom of the trough prior to compression-expansion cycles and collected afterwards. Once collected, the mica sheet for the mAb samples in citrate/histidine were immediately washed with Milli-Q water and dried with compressed air at $23 \pm 2\,^{\circ}C$. The mica sheets for the mAb samples in 1x PBS were also washed with pH 7.0 acetate buffer prior to drying. The AFM setup used was a Veeco MultiMode V (Veeco Instruments Inc., Plainview, NY). All AFM measurements were performed in a tapping mode using silicon probes (TAP150 Bruker) with a spring constant of $5\ Nm^{-1}$ at 150 kHz. Height analysis of the AFM images was done using Research NanoScope v7.30 (Veeco Instruments Inc., Plainview, NY). Imaging was done in a temperature controlled room maintained at $20\,^{\circ}C$. To evaluate the height of mAb particles analyzed by AFM, 3 images were collected from each mica sheet prepared during Langmuir trough experiments (N=3 for each sample condition). The combined data points for each condition were plotted as box plots.

5.3. Results

To better understand how protein particle formation is occurring at the air-solution interface during mechanical agitation, a Langmuir trough experimental setup was used where an IgG1 mAb solution is exposed to controlled compression/dilation cycles resulting in mechanical stresses applied only at the air-water interface, and not in the bulk protein solution. These results are then compared to agitation of the same mAb solution filled into glass vials. Figure 1 provides an overview of the experimental setup and the Langmuir trough instrument. In both cases, changes in interfacial area available are hypothesized to disrupt the adsorbed mAb layer at the air-solution interface and potentially result in the release of particles into the bulk solution as shown schematically in Figure 1.

Correlating Protein Particle Formation Due to Controlled Changes to Available Interfacial Area to Particle Formation During Mechanical Agitation of mAb Solutions

Particle Formation in the Bulk Solution During Mechanical Agitation in PBS Buffer

First, unstressed mAb samples (0 day), formulated in pH 4.5 or pH 7.4 PBS buffer, were analyzed for levels of protein subvisible particles by flow microscopy and were found to contain >300 subvisible particles/mL with most particles in the 2-5 μm and 5-10 μm particle size range (Figure 2, bottom panel). After 3 days of side-to-side shaking in glass vials, however, both mAb samples showed a large, significant increase in particles in the bulk solution, with the mAbs samples at pH 4.5 containing more particles compared to the mAb samples at pH 7.4 (Figure 2, top panel). Moreover, particles formed in the agitated mAb sample at pH 4.5 were distributed across the size ranges analyzed. The particle size distribution is shown on a logarithmic scale in Figure 2 and can be visualized from the shape of the polygon signal of the radar chart. The average number of particles per ml in the pH 4.5 mAb samples was greater than 100,000 for particles 2-5 μm, ~100,000 for particles 5-10 μm, and ~10,000 for particles ranging in size from 10-15, 15-25, 25-40, 40-50, and 50-100 μm. The mAb sample at pH 7.4, on the other hand, did not have significant particle formation for sizes greater than 25 μm as compared to the unstressed sample (Figure 2, top right panel). The average number of particles per ml in the pH 7.4 mAb samples was less than 10,000 for particles ranging from 2-5 μm and 5-10 μm, and less than 1,000 for particles ranging from 10-15 μm and 15-25 μm.

The unstressed and mechanically agitated (at 1 and 3 days) mAb samples in PBS buffer were also analyzed using size exclusion chromatography (SEC). The mAb sample at pH 4.5 had ~1.0 ± 0.3 % monomer loss (N=3) whereas the mAb sample at pH 7.4 did not have significant

monomer loss over the 3 days of agitation. Additionally, no high molecular weight species (HMWS) or mAb fragments were observed by SEC (see supplemental Figures S1 and S2 for representative chromatograms and SEC stability data).

Surface Properties of mAb Samples in PBS Buffer

As a next step, we then established techniques to correlate these observed differences in particle formation with differences in the interfacial properties of these mAb samples, in the absence and presence of applied stress to the interface. As shown in Figure 3A, the surface pressure-area (Π-A) isotherm of mAb solutions in PBS buffer at pH 7.4 was subjected to slow compression-expansion cycles. Theoretically, the measured surface pressure corresponds to possible adsorption and rearrangement of mAb molecules at the interface[28, 37]. Upon decreasing the interfacial area, the surface pressure increases (or the surface tension) decreases non-linearly. Interfacial area expansion after a compression cycle resulted in an abrupt decrease in the surface pressure causing a visible hysteresis pattern. The surface pressure at the beginning of first cycle corresponds to the equilibrium saturation value that was reached after the proteins were allowed to adsorb to the interface and equilibrate for two hours. This saturation value was not reached during compression-expansion cycles, because the proteins did not have enough time to reach their equilibrium value during continuous compression-expansion cycles. The maximum surface pressure at minimum interfacial area was also found to be the maximum for the first cycle and decreased steadily over the 50 cycles reported here. Supplementary figure S3 shows negligible increase of surface pressure with time for protein-free polysorbate samples at 0.00012 wt% (corresponds to the concentration of polysorbate in the mAb solutions being studied)during adsorption studies. Similarly, Π-A isotherm studies show that the polysorbate solution itself is

compressible further establishing that the increase in measured surface pressure may be attributed to the presence of mAb proteins at the air-solution interface.

Figure 3B presents the first and last cycle for compression-expansion isotherms plotted for mAb solutions in PBS buffer at both pH 4.5 and pH 7.4. The hysteresis was found to be greater in the first cycle compared to the last cycle for both sample conditions. The first (blue and red) and last (black and pink) cycles in the surface pressure vs. area isotherms overlapped with no statistically significant difference for the two conditions (Figure 3B). Additionally, the initial and final surface pressures were higher for the first cycle compared to the last cycle for both sample conditions. Figure 3C presents the average area under the isotherm curves for the first and last cycle of mAb samples in PBS buffer at pH 4.5 and 7.4, used as a measure of the total hysteresis in these protein films. The average value (N=3) of the total area under the curve for the first cycle was higher than that for the last cycle but the difference was not statistically significant. To investigate the effect of time of exposure of mAb samples to the air-solution interface during compression-expansion cycles, we compared 50 cycles of slow (6 hours) and fast (25 min) rate (see supplemental figure S3 panel C and D). To further investigate how the rate of the compression influenced the compression-expansion isotherms, we compared the surface pressure vs area isotherms for the 1st and 50th cycles corresponding to compression for 6 hours or 25 minutes (fast). While no difference seen for the first cycles, the 50th cycle shows more hysteresis.

The Effect of Compression Rate on Particle Formation at the Air-Protein Solution Interface and in Bulk Solution

The number and size distribution of subvisible sized protein particles in the bulk solution, as measured by flow digital imaging, for mAb samples at pH 4.5 and pH 7.4 after being subjected to slow (A) or fast (B) compression-expansion cycles during 6 hours in the Langmuir trough, are shown in Figures 4A and 4B, respectively. The same mAb solutions that were not subjected to the compression/dilatational stresses, but for which all other environment conditions were kept identical (temperature, time of incubation, formulation pH) were used as control samples (Figure 4, Panel A/B, red signal). Results show no statistically significant differences between the number and size distribution of particles in the bulk mAb samples subjected to the slow compression-expansion rate when compared to the corresponding control samples. Moreover, the control mAb samples at both pH conditions had similar numbers of particles detected in the bulk solution. In contrast, mAb protein solutions that were subjected to fast interfacial compressive stresses for 6 hours, demonstrated more than an order of magnitude increase in the number of protein subvisible particles detected in the bulk solution. Further, the stressed mAb samples at pH 4.5 were found to contain a broader size range of particles (up to 50 µm), when compared with mAb samples at pH 7.4.

Representative atomic force microscopy (AFM) images of mAb particle formation at the interface and in the bulk mAb solution, for both stressed mAb samples in PBS buffer at the two pHs, are presented in Figure 4, panel C and D. For the slow compression-expansion rate (Panel C), the protein films transferred from the air-water interface contained greater number of protein aggregates compared with mica surfaces placed in the bulk mAb solution, irrespective of the solution pH. In contrast, mica sheets placed in bulk mAb solutions that were subjected to fast compression expansion cycles (Panel D), contained greater number of micron and sub-micron protein aggregates when compared with films transferred from the air-solution interface.

Additionally, the mAb pH 4.5 solutions, after being subjected to fast compression-expansion cycles, contained more particles at the interface and in the bulk solution, when compared to the pH 7.4 mAb solutions. Supplementary figure S4 also shows that the total time of compression, or number of total compression-expansion cycles, plays an important role. Keeping the total number of cycles constant, but applying stress at different rates (slow vs fast), we find that the total number and size distribution of mAb particles is not different both at bulk solution (figure S4 panel A,B) and at the interface (figure S4 panel C, D).

In panels E and F of figure 4, box plots displaying the height (median and range) of mAb particles as measured by AFM are presented to quantitatively compare the AFM images (N=9 for each condition). For the slow compression-expansion rate (Panel E), the box plot of the height of protein particles at the interface of the pH 4.5 mAb sample had a higher median value than the box plot of the interface for the mAb sample at pH 7.4. For the bulk mAb solutions, the range of protein particle height data is much smaller compared to the range of particle height results at the interface. It should be pointed out that areas that did not contain any particles or a lesser number of particles were included in the analysis thereby exacerbating the apparent standard deviations shown in Figure 4E and 4F. For the mAb samples exposed to fast compression-expansion rate (Figure 4, Panel F), AFM results had similar median values for the height of mAb particles at the interface compared to the mAb samples exposed to low compression-expansion at both pH 4.5 and 7.4 conditions. Furthermore, the median value and the range of the particle height data from AFM for particles in bulk solution were similar between the fast and slow compression rates for the pH 7.4 mAb samples. However, the median and range of height data from AFM analysis of particles in bulk solution increased significantly for mAb pH 4.5 samples that were subjected to fast compression.

Qualitative Comparison of the Morphology of mAb Particles Formed During Mechanical

Agitation vs. Interfacial Compression-Expansion

To further compare and characterize the protein particles formed during compression-expansion cycles in the Langmuir trough vs. particles formed during agitation in vials, particle morphology data from flow microscopy digital images were analyzed. Circularity (Hu), a measure of particle perimeter relative to a circle of equivalent area, and aspect ratio, a measure of elongation, were evaluated for particles formed by the two stresses and compared to theoretical values for prolate ellipsoids with varying aspect ratios (Figure 5)[38]. The solid blue curve is a calculation, described previously from Kalonia et al. 2015, that determines the circularity of theoretical prolate ellipses based on the aspect ratio and is meant to be used as a reference point for characterizing particle morphology as described previously[39]. For example, at the coordinate (1 , 1) in Figure 5, the blue curve represents a perfectly circular particle. As the aspect ratio decreases, particle elongation increases and positive deviations from the curve represent the particle having a larger perimeter than an ellipse of equal aspect ratio (typically indicating an increase in surface roughness/fractal dimension). The subvisible sized protein particles detected in the mAb sample subjected to fast compression-expansion were ellipse-like (circularity and aspect ratios close to the theoretical ellipse curve) and ranged from 1x elongation to 3x elongation relative to a circular particle of equal area (Figure 5, Panel A). Protein particles generated by side-to-side agitation of the same mAb solution, on the other hand, were more elongated on average (up to 20x relative to a circular particle of equal area) and were not as ellipse-like as they showed positive deviations from the theoretical ellipse curve (Figure 5, Panel B) as compared to the same mAb sample exposed to compression in the Langmuir trough (see supplemental figure S5).

Several representative protein particle images from flow microscopy analysis are presented in Figure 5C for a mAb sample subjected to fast compression-expansion in the Langmuir trough. The protein particles appear to be compact and circular/ellipse-like, consistent with results as seen in the corresponding morphology scatter plot (Figure 5A). On the other hand, the representative images of protein particles detected in the side-to-side agitated mAb samples (Figure 5, Panel D) appear to be loose, tenuous structures with rough perimeters. The images of the protein particles caused by agitation of the mAb solution in vials are also consistent with scatter plot data which showed positive deviations from the theoretical ellipse curve (Figure 5B). Additionally we compared overall secondary structure of the mAb particles ,formed during fast compression, using solution FTIR and FTIR microscopy (see supplemental figure S6). Comparing interfacial stress-induced mAb particles with control and denatured (by heat) mAb samples, a slight shift in second-derivative FTIR spectra is monitored in two peaks for intramolecular beta-sheet content (occurring between 1620-1640 and 1690-1700 cm^{-1}) (N=3) (figure S6).

The Effect of pH and Buffer Composition of mAb Solutions on the Properties of the Protein Films Formed at the Air-Solution Interface

Analysis of the surface activity and surface pressure vs. area isotherms for mAb Samples in Histidine or Citrate Buffer

The previous section presented data for an IgG1 mAb in PBS buffer at two different pH values. As a next step, the effect of histidine and citrate buffers on the aggregation propensity of the same IgG1 mAb was examined. The surface pressure-area (Π-A) isotherm of mAb solutions in citrate buffer at pH 6.5 subjected to dilation cycles at a slow compression-expansion rate as shown in Figure 6A. Similar to mAb formulated in PBS buffer, the initial surface pressure value

corresponds to the value of the saturated surface pressure after 2 hours of adsorption. The initial and final surface pressures at the minimum and maximum interfacial area during compression-expansion cycles decreased over the 50 cycles.

Figure 6, Panel B shows the surface pressure change with change in interfacial area during the first and last (50th) cycles for pH 4.5 and 6.5 mAb samples formulated in citrate buffer. Obvious changes in the shape of the curves as well as the values of the surface pressure were recorded in these samples. The mAb solution in citrate buffer at pH 4.5 demonstrated the maximum protein film compressibility (maximum change in surface pressure with changes in the trough area), while the mAb formulated citrate buffer at pH 6.5 showed protein films at the air-water interface were the least compressible films. Further, for each of the excipient solutions, the lower pH solutions demonstrated increased protein film compressibility at the air-solution interface.

Figure 6, Panel C presents a quantitative comparison of the average area (N=3) within the surface pressure vs. area curves during the first and last compression-expansion cycles for mAb samples at pH 4.5 and 6.5 in histidine or citrate buffers. Such measurements represent differences in the hysteresis present in the mAb protein films. The difference between the hysteresis of the first and last compression-expansion cycle was significant for all conditions assessed (p<0.005). In addition, the area under the curve for the first compression-expansion cycle for mAb samples was larger when formulated in buffers at pH 4.5 than at pH 6.5, regardless of the buffer ion type (citrate vs. histidine). Most notably, the area under the isotherms for mAb samples in citrate buffer at pH 4.5 is significantly higher than all the other conditions studied (p<0.05). A summary of the statistical analysis of the differences in these areas is presented in Figure 6, Panel D.

The Effect of pH and Buffer Composition of mAb solution on Particle Formation at the Air-Solution Interface for the Slow Compression Rate

To further explore the interfacial mAb particle formation process, topographical AFM images of protein films transferred from the air-solution interface were recorded. Representative images are presented in Figure 7 (top panel). Control mAb samples were incubated at room temperature without the application of interfacial stress. Irrespective of the buffer composition and pH of the mAb samples, the extent of protein aggregates formed at the air-solution interface (represented with lighter colors) was greater after being subjected to compression–expansion cycles, compared to their corresponding control samples. Additionally, several raised/aggregated features in the AFM images were recorded for proteins at the air-solution interface of compressed mAb samples in citrate buffer compared to histidine, irrespective of the solution pH.

Figure 7 (bottom panel) presents a box plot analysis of the height (median and range) of AFM images of mAb particles formed in histidine and citrate buffers at pH 4.5 and 6.5. Comparing the protein particles of control mAb samples there was no significant increase in particle height within the formulation by changing the pH (comparing AFM images A with C as well as E with G). However, when comparing the AFM images of the protein particle formed at the interface of compressed mAb samples, by decreasing the solution pH, the median value of protein particle height from the AFM images increases for mAb samples in both histidine and citrate (comparing AFM images B with D as well as F with H). Compressed mAb samples in citrate buffer at air-solution interface had higher median value and range of particle height compared to mAb solution in histidine buffer (AFM images F and H compared to B and D).

The Effect of pH and Buffer Composition of mAb Solution on Particle Number/Size Distribution in Bulk Solution After Compression-Expansion or Agitation

An analysis of particle formation in the bulk mAb solutions filled in glass vials, before and after 3 days of side-to-side agitation, showed that all four of the mAb samples had substantial particle formation in the bulk, when compared to the unstressed (0 day) control (Figure 8, top panel). The mAb solution in citrate buffer at pH 4.5 formed the most subvisible particles as compared to the other three mAb samples (pH 4.5 and 6.5 in histidine buffer and pH 6.5 in citrate buffer). After agitation, the mAb sample in citrate buffer at pH 4.5 had over 100,000 particles per ml from 2-5 μm, ~100,000 particles in each size range from 5-10 μm and 10-15 μm, and ~10,000 particles in each size range from 15-25, 25-40, 40-50, and 50-100 μm. On the other hand, the amount and size distribution of particles in the agitated mAb samples in histidine buffer at pH 4.5 and 6.5, as well as the agitated mAb samples in citrate buffer pH 6.5, were comparable and contained ~10,000 particles per ml from 2-5 μm, ~1,000 particles/ml in each range from 5-10, 10-15, and 15-25 μm, and less than 1,000 particles/ml in each of the larger size ranges. Additionally, the unstressed and mechanically agitated (at 1 and 3 days) mAb samples in citrate and histidine buffer were also analyzed using size exclusion chromatography (SEC) (see supplemental figure S6). The mAb sample in citrate buffer at pH 4.5 had ~2.0 ± 0.7 % monomer loss (N=3) whereas the mAb samples at pH 6.5 in citrate buffer and histidine buffer (both pH values) did not have significant monomer loss over the 3 days of agitation.

In addition to agitation in vials, mAb samples formulated in the same buffer conditions were subjected to controlled fast or slow compression-expansion rates in the Langmuir trough (see Experimental Procedures). Particle numbers were evaluated for the above conditions (Figure 8, bottom panel, black signals) and for a control where the same sample mAb formulations were

incubated at room temperature for the same amount of time. Similar to results described above with the mAb samples in the PBS buffer, slow compression of the same mAb in the histidine and citrate buffers did not result in a statistically significant difference in the number of particles in bulk solution as compared to the control samples. On the other hand, the fast compression-expansion caused significant increases in levels of particle observed versus the control samples for all four mAb samples. Interestingly, the mAb samples in histidine buffer at pH 4.5 and 6.5, as well as mAb in citrate buffer at pH 6.5, had similar levels of particles after fast compression. The mAb sample in citrate buffer at pH 4.5 generated the greatest number of subvisible particles as well as larger sized particles compared to the other mAb sample conditions subjected to fast compression. After the fast compression-expansion cycles, the mAb sample in citrate buffer at pH 4.5 had over 10,000 particles per ml from 2-5 μm, ~10,000 particles in each size range from 5-10 μm and 10-15 μm, and 15-25 μm, and ~1,000 particles in each range from 25-40, 40-50, and 50-100 μm (Figure 8, bottom panel, black signal).

5.4. Discussion

The primary focus of this work was to elucidate the correlation between interfacial stress induced protein clustering at air-water interfaces and mechanical agitation induced protein particle formation in bulk mAb solutions. Specifically, a Langmuir trough was used to induce controlled dilatational stress to protein films at the air-water interface, while high resolution imaging techniques were used to characterize, in more detail, protein particles formed at the interface (by AFM), and in the bulk solution (by flow digital imaging). Using Langmuir troughs to apply a compression/dilatation stress to mAb protein films at the air-water interface was recently described by Bee *et al.*, to mimic changes in available surface area during agitation[27]. TheLangmuir trough ensures that only protein molecules at the interface, and not the bulk solution, are subjected to

controlled stresses. This isolation of the bulk and interfacial stresses allowed for correlations to be developed between formation of protein particles in these two different environments with our model IgG1 mAb (see Figure 1 for a schematic of proposed correlation). In this work, we also explored how changes in the bulk mAb solution conditions and formulation composition contributed to differences in the formation and morphology of protein aggregates at the air-solution interface. Based on our results, we conclude that while interfacial stress initiates protein aggregation at the air-solution interface, the presence of protein particles in the bulk mAb solution formed as a result of mechanical agitation is only correlated with mAb solutions subjected to "fast" compression/dilatation cycles over an equal length of time. Further, both the solution pH and buffer composition control the morphology and size distribution of protein particles formed at the interface and in the bulk solution for this IgG1 mAb. These conclusions are discussed in more detail below.

Based on a combination of light scattering and calorimetry characterization studies (data not shown), the four selected solution conditions (citrate and histidine buffer at pH 4.5 and 6.5) result in a range of conformational and colloidal stability values for this IgG1 mAb. The lack of correlation between the mAb's biophysical parameters under these conditions (such as normalized second virial coefficient data from static light scattering and the apparent thermal onset and melting temperature obtained from DSC) and protein particle formation during agitation will be described in an companion manuscript (Kalonia et al, manuscript in preparation). Since mAb samples in histidine and citrate buffer at pH 4.5 and 6.5 are representative of a range of physical stability properties in the bulk solution, differences in protein-protein interactions at the air-water interface, and not conformational and colloidal stability, better predict the physical stability of mAb samples subjected to the mechanical stresses (Kalonia et al, manuscript in preparation). In this paper we

describe methodologies to thoroughly characterize the protein films formed at the air-water interface (e.g., Langmuir trough data and atomic force microscopy analysis) with this IgG1 mAb in PBS buffer (pH 4.5 and 7.4), in the absence and presence of interfacial stress, to better correlate the observed changes in particle formation in bulk mAb solutions to differences in interfacial protein film properties. We then not only examine the effect of solution pH and buffer ion types (histidine and citrate buffers at pH 4.5 and 6.5) on the propensity of this IgG1 mAb to form aggregates and particles at the interface and in bulk solution, but also evaluate their effects on the resulting protein particle number, size and morphology.

Analysis of surface pressure changes during compression-expansion cycles: As a first step towards analyzing interfacial phenomenon in various solutions of this gG1 mAb, we measured the surface activity of the protein films in a Langmuir trough experimental setup (Figure 1). The equilibrium surface pressure measurements show that even at a concentration of 0.37 mg/ml, the IgG1 mAb samples were surface active when formulated in different buffers and pH values. These results suggest that surface pressure measurements alone do not correlate with protein particle formation. Shieh *et al.* have recently shown, in fact, that equilibrium surface pressure values were not an adequate predictor of a different mAb sample's susceptibility to aggregate[28]. Instead, the kinetics of antibody rearrangement after adsorbing to the interface was shown to be better correlated with the extent of observed aggregation[28]. In this work, we present a comparison of how differences in the application of surface stresses, as well as protein solution composition, influence protein particle formation in the bulk solution. Particularly, surface pressure vs. area isotherms during the compression-expansion cycles were recorded and analyzed in detail to determine evidence of strong attractive antibody-antibody interactions that may result from mechanical agitation or stresses. Specifically, we compared the difference between the hysteresis

of the first and last cycle of surface pressure vs. area isotherms that could potentially indicate the extent of particle loss from the interface. The isotherms indicate the formation of an incompressible film at the interface while the hysteresis indicates the likely possibility of formation of irreversible protein associations during a compression-expansion cycle. Further, mAb samples in citrate buffer at pH 4.5 were found to possess the largest difference in hysteresis between first and last cycles, suggesting the most associations between the proteins at the air-water interface in this solution. Our supplementary data (figure S3) also conclusively established that the observed phenomena is due to protein-protein interactions, and not due to the presence of surfactant (polysorbate).

Analysis of protein particles formed at the air-water interface or in bulk solution: The analysis of the interfacial properties of the protein films were complemented with high resolution AFM imaging of protein aggregates. Our AFM images confirmed the formation of protein aggregates at the air-water interface in mAb samples that were mechanically stressed in the Langmuir trough. The lack of any notable raised features in the AFM images of mAb samples not subjected to mechanical stresses confirmed that application of interfacial stresses was the key to protein aggregate formation at the air-protein solution interface. It was also interesting to note that protein films transferred from mAb solutions in citrate buffer at pH 4.5 produced the maximum number of protein aggregates, particularly fold-like fibrils, that resemble collapsed protein, polymer or lipid films at air-water interfaces, when they are subjected to very high compression[40, 41] . Therefore, both the presence of compressive stresses, as well as different bulk mAb solution composition (pH and buffer ion type) contribute to the protein aggregate formation at the air-solution interface.

Differences in the formation of protein particles in bulk solution, as measured by radar chart analysis of digital flow imaging data, for the slow and fast compressions, together with the AFM images of the protein aggregates at the interface and bulk solution for slow and fast compressions, establish that in addition to being subjected to interfacial stresses, the protein particles can be lost from the interface into the bulk and serve as nucleation points only if the interface is sufficiently perturbed. When the number of cycles was kept constant at 50, but the stress was applied for different amounts of time, no difference is observed in the formation of mAb particles, at the interface or in the bulk, further stablishing the need for extensive perturbation of the interface. Additionally, hysteresis in the protein films corresponds well with presence of protein particles in bulk protein samples. For example, not only did the mAb sample in citrate buffer at pH 4.5 have the largest difference in hysteresis, suggesting the highest protein-protein associations, the bulk mAb solution for this formulation also had the highest particle formation among mechanically agitated samples (see Figure 8). These observations, along with the direct visual evidence of protein aggregates at mechanically stressed air-protein solution interfaces, further establish that while mechanical agitation to the interfacial protein film alone is sufficient to cause protein particle formation, even in relatively dilute solutions of this IgG1 mAb, continuous and aggressive disruption of the interfacial film is also necessary for more extensive protein particle formation in the bulk mAb solution.

Further analysis of the high resolution AFM images of the protein films transferred from the air-water interface suggest that protein particles present at air-water interface of mAb samples formulated in citrate buffer were more fibril-like compared to protein particles present in mAb samples in PBS buffer and larger compared to fibrils formed in mAb samples in histidine buffer (see Fig. 4 and 7). Interestingly, similar fibril/filament morphology of protein particles with a

different mAb in citrate buffer has been reported using other techniques such as electron scanning imaging [42, 43]. Interestingly, subvisible particle images of our model IgG1 mAb particles in bulk solution, using flow digital imaging measurements, showed similar fibril morphology for mAb samples in citrate buffer, which further suggests the possibility of detachment of mAb particles from the interface to the bulk solution. Additionally, the compact morphology of mAb particles formed as a result of interfacial stresses compared to those formed by agitation of the same mAb samples in glass vials (Figure 5) suggests that the larger compression ratio of the Langmuir trough compared to vials possibly influences the morphology of the observed protein particles in these mAb samples. Differences in the rate and nature of interfacial perturbation between shaking and interfacial compression-expansion cycles could also be responsible for the different particle morphologies observed. Protein molecules that associate rapidly tend to form loose, tenuous aggregate structures whereas molecules that associate slowly have more time to reorient and tend to form more compact aggregates[44].

Impact of buffer ion and pH conditions of mAb samples on protein particle formation: To better explain the observed differences in the morphology and number of protein particles formed at the air-solution interface, we turn our attention to protein-protein interactions observed in highly concentrated bulk protein solutions. Although one might argue that the bulk protein solution in our studies is very dilute, the two-dimensional air-water interface is in fact highly concentrated, because of the saturation of this interface with protein molecules. Literature survey of highly concentrated mAb protein solution suggests that increased protein-protein interactions in highly concentrated mAb solutions can in fact be correlated with bulk viscosity measurements at high protein concentrations [42, 43, 45-47]. For example, Esue *et al.* reported on the appearance of large bulk elasticity for a mAb solution in citrate buffer at a mAb concentration

higher than 25 mg/ml at pH 6.0. The elastic modulus of the protein solution was not affected by ion strength of the formulation but concentration of carboxylate ions [43]. On the other hand, decreases in bulk viscosity of mAb samples in histidine buffer have been reported at pH 6.0 [45-47]. Esue *et al.* further reported that while the highest elastic modulus or gel-like behavior was found in the mAb protein solution in the pH range 4-6, deprotonation of histidine residue decreased the ability of mAb to interact with citrate ion (with a net negative charge) [42]. As a result, the mAb samples in histidine buffer had lower protein-ion interaction, resulting in lower gel-like properties. These observations, although with a different IgG1 mAb, are consistent with particle formation at the air-solution interface observed in this work. Surface pressures vs. area isotherms demonstrate the highest hysteresis for mAb solution in citrate buffer, suggesting the formation of the elastic gel-like film at the interface. Further, mAb samples in citrate buffer at pH 4.5 displayed gel-like fibril formation, rather than clusters at the interface. Moreover, compared to citrate, mAb samples in histidine buffer showed less hysteresis at each of the solution pH values studied. In addition, AFM images of mAb proteins in solutions containing histidine ions formed more loose thread-like structures at the interface.

5.5. Conclusions

In this work, we have examined protein particle formation in bulk solution and in interfacial protein films for a model IgG1 mAb in different formulations, as a means to correlate how stresses and protein interactions at the air-water interface may be attributed to differences in protein particle levels in mechanically agitated mAb solutions. Our results demonstrate that the buffer type and the solution pH of mAb samples affect the extent and morphology of mAb particle formation at the air-solution interface, which in turn affects the levels and shape of protein particles detected in the bulk mAb solution. Comparison of particle formation between mechanical agitated and

interfacial stressed mAb protein samples in this work confirmed previous findings with other mAbs on the significant role of interfacial stress in protein particle formation in bulk mAb solutions [27, 29]. One common approach to stabilize mAb formulations from agitation stress is to avoid/reduce the surface activity of mAb samples, by adding more thermodynamically favorable compounds, such as non-ionic surfactants such as polysorbates, that compete with mAb molecules for the air-water interface [48, 49]. However, these additives are difficult to remove, may accelerate other protein degradation/aggregation pathways, and are labile and prone to self-degrade [33, 48]. Although this study focused on mAb particle formation in response to changes in buffer type and pH, future work will include addition of different concentrations of polysorbates and other surface active molecules. Finally, we suggest that the experimental methodology, as summarized Figure 1, could be an effective screening tool of various excipient classes and types to identify combinations of additives to minimize interfacial particle formation and thus develop more stable therapeutic protein drug formulations.
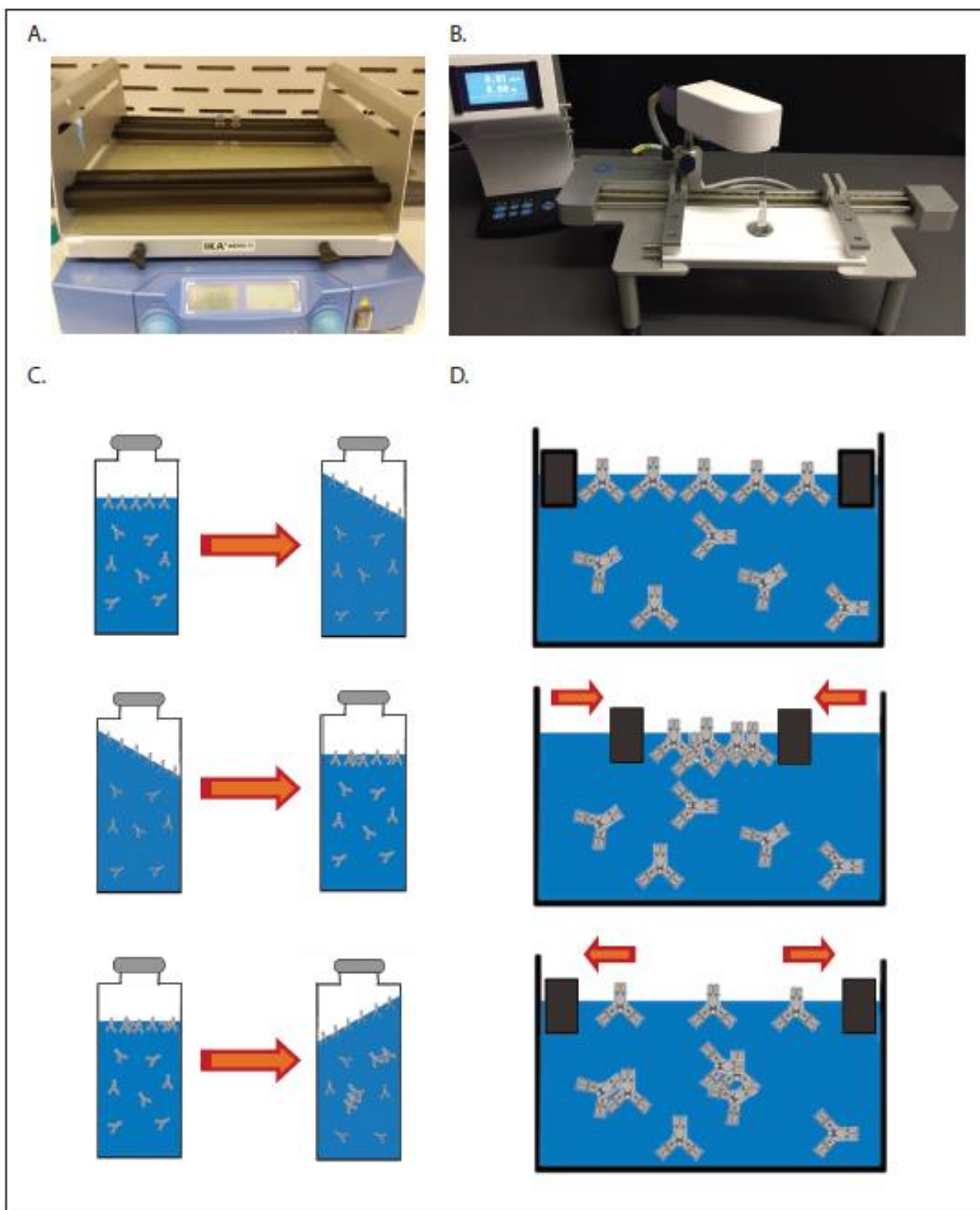
ACKNOWLEDGMENTS

5.6. Figures

Figure 1. Schematic illustration of interfacial stress and subsequent protein particle formation during mechanical agitation of mAb samples in glass vials vs. controlled compression-expansion in a Langmuir trough. (A) System used to shake sample vials in a side-to-side motion. (B) Image of the Langmuir trough connected to a pressure sensor used to apply interfacial mechanical stress and monitor the surface pressure with changes in interfacial area. Panel C and D are schematic illustrations of the potential correlation between mechanisms of protein particle formation in mAb samples subjected to (C) mechanical agitation in vials, and (D) interfacial stress in a Langmuir trough.
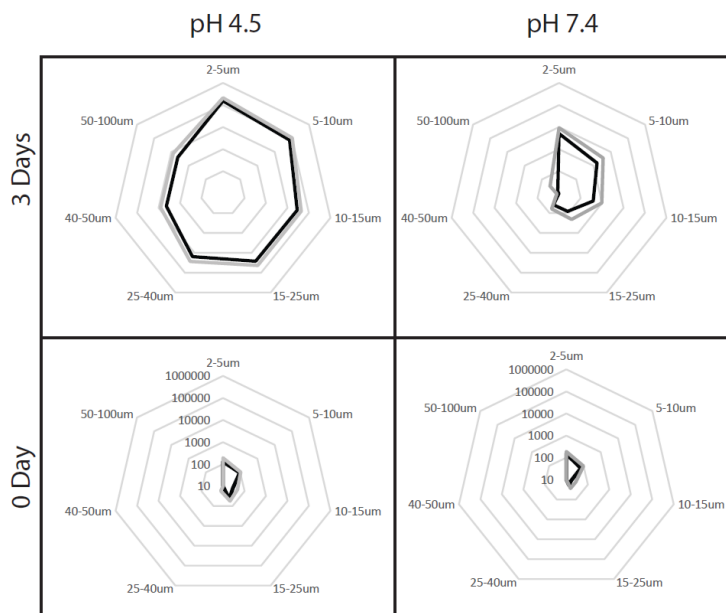
Figure 2. Radar chart analysis of flow digital images of subvisible particles formed in mAb solutions in PBS buffer at pH 4.5 or 7.4 at time 0 or after 3 days of side-to-side shaking in glass vials. Each axis of the radar charts represent a particular particle size range (labelled on figure). The black signal represents the average number of protein particles (n=3) and the grey signal represents average plus the standard deviation. The radar charts in this figure use a logarithmic scale with the center of chart representing 10 particles/ml and each concentric polygon of the chart marking a 10x increase in the particle number. The outermost polygon comprising each radar chart marks a particle concentration of 1,000,000 particles/ml for each corresponding size range.
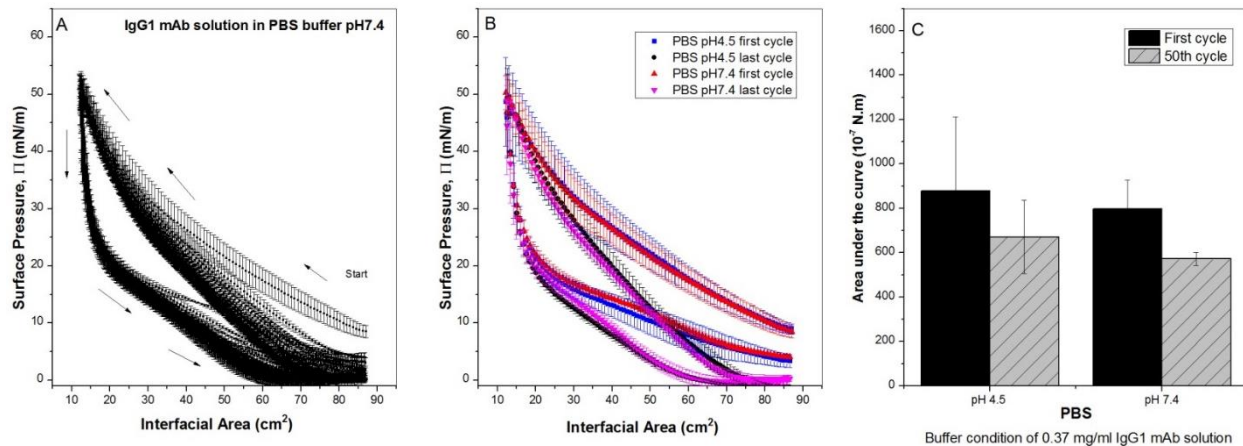
Figure 3. (A) Surface pressure vs. area isotherms of 0.37 mg/ml mAb samples in PBS buffer at pH 7.4 subjected to 50 cycles of compressions-expansion during 6 hours (slow rate) in Langmuir trough. Results are presented as mean and SD (n=3). (B) The first and last cycle of compression-expansion isotherms for mAb sample in PBS buffer at pH 7.4 and 4.5. Results are presented as mean and SD, (n=3). (C) Comparing the area under the compression-expansion isotherm (hysteresis) of the first and last cycle for mAb sample in PBS buffer at pH 7.4 and at 4.5. Results are presented as mean and SD (n=3).
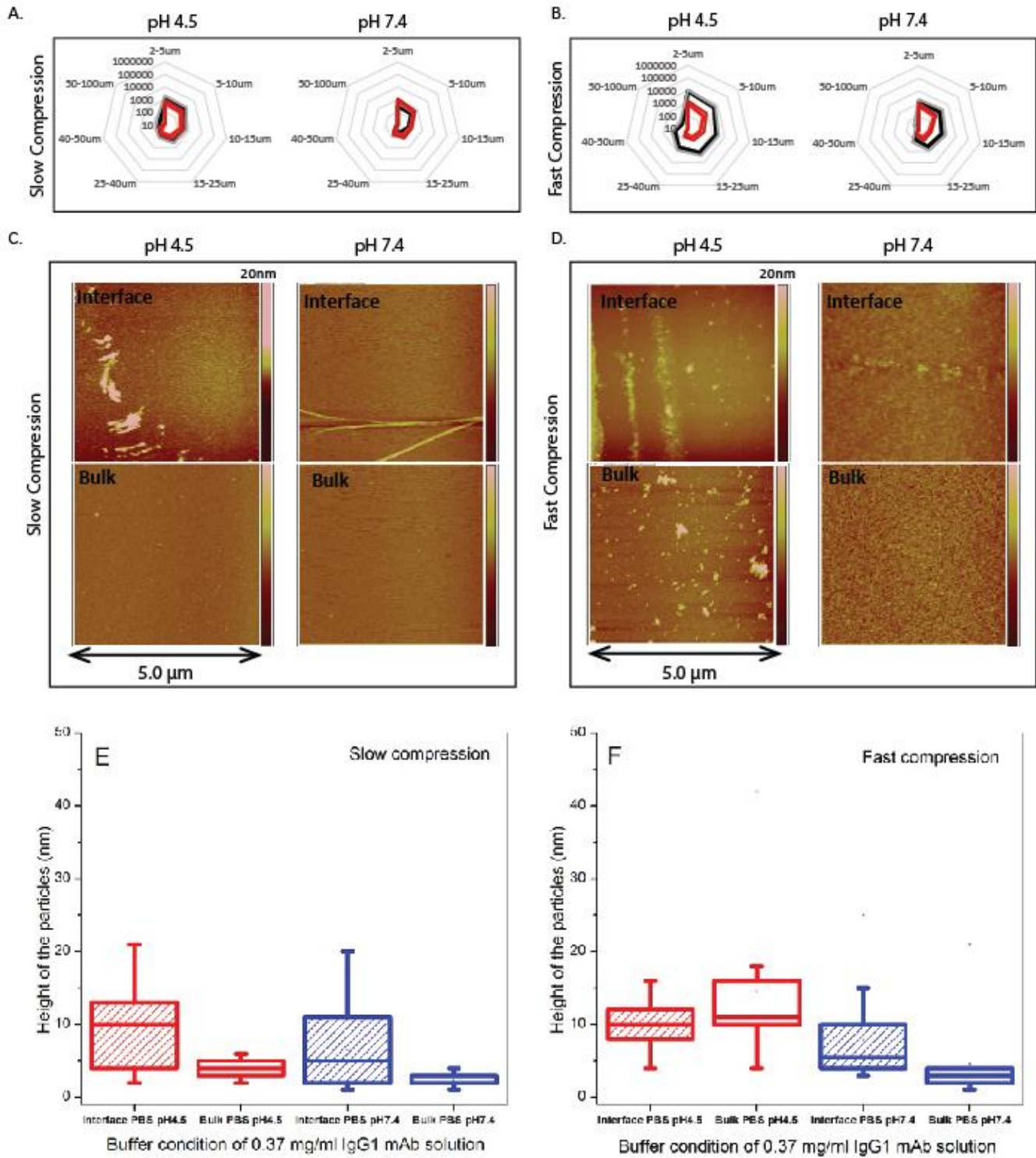
A.

Slow Compression

pH 4.5

pH 7.4

B.

Fast Compression

pH 4.5

pH 7.4

C.

Slow Compression

pH 4.5 — Interface, Bulk

pH 7.4 — Interface, Bulk

20nm

5.0 µm

D.

Fast Compression

pH 4.5 — Interface, Bulk

pH 7.4 — Interface, Bulk

20nm

5.0 µm

E

Slow compression

Height of the particles (nm)

Interface PBS pH4.5   Bulk PBS pH4.5   Interface PBS pH7.4   Bulk PBS pH7.4

Buffer condition of 0.37 mg/ml IgG1 mAb solution

F

Fast compression

Height of the particles (nm)

Interface PBS pH4.5   Bulk PBS pH4.5   Interface PBS pH7.4   Bulk PBS pH7.4

Buffer condition of 0.37 mg/ml IgG1 mAb solution

138

Figure 4. (A, B) Radar chart analysis of flow digital images of subvisible particles formed in Langmuir trough for mAb samples in PBS buffer at pH 4.5 and 7.4 after 6 hours of slow compression (panel A), fast compression (Panel B), or room temperature incubation (red trace in panel A and B). Each axis of the radar charts represent a particular particle size range (labelled on figure). The black signal represents the average number of particles (n=3) formed during stressed conditions and the grey signal represents average plus the standard deviation. The red signal represents the average number of particles (n=3) formed during a 'no-stress' condition with the dark red signal representing the average plus standard deviation. The radar charts in this figure use a logarithmic scale with the center of chart representing 10 particles/ml and each concentric polygon of the chart marking a 10x increase in the particle number. The outermost polygon comprising each radar chart marks a particle concentration of 1,000,000 particles/ml for each corresponding size range. (C, D) AFM images of protein particles formed at air-solution interface and bulk mAb solution subjected to the slow (Panel C) or fast (Panel D) compression. The mAb particles at interface or in the bulk solution were transferred on a freshly cleaved mica sheet by a brief horizontal contact with the interface or being allowed to sit in trough, respectively. (E, F) the height analysis of AFM images of the mAb particles formed at air-solution interface or bulk solution of compressed samples in 1x PBS buffer at pH 4.5 or 7.4 subjected to the slow (Panel E) and fast (Panel F) compression (N=9).
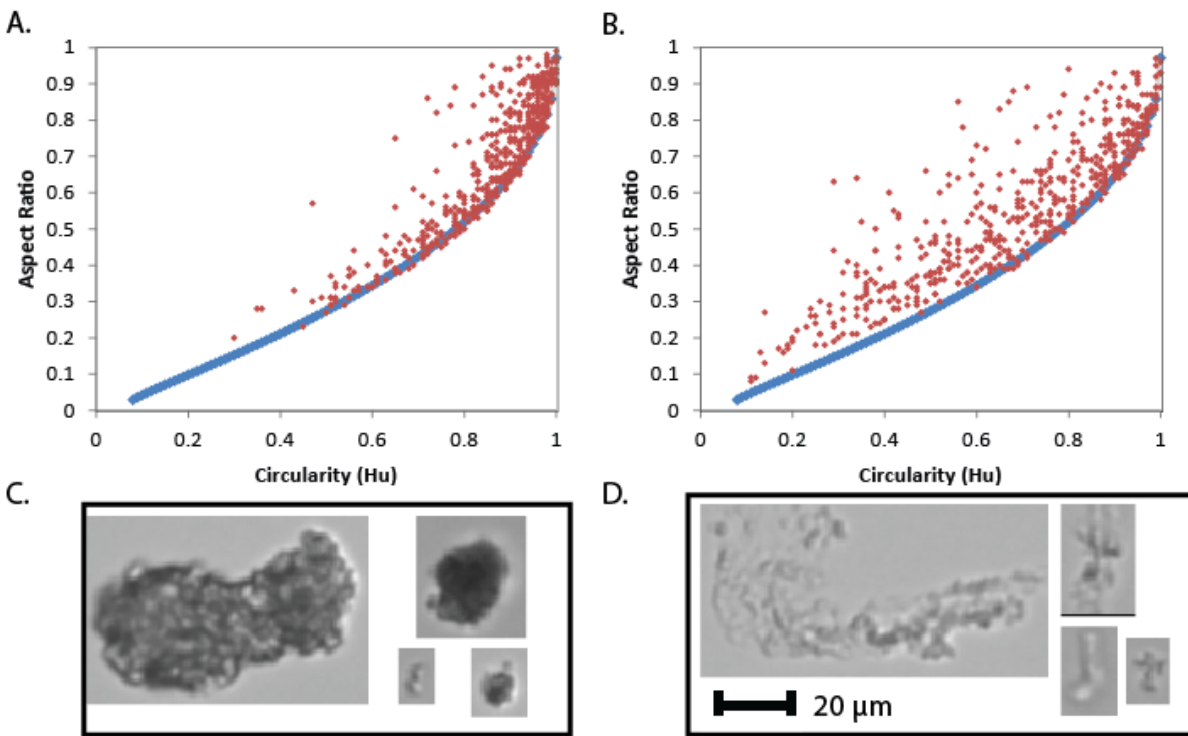
Figure 5. Morphology of protein particles detected in bulk solution after stress conditions as measured by flow digital imaging. (A) Scatter plot of the first 500 particles detected in a mAb sample in PBS buffer at pH 4.5 subjected to 8 hours of fast compression. The blue line represents the morphology of an ellipse calculated using the Ellipsoid-Volume method[38] to characterize the morphology of the particles (see text). (B) Scatter plot of the first 500 particles detected in a mAb sample in PBS buffer at pH 4.5 subjected to 3 days of side-to-side shaking in a glass vial at 300 RPM. (C) Representative protein particle images for the fast compression sample. (D) Representative protein particle images of the stressed mAb samples from flow digital imaging analysis.
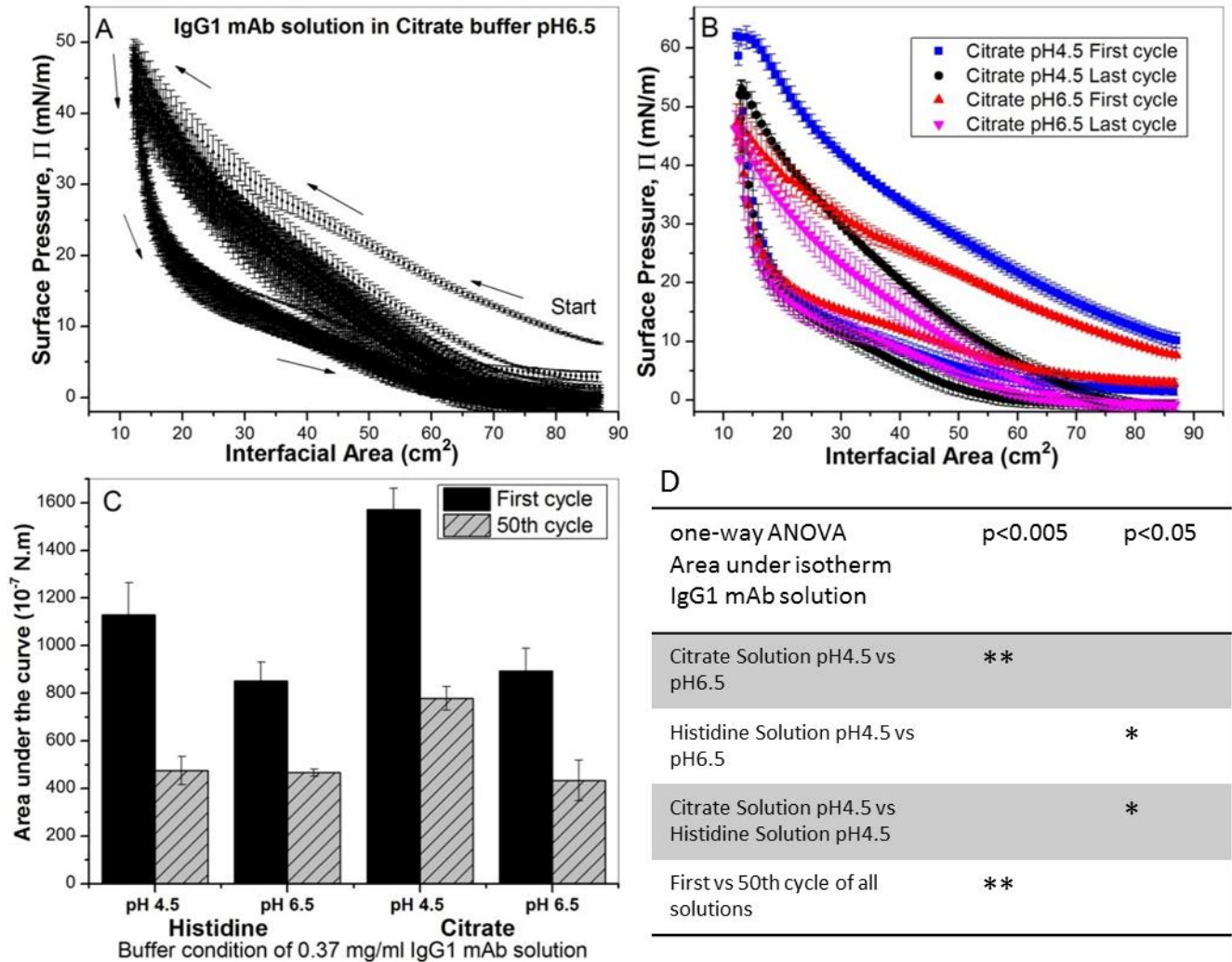
Figure 6. (A) Surface pressure vs. area isotherms of 0.37 mg/ml IgG1 mAb in citrate buffer at pH 6.5 subjected to slow compressions-expansions rate in Langmuir trough. Results are presented as mean and SD, (n=3). (B) Comparison of the first and last cycle of compression-expansion isotherms for mAb samples in citrate buffer at pH 4.5 and 6.5. Results are presented as mean and SD, (n=3). (C) Comparison of the area under the compression isotherms of the first and last cycles for mAb samples in histidine or citrate buffer at pH 4.5 and 6.5. Results are presented as mean SD, (n=3). (D) One-way ANOVA analysis of the area under the compression isotherms (hysteresis) of the first and last cycles of mAb samples presented in panel C.
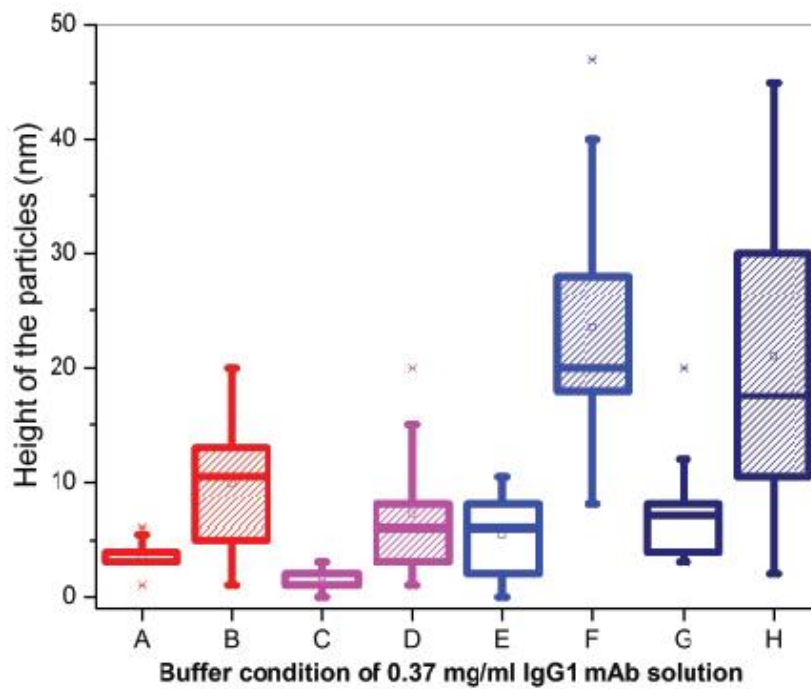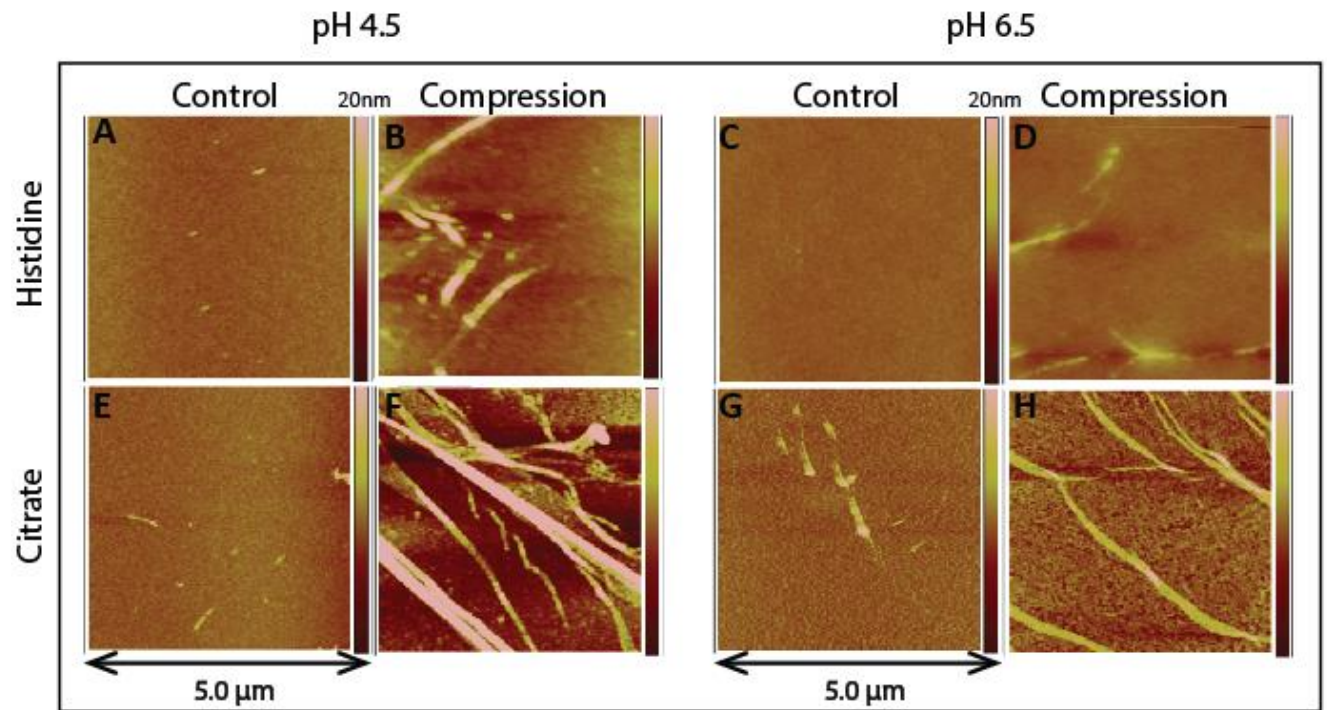
Panel D table:

one-way ANOVA Area under isotherm IgG1 mAb solution	$p < 0.005$	$p < 0.05$
Citrate Solution pH4.5 vs pH6.5	**	
Histidine Solution pH4.5 vs pH6.5		*
Citrate Solution pH4.5 vs Histidine Solution pH4.5		*
First vs 50th cycle of all solutions	**	

pH 4.5   pH 6.5

Control   20nm   Compression   Control   20nm   Compression

Histidine

Citrate

5.0 µm   5.0 µm

Height of the particles (nm)

Buffer condition of 0.37 mg/ml IgG1 mAb solution

Figure 7. (Top Panel) High resolution topographical AFM images of mAb protein films show IgG1 mAb particles formed at air-solution interface of samples formulated in histidine or citrate buffer at pH 4.5 and 6.5 and subjected to slow compression-expansion in Langmuir trough. (Bottom Panel) Height analysis of the AFM images of the mAb particles in slow compression-expansion and control for the same conditions as the top panel (n=9). The control samples correspond to protein films transferred from the air-protein solution interface of mAb samples that were not subjected to any interfacial mechanical stresses.
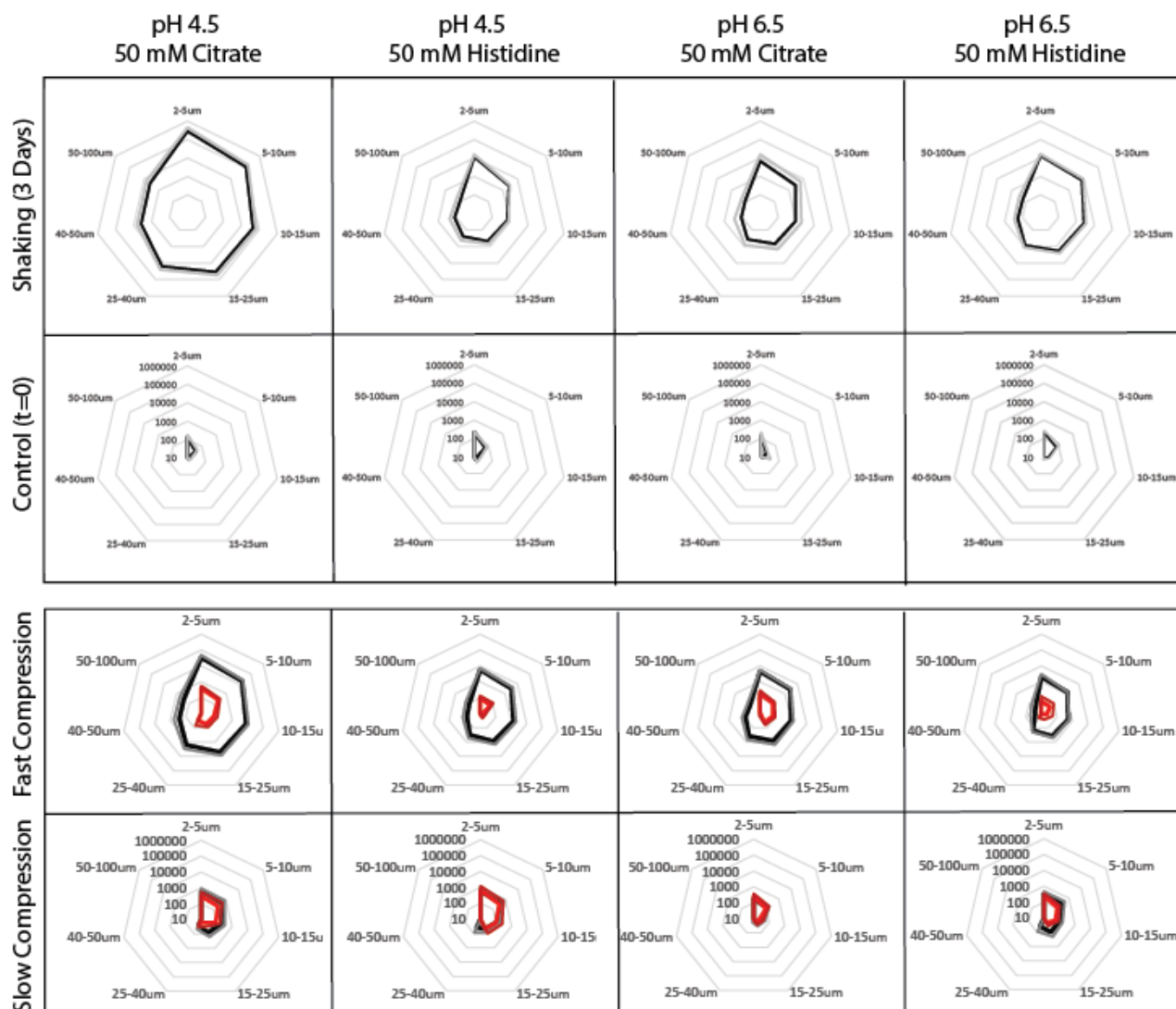
Figure 8. Radar chart analysis of flow digital images of subvisible particles formed in bulk mAb samples in histidine or citrate buffers at pH 4.5 or 6.5. (Top) samples subjected to 0 or 3 days of side-to-side shaking in glass vials at 300 RPM. The black signal represents the average number of particles (n=3) and the grey signal represents average plus the standard deviation. (Bottom) samples subjected to 6 hours of fast compression, slow compression, or room temperature incubation in Langmuir trough. The black signal represents the average number of particles (n=3) formed during compression and the grey signal represents average plus the standard deviation.

The red signal represents the average number of particles (n=3) formed during room temperature incubation with the dark red signal representing the average plus standard deviation. The radar charts in this figure use a logarithmic scale with the center of chart representing 10 particles/ml and each concentric polygon of the chart marking a 10x increase in the particle number. The outermost polygon comprising each radar chart marks a particle concentration of 1,000,000 particles/ml for each corresponding size range.
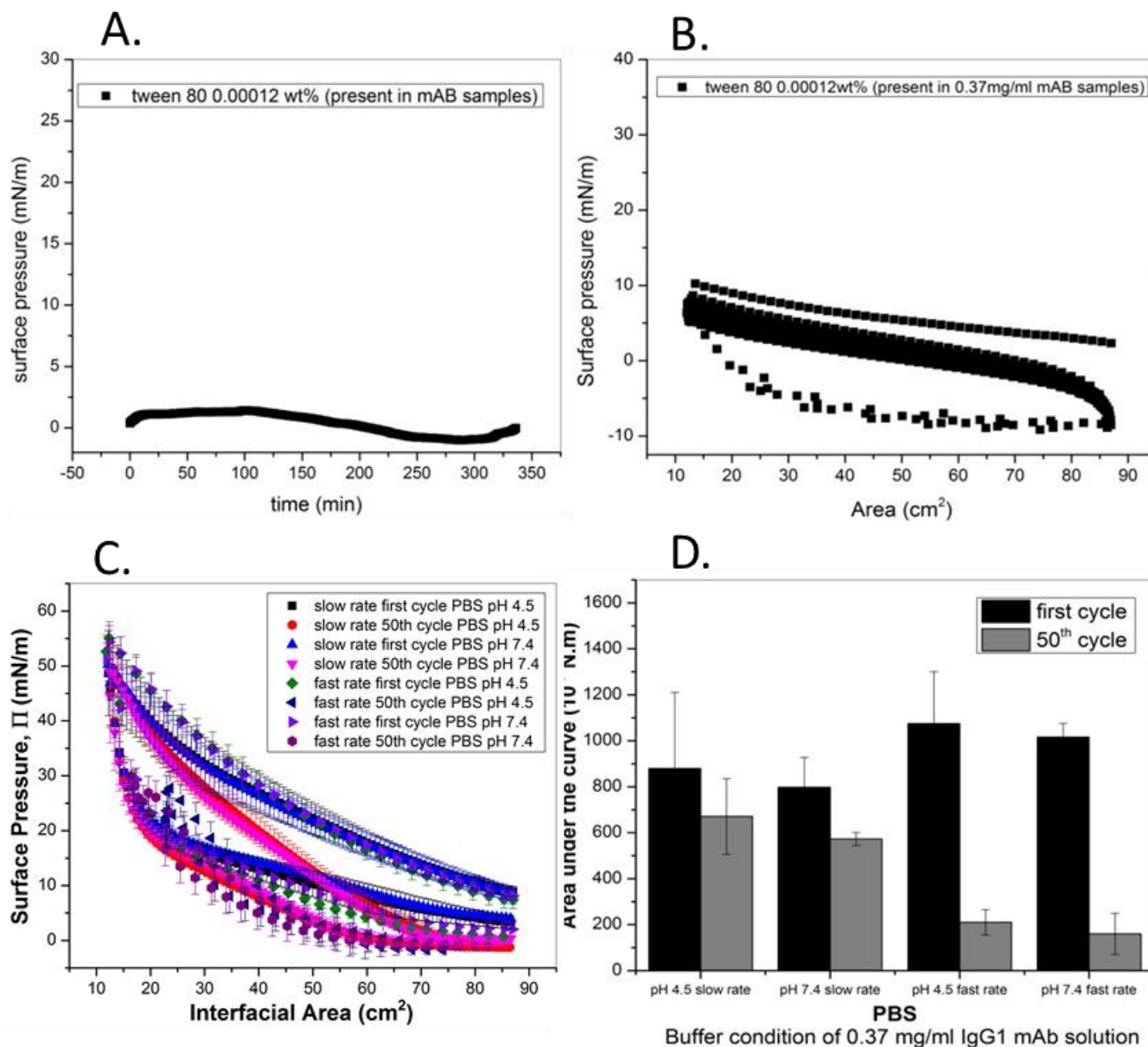
Supplementary Figures:
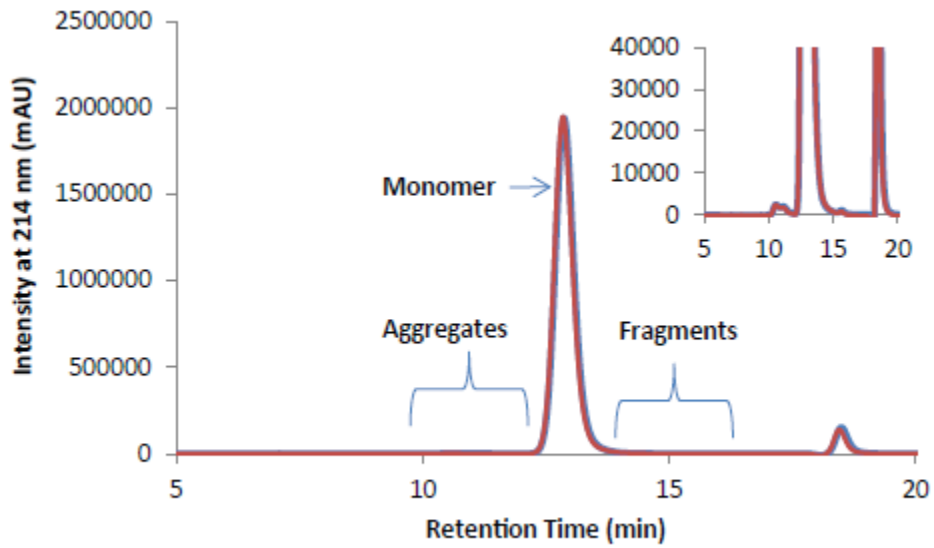
Supplementary Figure S1. Representative SEC chromatogram overlay for mAb samples in pH 7.4 PBS buffer that were shaken in vials side-to side for 3 days (blue) and the corresponding unstressed control (red). The insert is a zoomed in view of the chromatograms. Aggregates are also referred to as high molecular weight species (HMWS) in the text.
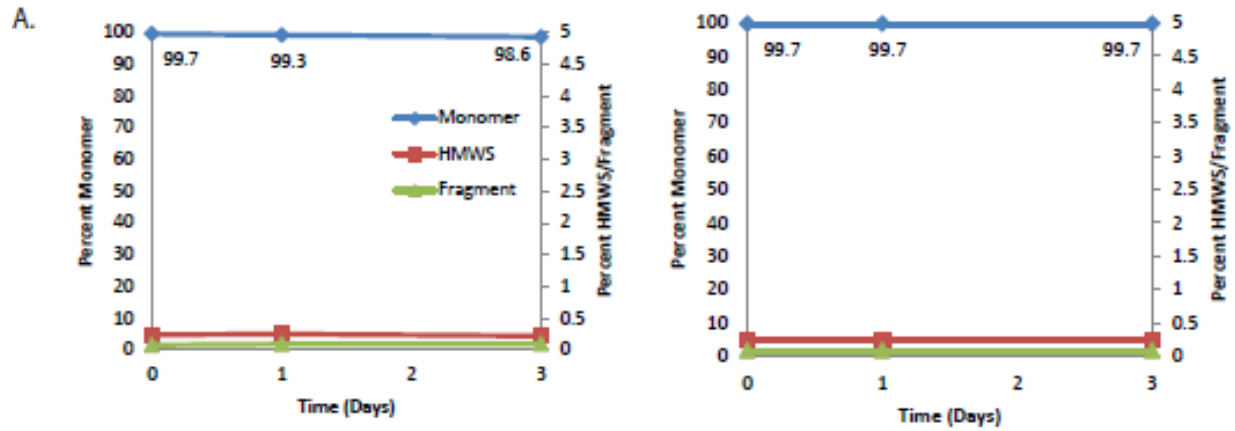
Supplementary Figure S2. The fraction of monomer, high molecular weight species (HMWS), and fragments for the shake stressed mAb samples in PBS buffer as measured by size exclusion chromatography (SEC). Values obtained from integrated SEC chromatograms normalized to t=0 values. The SEC was performed in triplicate (n=3) and error bars are plotted as standard deviation. (A) mAb solution at pH 4.5, and (B) mAb solution at pH 7.4.

Supplementary Figure S3. (A) Adsorption of polysorbate 80 at 0.00012 wt.% as surface pressure vs time.

(B) Surface pressure-area isotherm of polysorbate 80 at 0.00012 wt.% through slow compression-expansion

cycles. The samples contain the same concentration of polysorbate 80 in water that is present in the mAb

samples throughout the study. The low surface pressure of polysorbate 80 at this concentration indicates

the surface pressure that was measured through the study is due to presence of mAb itself. (C) the **first and**

50th cycle of slow (6hours) and fast rate (25min) of compression-expansion isotherms for mAb sample in 1x PBS buffer at pH7.4 and at 4.5. Results are presented as mean and SD, (n=3). (D) Comparing the area under the compression-expansion isotherm (hysteresis) of the **first and 50th cycle** for mAb sample in 1x PBS buffer at pH 7.4 and at 4.5 for both slow and fast compression. Results are presented as mean and SD (n=3).
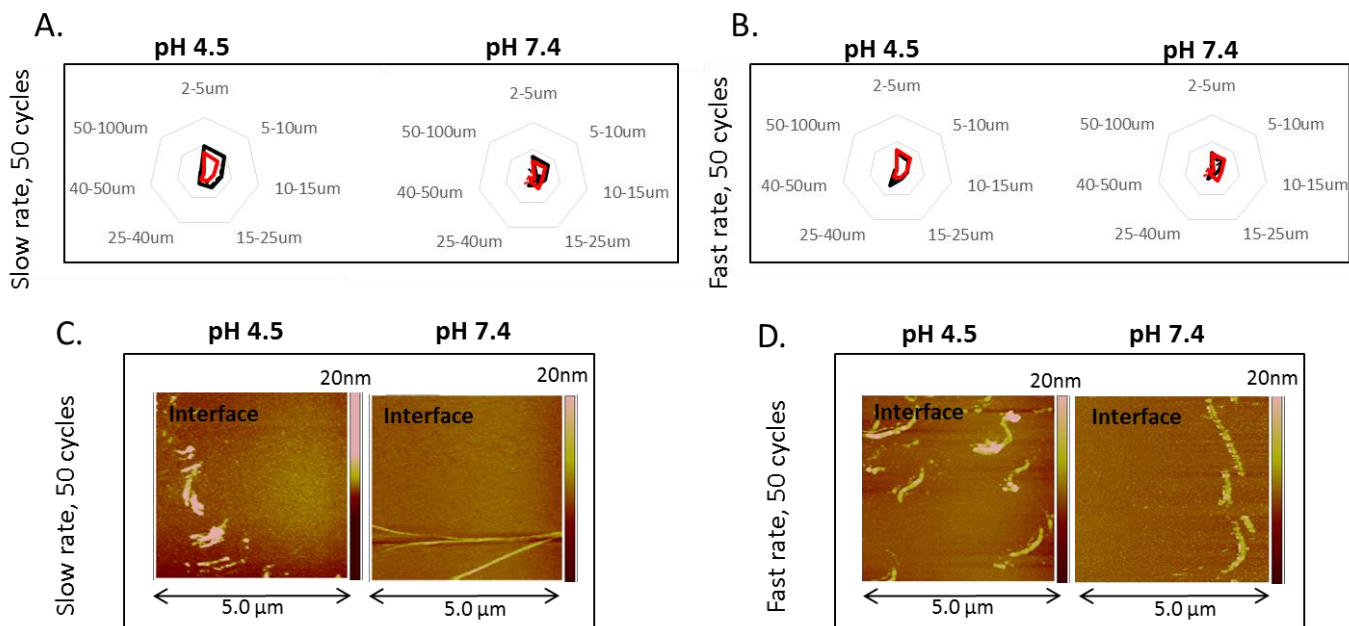
Supplementary Figure S4. (A,B) Radar chart array of mAb particles suspended in bulk solution of pH 4.5 or 7.4 1x PBS buffer after **50 cycles (6 hours) of slow compression (panel A)**, **50 cycles (25 min) of fast compression (Panel B)**, or room temperature incubation (red trace in panel A and B). Each axis of the radar charts represent a particular particle size range (labelled on figure). The black signal represents the average number of particles (n=3) formed during stressed conditions and the grey signal represents average plus the standard deviation. The red signal represents the average number of particles (n=3) formed during a 'non-stressed condition' with the dark red signal representing the average plus standard deviation. The radar charts in this figure use a logarithmic scale with the center of chart representing 10 particles/ml and each concentric polygon of the chart marking a 10x increase in the particle number. The outermost polygon comprising each radar chart marks a particle concentration of 1,000,000 particles/ml for each corresponding size range. (C,D) representative AFM images of IgG1 mAb particles formed at air-solution interface subjected to **50 cycles (6 hours) of slow compression** (Panel C) or **50 cycles (25 min) of fast compression** (Panel D) compression. MAb particles at interface or bulk solution were transferred on a freshly cleaved mica sheet by a brief horizontal contact with the interface or being allowed to sit in trough, respectively.
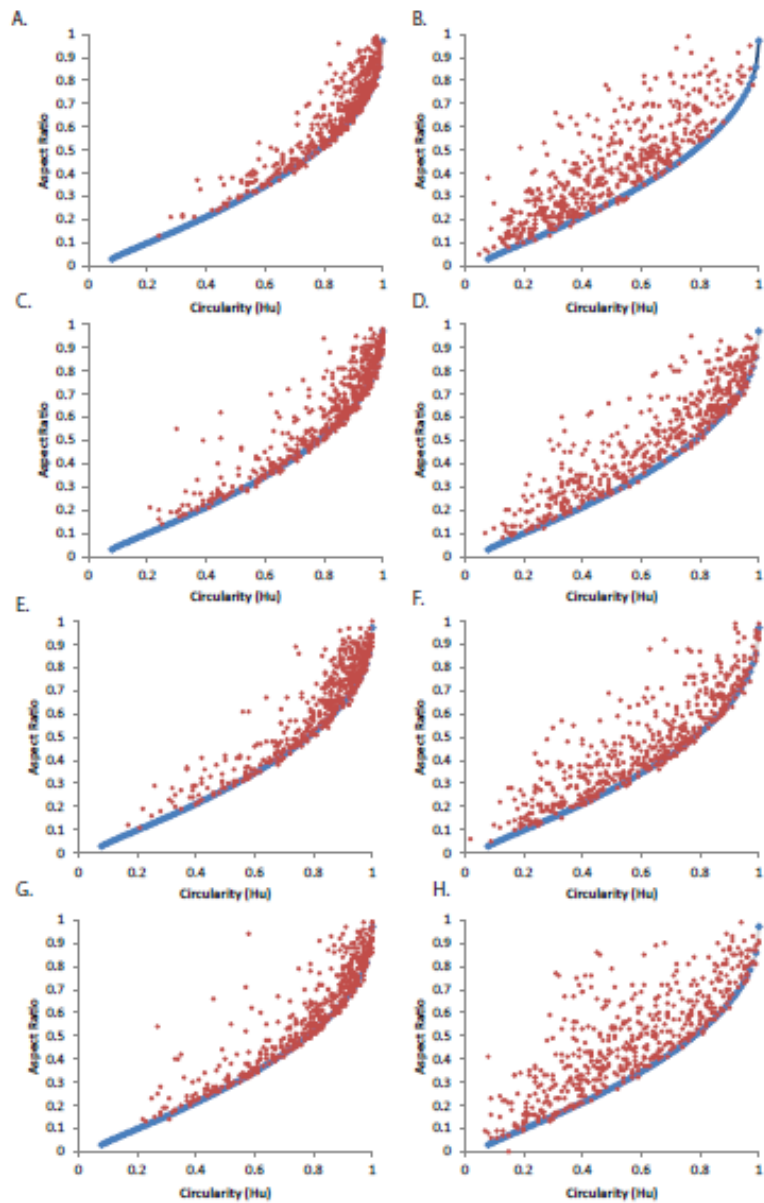
**Supplementary Figure S5.** Morphology of particles detected in bulk solution after stress conditions. Representative scatter plots of the first 500 particles detected during a fluid microscopy measurements. The blue line in each plot represents the morphology of an ellipse calculated using the Ellipsoid-Volume method to characterize the morphology of the particles (see text)[38]. The left column (A, C, E, G) contains samples

stressed by 200 mm/min (fast) compression for 6 hours. The right column (B, D, F, H) contains samples stressed for 3 days by side-to-side shaking. The rows are divided by formulation of the mAb samples with top row (A, B) pH 4.5 50 mM citrate, the second row (C, D) pH 6.5 50 mM citrate, the third row (E, F) pH 4.5 50 mM histidine, and the last row (G, H) pH 6.5 histidine.
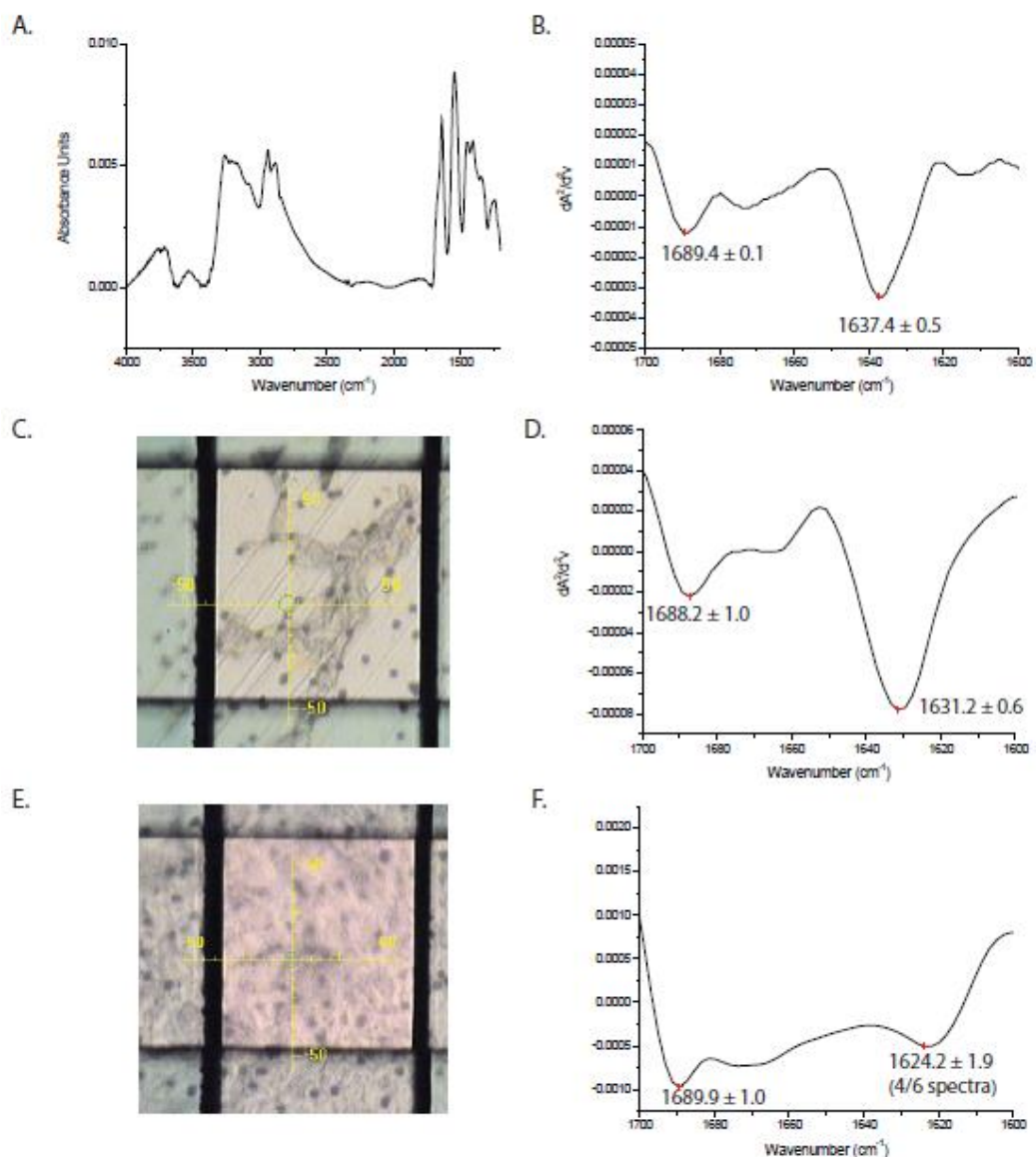
Supplementary Figure S6. Secondary structure analysis of imaged protein particles (formed in pH 7.4 PBS mAb samples subjected to fast compression for 6 hours) as measured by FTIR and FTIR microscopy. A) Representative FTIR spectra of the native mAb control solution. B) Representative second derivative spectra of the amide I region for the native mAb control. Peaks are given as the average of 3 replicates. C) Representative particle image captured using FTIR microscopy to analyze particles formed during fast compression. D) Representative second derivative FTIR spectra of the amide I region for a particle formed during fast compression. Peak values (mean and SD) are given as the average of 9 particles. E) Representative particle image captured using FTIR microscopy to analyze particles formed after extensive

heat denaturation at 90 °C. D) Representative second derivative FTIR spectra of the amide I region for a particle formed during extensive heat denaturation at 90 °C. Peak values (mean and SD) are given as the average of 6 particles.
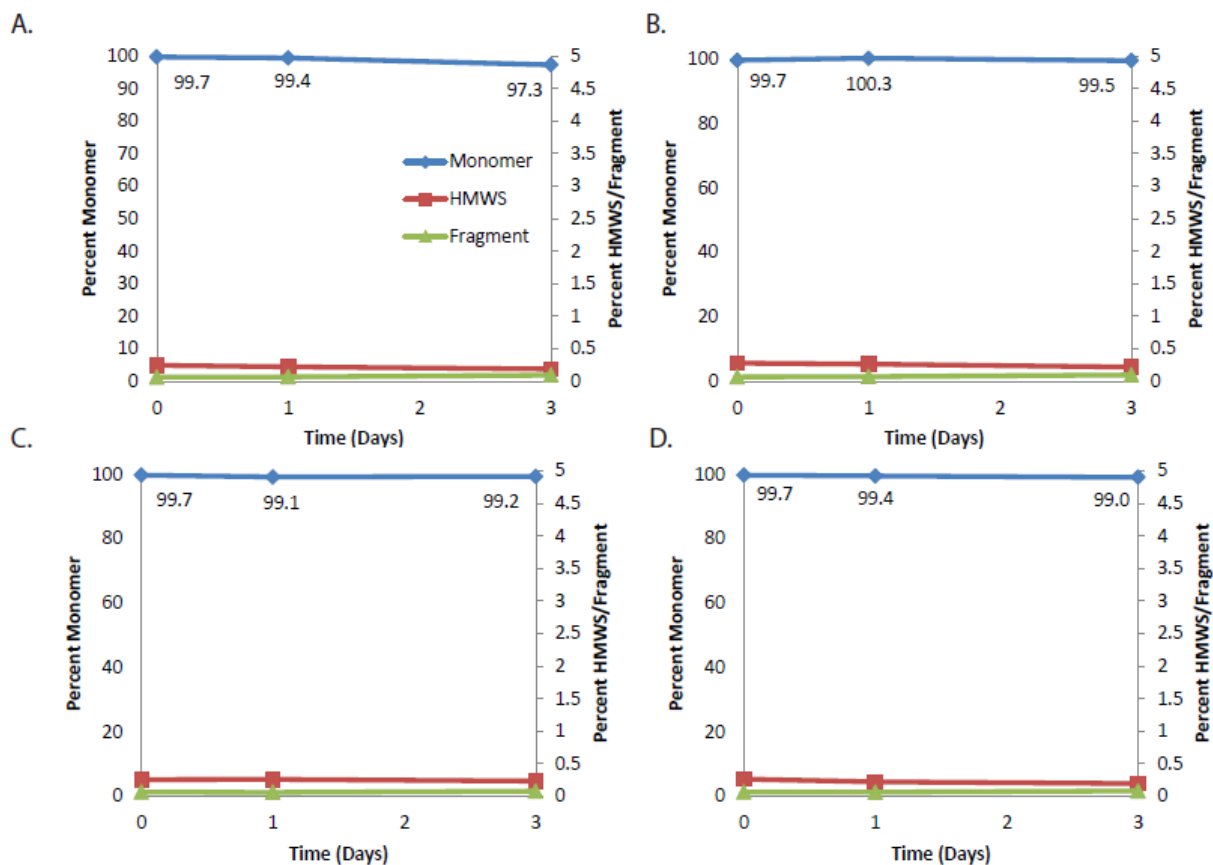
Supplementary Figure S7. The fraction of monomer, high molecular weight species (HMWS), and fragments for the shake stressed mAb samples in different formulations. Values obtained from integrated SEC chromatograms normalized to t=0 values. The SEC is performed in triplicate (n=3), error bars were plotted as standard deviation. MAb solution at (A) pH 4.5 in 50mM citrate buffer, (B) pH 6.5 in 50mM citrate buffer, (C) pH 4.5 in 50mM histidine buffer, and (D) pH 6.5 in 50mM histidine buffer.

5.7. References

1. Ratanji, K.D., et al., *Immunogenicity of therapeutic proteins: influence of aggregation.* J Immunotoxicol, 2014. **11**(2): p. 99-109.

2. Rosenberg, A.S., *Effects of protein aggregates: an immunologic perspective.* AAPS J, 2006. **8**(3): p. E501-7.

3. Carpenter, J.F., et al., *Overlooking subvisible particles in therapeutic protein products: gaps that may compromise product quality.* J Pharm Sci, 2009. **98**(4): p. 1201-5.

4. Bi, V., et al., *Development of a human antibody tolerant mouse model to assess the immunogenicity risk due to aggregated biotherapeutics.* J Pharm Sci, 2013. **102**(10): p. 3545-55.

5. Joubert, M.K., et al., *Highly Aggregated Antibody Therapeutics Can Enhance the in Vitro Innate and Late-stage T-cell Immune Responses.* Journal of Biological Chemistry, 2012. **287**(30): p. 25266-25279.

6. Xiang, S.D., et al., *Pathogen recognition and development of particulate vaccines: does size matter?* Methods, 2006. **40**(1): p. 1-9.

7. Corvari, V., et al., *Subvisible (2–100 μm) particle analysis during biotherapeutic drug product development: Part 2, experience with the application of subvisible particle analysis.* Biologicals, 2015.

8. Narhi, L.O., et al., *Subvisible (2–100 μm) Particle Analysis During Biotherapeutic Drug Product Development: Part 1, Considerations and Strategy.* Journal of pharmaceutical sciences, 2015. **104**(6): p. 1899-1908.

9. Joubert, M.K., et al., *Classification and characterization of therapeutic antibody aggregates.* J Biol Chem, 2011. **286**(28): p. 25118-33.

10. Luo, Q., et al., *Chemical modifications in therapeutic protein aggregates generated under different stress conditions.* J Biol Chem, 2011. **286**(28): p. 25134-44.

11. Telikepalli, S.N., et al., *Structural characterization of IgG1 mAb aggregates and particles generated under various stress conditions.* J Pharm Sci, 2014. **103**(3): p. 796-809.

12. Telikepalli, S., et al., *Physical characterization and in vitro biological impact of highly aggregated antibodies separated into size-enriched populations by fluorescence-activated cell sorting.* J Pharm Sci, 2015. **104**(5): p. 1575-91.

13. Bukofzer, S., et al., *Industry perspective on the medical risk of visible particles in injectable drug products.* PDA J Pharm Sci Technol, 2015. **69**(1): p. 123-39.

14. Filipe, V., et al., *Immunogenicity of different stressed IgG monoclonal antibody formulations in immune tolerant transgenic mice.* MAbs, 2012. **4**(6).

15. Singh, S.K., et al., *An industry perspective on the monitoring of subvisible particles as a quality attribute for protein therapeutics.* J Pharm Sci, 2010. **99**(8): p. 3302-21.

16. Banks, D.D., et al., *Native-state solubility and transfer free energy as predictive tools for selecting excipients to include in protein formulation development studies.* J Pharm Sci, 2012. **101**(8): p. 2720-32.

17. Andersen, C.B., et al., *Aggregation of a multidomain protein: a coagulation mechanism governs aggregation of a model IgG1 antibody under weak thermal stress.* Protein Sci, 2010. **19**(2): p. 279-90.

18. Philo, J.S. and T. Arakawa, *Mechanisms of protein aggregation.* Curr Pharm Biotechnol, 2009. **10**(4): p. 348-51.

19. Li, Y. and C.J. Roberts, *Lumry-Eyring nucleated-polymerization model of protein aggregation kinetics. 2. Competing growth via condensation and chain polymerization.* J Phys Chem B, 2009. **113**(19): p. 7020-32.

20. Andrews, J.M. and C.J. Roberts, *A Lumry-Eyring nucleated polymerization model of protein aggregation kinetics: 1. Aggregation with pre-equilibrated unfolding.* J Phys Chem B, 2007. **111**(27): p. 7897-913.

21. Roberts, C.J., *Nucleation, Aggregation, and Conformational Distortion*, in *Biophysical Methods for Biotherapeutics: Discovery and Development Applications*, T.K. Das, Editor. 2014, John Wiley & Sons, Inc: Hoboken. p. 125-144.

22. Chi, E.Y., et al., *Physical stability of proteins in aqueous solution: mechanism and driving forces in nonnative protein aggregation.* Pharm Res, 2003. **20**(9): p. 1325-36.

23. Roberts, C.J., T.K. Das, and E. Sahin, *Predicting solution aggregation rates for therapeutic proteins: approaches and challenges.* Int J Pharm, 2011. **418**(2): p. 318-33.

24. Kumru, O.S., et al., *Compatibility, physical stability, and characterization of an IgG4 monoclonal antibody after dilution into different intravenous administration bags.* Journal of pharmaceutical sciences, 2012. **101**(10): p. 3636-3650.

25. Kalonia, C., et al., *Radar chart array analysis to visualize effects of formulation variables on IgG1 particle formation as measured by multiple analytical techniques.* J Pharm Sci, 2013. **102**(12): p. 4256-67.

26. Kiese, S., et al., *Shaken, not stirred: mechanical stress testing of an IgG1 antibody.* J Pharm Sci, 2008. **97**(10): p. 4347-66.

27. Bee, J.S., et al., *Production of particles of therapeutic proteins at the air–water interface during compression/dilation cycles.* Soft Matter, 2012. **8**(40): p. 10329-10335.

28. Shieh, I.C. and A.R. Patel, *Predicting the agitation-induced aggregation of monoclonal antibodies using surface tensiometry.* Molecular pharmaceutics, 2015. **12**(9): p. 3184-3193.

29. Rudiuk, S., et al., *Importance of the dynamics of adsorption and of a transient interfacial stress on the formation of aggregates of IgG antibodies.* Soft Matter, 2012. **8**(9): p. 2651-2661.

30. Kamerzell, T.J., et al., *Protein–excipient interactions: Mechanisms and biophysical characterization applied to protein formulation development.* Advanced drug delivery reviews, 2011. **63**(13): p. 1118-1159.

31. Khan, T.A., H.-C. Mahler, and R.S. Kishore, *Key interactions of surfactants intherapeutic proteinformulations: A review.* European Journal of Pharmaceutics and Biopharmaceutics, 2015.

32. Lee, H.J., et al., *Molecular origins of surfactant-mediated stabilization of protein drugs.* Advanced drug delivery reviews, 2011. **63**(13): p. 1160-1171.

33. Kerwin, B.A., *Polysorbates 20 and 80 used in the formulation of protein biotherapeutics: structure and degradation pathways.* Journal of pharmaceutical sciences, 2008. **97**(8): p. 2924-2935.

34. Liu, L., et al., *The effects of excipients on protein aggregation during agitation: an interfacial shear rheology study.* Journal of pharmaceutical sciences, 2013. **102**(8): p. 2460-70.

35. Fesinmeyer, R.M., et al., *Effect of ions on agitation- and temperature-induced aggregation reactions of antibodies.* Pharm Res, 2009. **26**(4): p. 903-13.

36. Bond, M.D., et al., *Evaluation of a dual-wavelength size exclusion HPLC method with improved sensitivity to detect protein aggregates and its use to better characterize degradation pathways of an IgG1 monoclonal antibody.* J Pharm Sci, 2010. **99**(6): p. 2582-97.

37. Graham, D. and M. Phillips, *Proteins at liquid interfaces: I. Kinetics of adsorption and surface denaturation.* Journal of Colloid and Interface Science, 1979. **70**(3): p. 403-414.

38. Kalonia, C., et al., *Calculating the Mass of Subvisible Protein Particles with Improved Accuracy Using Microflow Imaging Data.* Journal of pharmaceutical sciences, 2015. **104**(2): p. 536-547.

39. Kalonia, C., et al., *Radar chart array analysis to visualize effects of formulation variables on IgG1 particle formation as measured by multiple analytical techniques.* Journal of pharmaceutical sciences, 2013. **102**(12): p. 4256-4267.

40. Razavi, S., et al., *Collapse of Particle-Laden Interfaces under Compression: Buckling vs Particle Expulsion.* Langmuir, 2015. **31**(28): p. 7764-7775.

41. Pocivavsek, L., et al., *Stress and fold localization in thin elastic membranes.* Science, 2008. **320**(5878): p. 912-916.

42. Esue, O., et al. *Thermodynamic and structural characterization of an antibody gel*. in *Mabs*. 2013. Taylor & Francis.

43. Esue, O., et al., *Carboxylate-dependent gelation of a monoclonal antibody.* Pharmaceutical research, 2009. **26**(11): p. 2478-2485.

44. Rajagopalan, R. and P.C. Hiemenz, *Principles of colloid and surface chemistry.* Marcel Dekker, New-York, 3e édition, ISBN 0, 1997. **8247**(9397): p. 8.

45. Chen, B., et al., *Influence of histidine on the stability and physical properties of a fully human antibody in aqueous and solid forms.* Pharmaceutical research, 2003. **20**(12): p. 1952-1960.

46. Katdare, A. and M. Chaubal, *Excipient development for pharmaceutical, biotechnology, and drug delivery systems.* 2006: CRC Press.

47. Salinas, B.A., et al., *Understanding and modulating opalescence and viscosity in a monoclonal antibody formulation.* Journal of pharmaceutical sciences, 2010. **99**(1): p. 82-93.

48. Mahler, H.C., et al., *Surface activity of a monoclonal antibody.* Journal of pharmaceutical sciences, 2009. **98**(12): p. 4525-4533.

49. Serno, T., et al., *Inhibition of agitation‐induced aggregation of an IgG‐antibody by hydroxypropyl‐β‐cyclodextrin.* Journal of pharmaceutical sciences, 2010. **99**(3): p. 1193-1206.

Chapter 6: Conclusions and future directions

6.1.   Air-water interface in relevant biological and physiological systems

Fluidity is a key factor in functionality of many biological systems, from the cell membrane, to lung surfactants [1-4]. The importance of understanding viscoelasticity of interfaces has resulted in large investments towards designing more sensitive and effective methods to quantify the mechanical properties at the interfaces [5-8]. Active microrheology has been used in this thesis to explore lipid monolayers at the air-water interface. Our studies explore microscopic behavior of the lipids and added to our understanding of their specific chemical-mechanical features, in agreement with current literature. Using micron-sized magnetic rods, the sensitivity of our measurements are increased 100-folds compared to the most recent successful active microrheology technique which had a disk-shaped probe with diameter of 100um [9]. All the lipid monolayers that have been explored in this thesis were complicated and fascinating, and allowed us to discover correlations between the chemical features of these lipids and the fluidity of the monolayers. Specifically, a common theme that emerged was that lipid tail saturation, physical properties of the headgroup moiety, as well as the organization of the lipid headgroups at the air-water interface contributed to the overall fluidity of the monolayer. Saturated lipids, which pack more tightly, had significantly higher surface viscosity compared to the unsaturated lipids. Additionally, the chemical features of the lipid headgroup that affected surface viscosity are: the size which influenced the packing density, and the charge which effected the quality of the interactions. Finally, in this thesis we find that the presence of charged compounds (ions or proteins) in the local environment also contributed to the overall surface viscosity.

Studying transport and cell recognition by monitoring fluidity as a function of ion concentration and pH could be important since it could represent the changes in plasma and inner cell membranes during vital function of the cell, such as endocytosis, specially using more

complex monolayers. Recent research on Alzheimer's disease suggests a strong connection between the cell membrane damaged by altered protein and the initiation of this disease [10, 11]. Interfacial characterization of lipid-protein mixtures relevant to this disease could expand our knowledge about progression of this disease [10, 11]. Furthermore, our understanding of the membrane fluidity could be useful in designing more effective drug delivery methods to open a door to multiple treatments. Of course, it is important to note that rheological measurements ultimately need to be complemented by high resolution techniques such as X-ray diffraction and neutron magnetic resonance (NMR) to obtain molecular-level information on chemical orientation of the molecules at interfaces. However, they can extend our knowledge on microscale properties of biological material and help identify areas of interest that can be explored further to obtain detailed structural information [5, 7]. For example, one can use microrheology techniques to identify significant changes in the surface viscosity corresponding to possible phase changes, and then use grazing angle X-ray diffraction to identify if indeed there was changes in the molecular arrangement [12]. However, it must also be noted that unlike saturated lipids, unsaturated lipids never pack into well-organized structures, and therefore cannot be probed with X-ray [12, 13]. In such cases, microrheology might be a very dependable tool to identify changes in the molecular organization of lipids. Another important point to keep in mind for future studies is that in this thesis, the phospholipid bilayer was modeled as a monolayer representing one leaflet of the cell membrane; future work should focus on developing techniques that directly measure the bilayer fluidity.

The ability to measure the surface viscosity over 100000-fold range (nNs/m) allows us to study the lung surfactants, since the dynamic activity of lung surfactant as a film must accommodate a drastic change of surface viscoelasticity during compression-expansion. While the

fast spreading of the monolayer during the expansion of the lung requires a high fluidity, it should also have a viscosity to accommodate a reversible collapse. Both addition of unsaturated lipids and synthetic version of SP-B, miniB, to the DPPC monolayer modified the maximum viscoelasticity as well as the range of it. Addition of unsaturated lipids, POPC and POPG, to the DPPC had different effect on surface viscosity based on the charge of the headgroup, while in both cases the presence of the miniB increased the surface viscosity. Further studies should study natural LS to identify its natural viscoelastic behavior.

Our findings have applications in designing more effective replacement lung surfactant to treat ARDS. The most clinically successful commercially surfactants, such as Curosurf, Survanta, Infasurf, and Surfaxin, vary significantly in composition and differ in the main component [1, 9, 14]. The role of additives such as palmitic acid and cholesterol, are not fully understood even though these components could greatly influence the chemical-mechanical properties of the LS film [9, 15-17]. We are recognizing the surface viscoelasticity of the replacement LS film as an important parameter that should be used to better understand the role of each LS component in achieving the optimal surface activity. In chapter three and four we have measured the surface viscosity of phospholipid monolayer that were prepared in an organic solvent (chloroform) and therefore formed insoluble monolayer at the air-water interface. While characterizing lung surfactant lipids as insoluble monolayers, called Langmuir monolayers, have been commonly performed, the natural lung surfactant exist in water and must adsorb to the air-water interface before spreading. Our preliminary data (figure 1) using DPPC-POPG mixture in water were designed to test the influence of LS component on fluidity of DPPC-POPG mixture after the adsorption of mixture to the air-water interface reached a steady state. The surface viscosity of DPPC-POPG mixture increased from 10 to 20nNs/m by increase of concentration of SP-B (from

0.025 to 0.05mg/ml). Interestingly by adding 1wt. % cholesterol to the lipid-SP-B mixture, the surface viscosity dropped to the surface viscosity of the control sample (only lipids). These results indicate the importance of natural LS components and their concentration in the overall surface viscosity. Clinical studies would ultimately indicate which of these compositions are more efficient, although the purpose of this thesis is to quantify the crucial properties of the synthetic LS to eliminate the composition expected to fail in clinical trial.

In addition to designing more efficient replacement LS, our fluidity studies could be helpful in understanding the effect of air pollution and presence of these foreign particles on LS film [18]. Our preliminary data (figure 2) indicates that the presence of 1wt.% negatively charged nanoparticles (NP) significantly decreased the surface viscosity of the DPPC-POPG monolayer. This could be due to the repulsive interaction between the negative nanoparticles and the negative charge of the PG headgroup at neutral pH. Since the environmental nano-pollution has caused a safety concern specially targeting the lung function, this experiment serves as motivation as to how NPs can influence surface viscosity which in turn might impact functioning of lung surfactant [18, 19].Further studies are required to evaluate the mechanism of air-pollution on the generation or amplification of lung diseases.

In addition to the application of active microrheology to study interfacial microrheology, this technique can also be applied study complex bulk fluids. Another important application of the increased sensitivity of our active microrheology set-up is that it can be used to understand more about the viscoelastic properties of cells and tissues. In a collaboration with the Department of Anatomy and Cell Biology at KU, we used magnetic nanorods to measure the change in viscoelastic properties of a chicken embryo during the heart development. These studies were carefully performed by injecting the nanorods in the chicken embryo early on in the development

and interestingly, due to the small size of the nanorods their presence did not interfere with the growth and development of the embryo. Therefore, provided an opportunity to characterize the viscoelastic properties of heart tissue in a live embryo. Future studies could shed light on our unanswered questions in tissue regeneration by learning about their chemical-mechanical characteristics.

6.2. Industrial applications

Interfaces are a great source of concern in causing protein aggregation and particle formation in pharmaceutical industry. We have measured and correlated the protein particle formation at the air-water interface and the protein particles found in the bulk for a model IgG1 mAb in chapter 5 of this thesis. The impact of four types of buffer ion and pH on protein particle formation were evaluated for samples subjected to the mechanical agitation. The interfacial characterization, both atomic force microscopy imaging and surface pressure-area isotherms, predicted the formulation that was the most prone to protein particles formation due to mechanical agitation. These studies were specifically interesting since the concentration of surfactant was very low (0.00012wt. %) making the results applicable for biological drugs that should be injected in the brain tissue with zero or very limited surfactant in their formulations [20]. In addition to extending our understanding of protein particle formation, a practical outcome of this study was to introduce the interfacial characterization as an early screening technique for formulation of protein solutions.

An important aspect, that was not presented in chapter 5, but has been identified by other research groups recently, is that the kinetic of adsorption of proteins to the air-water interface is linked to their tendency to aggregate [21] . Our preliminary data presented in figure 3 shows the

adsorption curve of the model IgG1 mAb we studied in chapter 5. The kinetic of adsorption was monitored by recording the change of surface pressure (surface tension) after exposing the protein solution to the air-water interface. The rate in which protein molecules adsorb to the air-water interface is related to their rearrangement in exposure to the hydrophobic interface and favorable conformational changes. It has been suggested that the hydrophobically driven change of conformation, could expose cysteine groups and initiate covalent bonds between molecules [21]. Therefore, the rate of change of surface pressure (surface tension) of protein solutions could indicate the attractive interaction between molecules. Similarly, the influence of surfactant type and concentration as well as other excipients could be studies using this techniques as predictive tools to reduce protein aggregation.

Last, but not the least, recent studies have also identified that formation of interfacial protein gels at hydrophobic interfaces is typically indicative of higher tendency of protein-protein interactions in that solution [22, 23]. Our studies have indicated this gel-like behavior by measuring the irreversibility of the protein film in response to compression-expansion cycles. The higher the irreversibility, the more particles were found in the bulk solution as a result of the mechanical agitation. The gel-like properties of films could be quantified as their viscoelastic properties. Mehta *et. al.* have shown at silicon-water interface the adsorbed protein film had viscoelastic properties by measuring the viscose and elastic modulus of the film [23]. In the presented preliminary data in figure 4, surface viscosity of the studied IgG1 mAb was measured upon injection of protein the solution at the same concentration as previously tested (0.37mg/ml). The surface viscosity was very low at approximately 1 min after injection of the protein to the subphase and the nanorods were turning 90 degrees indicating the sample is not elastic. However, as the time increased the surface viscosity increased and the maximum angel of reorientation

decreased, indicating the elasticity of the film, until a point that the nanorods did not move by the applied magnetic field. It would be interesting to explore the relationship between viscoelastic properties of the protein film and the protein particle formation to design more effective and faster prescreening techniques for formulation of protein samples.
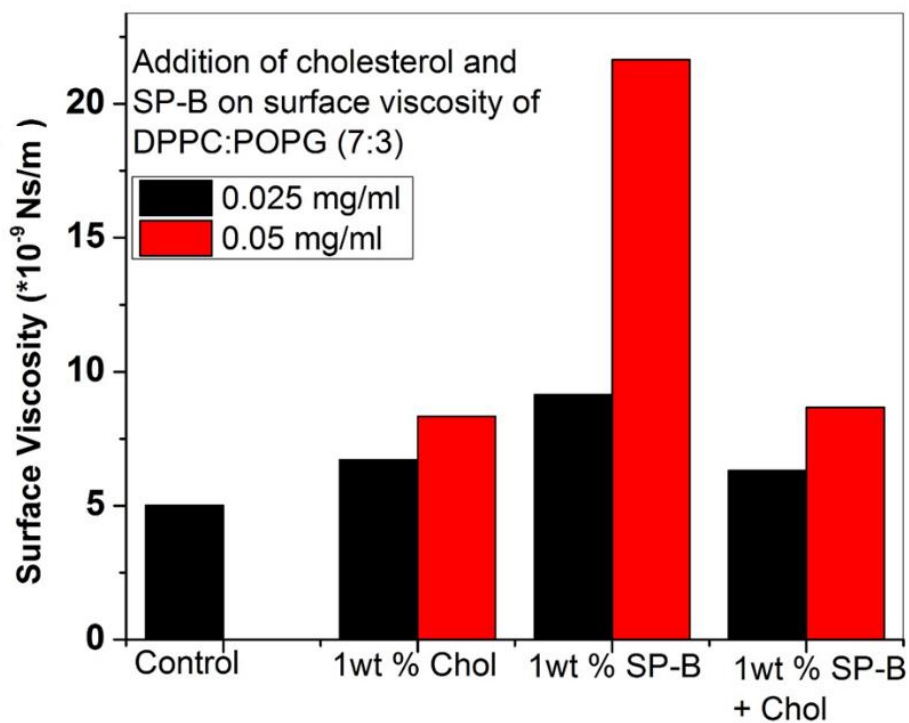
6.3. Figures

Figure1. the surface viscosity of aquous mixtures containing main components of natural lung surfactant. The control sample is a mixture of DPPC-POPG with a 7:3 ratio. By addition of cholesterol to the lipid mixture the surface viscosity did not change compared to the control. However, by addition of SP-B to the lipid mixture the surface viscosity increased, especially at 0.05mg/ml. the DPPC-POPG-cholesterol-SP-B mixture had similar surface viscosity as the control.
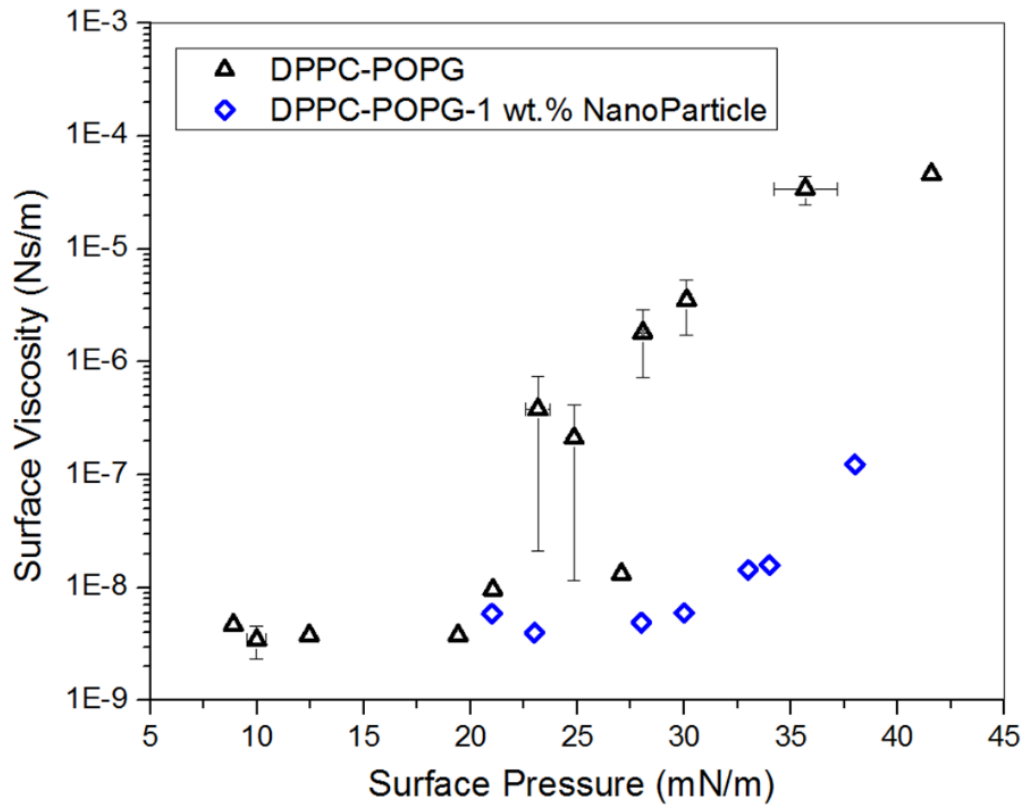
Figure2. Addition of negatively charged nanoparticles to the DPPC-POPG mixture reduced the surface viscosity of the mixture up to 1000-fold. The reduced viscosity could be due to repulsion between negative charges of nanoparticle and the PG headgroup.
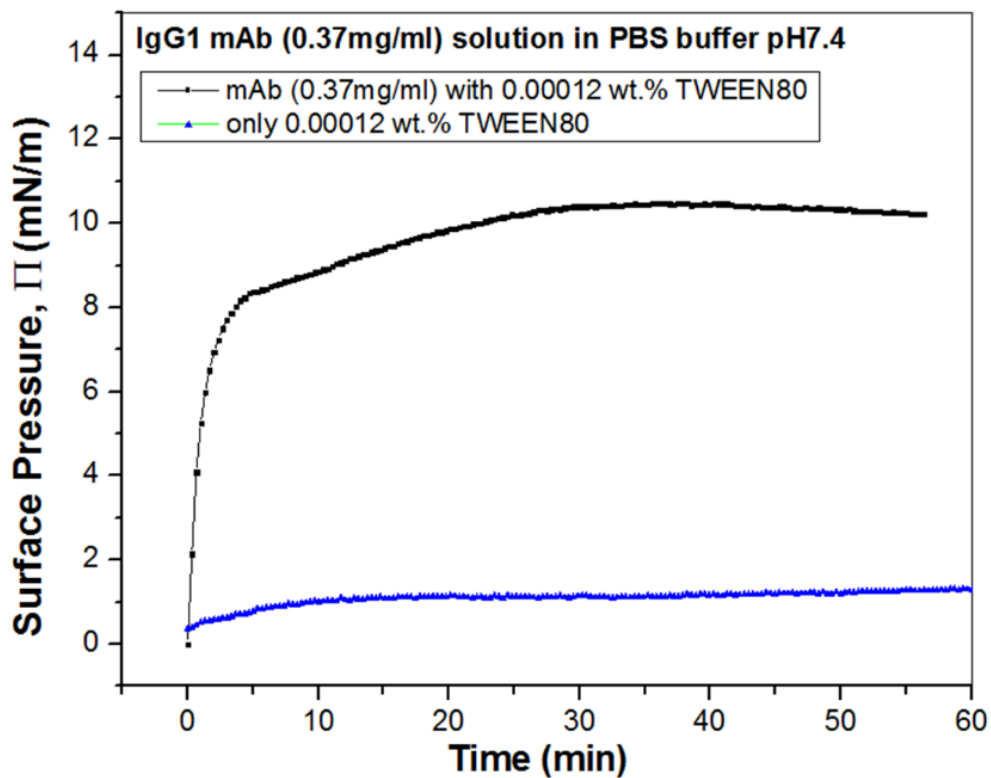
Figure 3. The adsorption of a model IgG1 mAb to the air-water interface at concentration of 0.37mg/ml is compared with the same formulation without the protein. The rate and the saturation surface pressure are dependent to the mAb type and concentration.
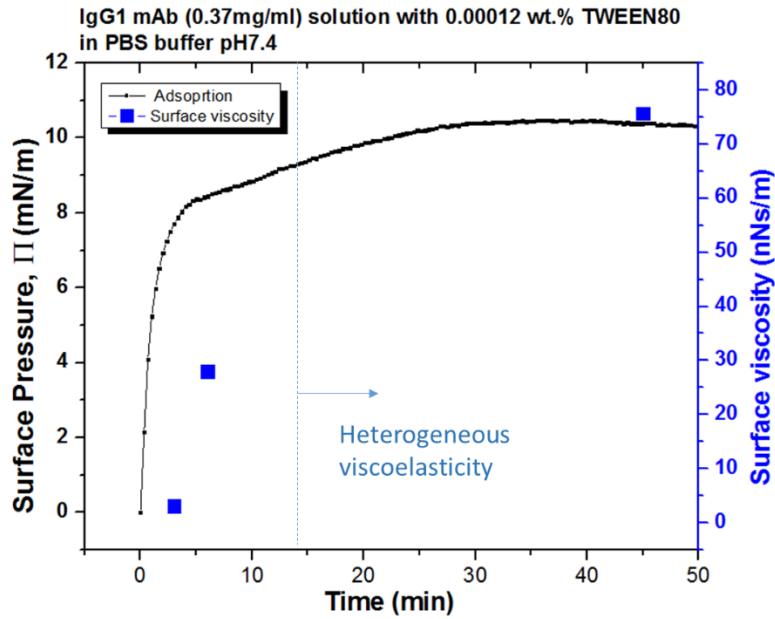
Figure 4. Preliminary date on surface viscosity of a model IgG1 mAb at the air-water interface. The data indicates by increase of adsorption of the protein to the interface, the viscosity increases.

6.4.   References

1.   Notter, R.H., *Lung surfactants: basic science and clinical applications*. 2000: CRC Press.
2.   Simons, K. and D. Toomre, *Lipid rafts and signal transduction.* Nature reviews Molecular cell biology, 2000. **1**(1): p. 31-39.
3.   Edidin, M., *Lipids on the frontier: a century of cell-membrane bilayers.* Nature Reviews Molecular Cell Biology, 2003. **4**(5): p. 414-418.
4.   Edidin, M., *The state of lipid rafts: from model membranes to cells.* Annual review of biophysics and biomolecular structure, 2003. **32**(1): p. 257-283.
5.   Fuller, G.G. and J. Vermant, *Complex fluid-fluid interfaces: rheology and structure.* Annual review of chemical and biomolecular engineering, 2012. **3**: p. 519-543.
6.   Brenner, H., *Interfacial transport processes and rheology*. 2013: Elsevier.
7.   Mendoza, A.J., et al., *Particle laden fluid interfaces: dynamics and interfacial rheology.* Advances in colloid and interface science, 2014. **206**: p. 303-319.
8.   Samaniuk, J.R. and J. Vermant, *Micro and macrorheology at fluid–fluid interfaces.* Soft matter, 2014. **10**(36): p. 7023-7033.
9.   Sachan, A., et al., *Interfacial rheology of coexisting solid and fluid monolayers.* Soft Matter, 2017. **13**(7): p. 1481-1492.
10.   Engel, M.F., et al., *Membrane damage by human islet amyloid polypeptide through fibril growth at the membrane.* Proceedings of the National Academy of Sciences, 2008. **105**(16): p. 6033-6038.
11.   Ditaranto, K., T.L. Tekirian, and A.J. Yang, *Lysosomal membrane damage in soluble Aβ-mediated cell death in Alzheimer's disease.* Neurobiology of disease, 2001. **8**(1): p. 19-31.
12.   Als-Nielsen, J., et al., *Principles and applications of grazing incidence x-ray and neutron scattering from ordered molecular monolayers at the air-water interface.* Physics Reports, 1994. **246**(5): p. 251-313.
13.   Helm, C., et al., *Phases of phosphatidyl ethanolamine monolayers studied by synchrotron x-ray scattering.* Biophysical journal, 1991. **60**(6): p. 1457.
14.   Alonso, C., et al., *More than a monolayer: relating lung surfactant structure and mechanics to composition.* Biophysical Journal, 2004. **87**(6): p. 4188-4202.
15.   Alonso, C., A. Waring, and J.A. Zasadzinski, *Keeping lung surfactant where it belongs: protein regulation of two-dimensional viscosity.* Biophysical journal, 2005. **89**(1): p. 266-273.
16.   Lee, K.Y.C., *Collapse mechanisms of Langmuir monolayers.* Annu. Rev. Phys. Chem., 2008. **59**: p. 771-791.
17.   Kim, K., et al., *Effect of cholesterol nanodomains on monolayer morphology and dynamics.* Proceedings of the National Academy of Sciences, 2013. **110**(33): p. E3054-E3060.
18.   Dawson, K.A., A. Salvati, and I. Lynch, *Nanotoxicology: nanoparticles reconstruct lipids.* Nature nanotechnology, 2009. **4**(2): p. 84-85.
19.   Love, S.A., et al., *Assessing nanoparticle toxicity.* Annual review of analytical chemistry, 2012. **5**: p. 181-205.
20.   Guhaniyogi, J., et al., *Crystal structure and autoactivation pathway of the precursor form of human tripeptidyl-peptidase 1, the enzyme deficient in late infantile ceroid lipofuscinosis.* Journal of Biological Chemistry, 2009. **284**(6): p. 3985-3997.
21.   Shieh, I.C. and A.R. Patel, *Predicting the agitation-induced aggregation of monoclonal antibodies using surface tensiometry.* Molecular pharmaceutics, 2015. **12**(9): p. 3184-3193.
22.   Lee, M.H., et al., *Combined Passive and Active Microrheology Study of Protein-Layer Formation at an Air− Water Interface.* Langmuir, 2009. **26**(4): p. 2650-2658.
23.   Mehta, S.B., et al., *Gelation of a monoclonal antibody at the silicone oil–water interface and subsequent rupture of the interfacial gel results in aggregation and particle formation.* Journal of pharmaceutical sciences, 2015. **104**(4): p. 1282-1290.